The Dissertation Committee for James Courtney Knight Certifies that this is the approved version of the following dissertation:

Electrochemical Properties and Ion-extraction Mechanisms of Li-rich Layered Oxides and Spinel Oxides

Committee:

Arumugam Manthiram, Supervisor

Charles Buddie Mullins

Paulo J. Ferreira

Guihua Yu

Gyeong S. Hwang

Electrochemical Properties and Ion-extraction Mechanisms of Li-rich Layered Oxides and Spinel Oxides

by

James Courtney Knight, B.S.C.E.

Dissertation

Presented to the Faculty of the Graduate School of

The University of Texas at Austin

in Partial Fulfillment

of the Requirements

for the Degree of

Doctor of Philosophy

The University of Texas at Austin

August 2015

Acknowledgements

I would like to thank my advisor, Dr. Arumugam Manthiram, for his help and guidance throughout my graduate studies. I certainly learned a lot and grew as a researcher under his supervision. I would also like to thank my committee members, Professors Buddie Mullins, Paulo Ferreira, Guihua Yu, and Gyeong Hwang, for their time and effort in helping me improve my dissertation. I would not have been able to complete this process without the help of numerous past and present colleagues in Dr. Manthiram's research group, including Dr. Eun Sung Lee, Dr. Seung-Min Oh, Dr. Chih-Chieh Wang, Dr. Xingde Xiang, Dr. Wang Hay Kan, Dr. Il Tae Kim, Dr. Junqing Pan, Dr. Katharine Harrison, Matt Beaudry, Justin Hrbacek, Dr. Veronica Augustyn, Dr. Jianming Zheng, Dr. Yongzhu Fu, Dr. Anmin Cao, Dr. Eungje Lee, Aaron Dangerfield, Dr. Matt West, Tchaa Taro, Dr. Zach Moorhead-Rosenberg, Dr. Katharine Chemelewski, Dr. Arturo Gutierrez, Lauren Murrah, and, particularly, two community college professors, Dr. Soosairaj Therese and Dr. Pat Nandakumar, who helped me perform part of my experimental work. I also thank NASA, SACHEM, the DOE, and the NSF Materials Interdisciplinary Research Team for funding. Finally, I would like to thank my family and friends for their help and support.

Electrochemical Properties and Ion-extraction Mechanisms of Li-rich Layered Oxides and Spinel Oxides

James Courtney Knight, Ph.D.

The University of Texas at Austin, 2015

Supervisor: Arumugam Manthiram

Li-ion batteries are widely used in electronics and automotives. Despite their success, improvements in cost, safety, cycle life, and energy density are necessary. One way to enhance the energy density is to find advanced cathodes such as Li-rich layered oxides, which are similar to the commonly layered oxide cathodes (*e.g.,* $LiCoO_2$), except there are additional Li ions in the transition-metal layer, due to their higher charge-storage capacity. Another way of advancing is to design new battery chemistries, such as those involving multivalent-ion systems (*e.g.,* Mg^{2+} and Zn^{2+}) as they could offer higher charge-storage capacities and/or cost advantages.

Li-rich layered oxides have a complex first charge-discharge cycle, which affects their other electrochemical properties. Ru doping was expected to improve the performance of Li-rich layered oxides due to its electroactivity and overlap of the $Ru^{4+/5+}$:4d band with the O^{2-}:2p band, but it unexpectedly decreased the capacity due to the reduction in oxygen loss behavior. Preliminary evidence points to the formation of Ru-Ru dimers, which raises the $Ru^{4+/5+}$:4d band, as the cause of this behavior.

Li-rich layered oxides suffer from declining operating voltage during cycling, and it is a huge challenge to employ them in practical cells. Raising the Ni oxidation state was found to reduce the voltage decay and improve the cyclability; however, it also

decreased the discharge capacity. Increasing the Ni oxidation state minimized the formation of Mn^{3+} ions during discharge and Mn dissolution, which led to the improvements in voltage decay and cyclability.

Extraction of lithium from spinel oxides such as $LiMn_2O_4$ with acid was found to follow a Mn^{3+} disproportionation mechanism and depend on the Mn^{3+} content. Other common dopants like Cr^{3+}, Fe^{3+}, Co^{3+}, or $Ni^{2+/3+}$ did not disproportionate, and no ion-exchange of Li^+ with H^+ occurred in the tetrahedral sites of the spinel oxides.

Extraction with acid of Mg and Zn from spinel oxides, such as $MgMn_2O_4$ and $ZnMn_2O_4$, were also found to follow the same mechanism as Li-spinels. The Mg-spinels, however, do experience ion exchange when Mg ions are in the octahedral sites. Chemical extraction of Mg or Zn with an oxidizing agent NO_2BF_4 in acetonitrile medium, however, failed due to the electrostatic repulsion felt by the migrating divalent ions. In contrast, extraction with acid was successful as Mn dissolution from the lattice opened up favorable pathways for extraction.

Table of Contents

List of Tables

List of Figures

Chapter 1: Introduction*

1.1. Introduction to Li-rich layered oxides

Li-ion batteries (LIBs) have become prevalent in modern day society, as they power cell phones, laptops, and electric vehicles (EV), amongst many other items. Significant research attention is being paid to them in order to expand their use in the EV market and for possible deployment in grid storage applications for renewable power sources, such as wind, solar, and geothermal. One of the most explored areas of research in LIBs is designing cathode materials that have improved capacity, stability, rate capability, cycle life, and safety, while keeping the cost low. Li-rich layered oxides (LLOs) are a family of cathodes that has received lots of attention as a potential next-generation cathode for LIBs. The prime advantage of these materials is their high discharge capacities (250 – 300 mAh g^{-1}) and energy densities, as they represent a significant improvement over the most common commercial LIB cathodes: $LiCoO_2$ (140 mAh g^{-1}), $LiMn_{1/3}Ni_{1/3}Co_{1/3}O_2$ (180 mAh g^{-1}), and $LiMn_2O_4$ (120 mAh g^{-1}). The other beneficial trait of LLOs is their lower cost due to a reduction in Co content. The structure of LLOs is described by researchers as either a solid solution or a nanocomposite of Li_2MnO_3 and $LiMO_2$, where M is a collection of metals, most often Mn, Ni, and Co. The high discharge capacity of LLOs is derived from its unique first charge-discharge cycle

* Portions of this chapter have previously been published as A. Manthiram, J. C. Knight, S.-T. Myung, S.-M. Oh, and Y.-K. Sun, "Nickel-rich and Lithium-rich Layered Oxide Cathodes: Progress and Perspectives", *Advanced Energy Materials*, accepted 2015.
J. C. Knight and A. Manthiram prepared the portion of the manuscript on Li-rich layered oxides and assembled the final document. S.-T. Myung, S.-M. Oh, and Y.-K. Sun prepared the portion of the manuscript on Ni-rich layered oxides.

that consists of transition-metal (TM) oxidation followed by the oxidation and loss of oxide ions from the lattice during charge, which leads to a compensatory Mn reduction during discharge. Unfortunately, a myriad of challenges are also associated with LLOs. The LLOs suffer from oxygen loss from the lattice during first charge, high first cycle irreversible capacity loss (IRC), poor rate capability, low volumetric energy density due to a low tap density, and a substantial voltage decay over extended cycling due to a transformation to a spinel-like phase. These issues will be discussed in further detail later in this chapter.

The roots of LLO research go back to 1991, when Thackeray *et al.*, inspired by Hunter's work, produced $Li_{1.09}Mn_{0.91}O_2$ by acid treatment followed by relithiation of Li_2MnO_3, and introduced the idea of $xLi_2MnO_3 \cdot (1-x)LiMnO_2$.[1, 2] Years later, Kalyani *et al.* discovered that Li_2MnO_3 could be electrochemically cycled.[3] Lu *et al.* put these ideas together and studied the $Li[Li_{(1/3-2x/3)}Mn_{(2/3-x/3)}Ni_x]O_2$ series in detail.[4-6] Research interest in this topic expanded in the following years, with a lot of the initial work focusing on improving the electrochemical behavior by incorporating other metal ions into the structure or by surface coating, understanding the unique mechanism of the first charge-discharge reaction, and clarifying the structure of the materials. The compositions of LLOs are often written in one of the three different notations. The first two notations are $xLi[Li_{1/3}Mn_{2/3}]O_2 \cdot (1-x)LiMO_2$ and $xLi_2MnO_3 \cdot (1-x)LiMO_2$, while the third notation is $Li_{1+x}M_{1-x}O_2$, where M = Mn, Co, Ni, *etc*. One can easily convert among the three notations. For example, $0.6Li[Li_{1/3}Mn_{2/3}]O_2 \cdot 0.4LiMO_2$ is the same as

$0.5Li_2MnO_3 \cdot 0.5LiMO_2$, which is equivalent to $Li_{1.2}Mn_{0.6}Ni_{0.2}O_2$ if M = $[Mn_{1/2}Ni_{1/2}]$. This is a common, often investigated, LLO composition.

1.2. STRUCTURE

As with all LIB cathode materials, the structure of LLOs can dramatically affect the electrochemical performance, so it is essential that the structure of LLO be clarified. LLOs can be thought of as a combination of $LiMO_2$ and Li_2MnO_3. $LiMO_2$ possesses a rhombohedral $R\bar{3}m$ structure, while Li_2MnO_3 adopts a $C2/m$ monoclinic structure. The two structures, which can be seen in Figure 1.1a, are very similar, as Li_2MnO_3 can be written in the normal layered stoichiometry as $Li[Li_{1/3}Mn_{2/3}]O_2$. The different space group of Li_2MnO_3 arises from the ordering between the Li^+ and Mn^{4+} ions in the TM layer of the structure. Both $LiMO_2$ and Li_2MnO_3 have a cubic close packed oxygen array in which all the resulting octahedral sites are filled by alternating layers of Li and TM or Li/TM. The peaks in a typical LLO X-ray diffraction (XRD) pattern can be indexed to the $R\bar{3}m$ space group, with the exception of some weak reflections in the 20° - 25° range, as shown in Figure 1.1c. These superstructure reflections are due to Li^+/Mn^{4+} ordering in the TM layer, and they, along with the major peaks, can be indexed to the $C2/m$ space group. Reitveld refinement of powder and synchrotron XRD data provide excellent fits when using both space groups in their models, but XRD data can only reveal the average crystal structure.[7, 8] More advanced characterization techniques must be applied in order to study the local structure of LLO.

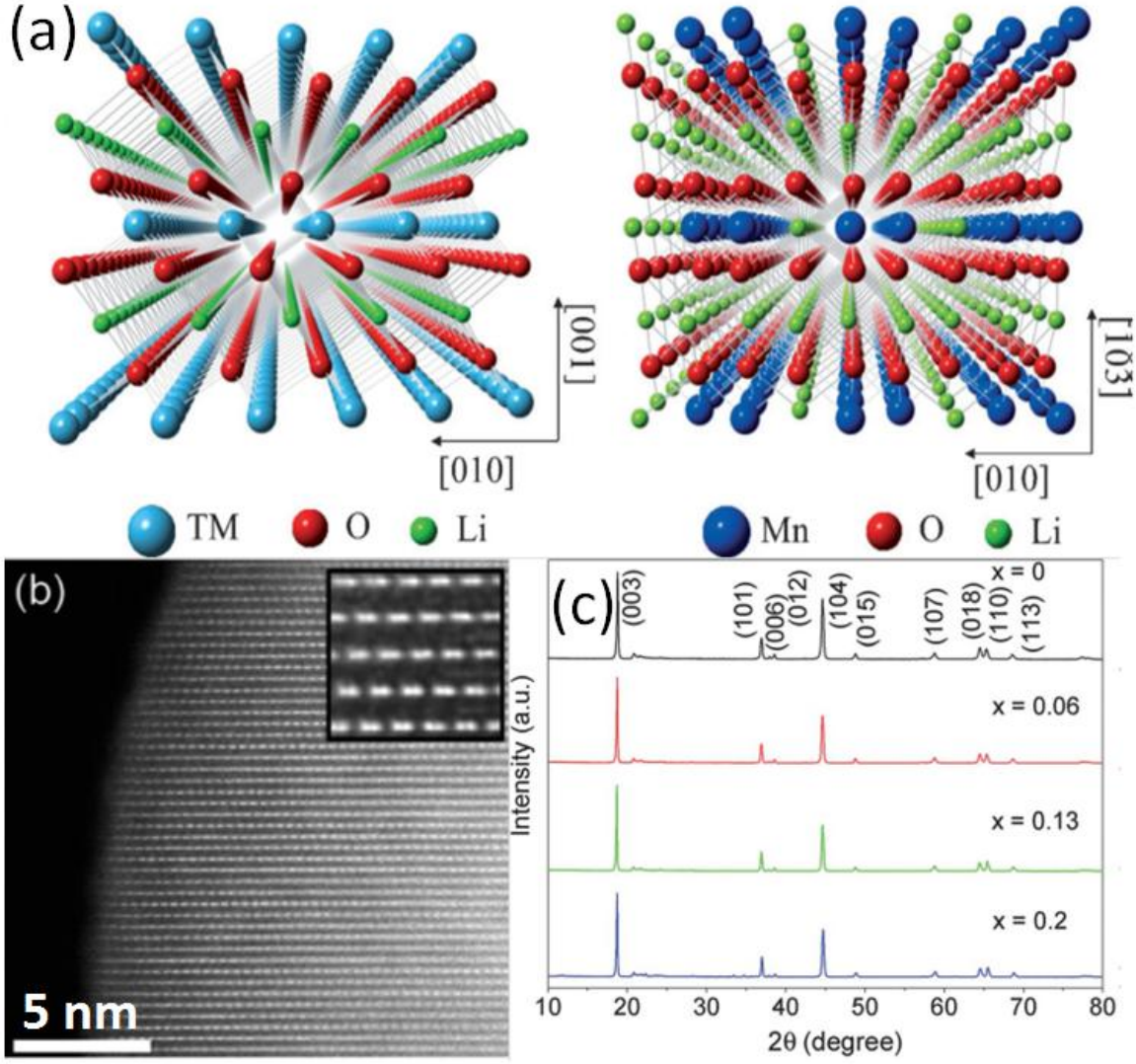

Figure 1.1. (a) Crystallographic models of the $LiTMO_2$ structure (left) with $R\bar{3}m$ symmetry and the Li_2MnO_3 structure (right) with $C2/m$ symmetry. Reproduced with permission.[9] Copyright 2013 Wiley-VCH Verlag GmbH & Co. KGaA, Weinheim. (b) Aberration-corrected HAADF-STEM image of $Li_{1.2}Mn_{0.6}Ni_{0.2}O_2$ viewed down the $[\bar{1}21]_{NaCl}$ zone axis showing a $C2/m$ -like arrangement. Reproduced with permission.[10] Copyright 2014 The Royal Society of Chemistry. (c) XRD patterns of $Li_{1.2}Mn_{0.6-0.5x}Ni_{0.2-0.5x}Co_xO_2$ ($0 < x < 0.2$) series showing typical LLO pattern. Reproduced with permission.[11] Copyright 2013 The Royal Society of Chemistry.

Due to the similarity of the $LiMO_2$ and Li_2MnO_3 phases, the local structure of LLOs is very complex, difficult to elucidate, and essential to understanding these materials and their performance. In order to study the local structure, high-resolution transmission electron micrscoscopy (HRTEM), high-angle annular dark field scanning transmission electron microscopy (HAADF-STEM), and electron energy-loss spectroscopy (EELS) analysis are required. Significant research efforts have been made to discern the local LLO structure, but there is still no clear consensus amongst researchers. Several researchers have found evidence of solid solution behavior. For instance, numerous studies have found that LLOs obey Vegard's law in that their structural parameters vary linearly with composition.[12-14] Also, researchers have used advanced TEM analysis to directly show the formation of a single structure at the atomic level, although some studies have found $R\bar{3}m$ symmetry, while others have found $C2/m$ symmetry.[13-16] An HAADF-STEM image of a particle exhibiting $C2/m$ symmetry can be seen in Figure 1.1b. Other studies discovered two-phase behavior by showing distinct regions of monoclinic and rhombohedral symmetry within the same particle or Mn-rich domains.[9, 17-22] Perhaps the most widely accepted model is the nanocomposite model put forth by Thackeray *et al.*[23] They posit that because there are not enough Li ions in the TM layer in most LLO compositions to maintain the 1 Li to 2 TM ratio found in Li_2MnO_3, there are Li_2MnO_3-like and $LiMO_2$-like nanodomains that result in short-range order but not a full solid solution, which has been supported by several studies.[19, 24, 25] Consensus on the local structure of LLO will most likely continue to be elusive because

the structure has been found to be sensitive to multiple factors, including Li content, cooling rate, composition, and synthesis temperature, among others.[10, 26-30]

1.3. First Charge-discharge Cycle Mechanism

One of the defining features of LLOs is their unique first charge-discharge cycle mechanism, which is still not fully understood. The initial charge cycle consists of two regions. During the first part, Li is extracted due to the oxidation of the TM ions to the 4+ oxidation state. This process occurs up to ~ 4.4 V and the capacity from this region varies based on the composition of the material and the charge current. The second phase is a long plateau that occurs above 4.4 V and consists of Li being removed concomitantly with oxygen; oxide ions are oxidized and lost as O_2 gas, but LLOs can be thought of as losing Li_2O. In this article, these regions will be referred to as the "sloping region" and the "oxygen-loss plateau". The initial discharge cycle is also complex due to the complicated nature of the first charge cycle. During the first discharge, the TM ions that were oxidized during the sloping region are reduced back to their initial states. Then, because of the lost oxygen ions during charge, another ion must be reduced, so some Mn^{4+} ions are reduced to Mn^{3+}. While this mechanism can explain the high capacities seen with LLOs (up to 300 mAh g^{-1}), it would require almost every Mn^{4+} ion to be reduced to Mn^{3+}. Other mechanisms, such as reversible oxygen reduction, side reactions with the electrolyte, and/or proton exchange, are also believed to provide additional capacity.[31-36] These mechanisms will be further discussed later.

Numerous studies have focused on the substitution of different metal ions into a base LLO composition, often $Li_{1.2}Mn_{0.6}Ni_{0.2}O_2$, in order to alter the length of the sloping region and oxygen-loss plateau. When substituting an additional metal ion into the composition, Ni and Mn should be kept in their 2+ and 4+ oxidation states, respectively, so the new compositions must be chosen carefully. This means that a 2+ ion, such as Mg^{2+}, should replace Ni^{2+}, while a 4+ ion, such as Ti^{4+}, should replace Mn^{4+}. A 3+ ion, such as Al^{3+}, should replace Mn^{4+} and Ni^{2+} equally. Any dopant ion that can be oxidized above 4+ will significantly increase the length of the sloping region. Examples of this include Ru and Cr, as they can be oxidized to 5+ and 6+, respectively.[11, 37] Conversely, substitution of electroinactive ions, such as Mg^{2+}, Al^{3+}, and Ga^{3+}, markedly decrease the length of the sloping region.[11] Ions that maintain the same level of electroactivity, such as Co^{3+} and Fe^{3+}, cause slight changes in the length of the sloping region due to changes in conductivity and whether or not they can be fully oxidized to the 4+ state.[11, 38] The effect of substituted ions on the length of the plateau region is not as straightforward, however, as it varies with the covalency of the metal-oxygen bond. The covalence of this bond is determined by the position of the metal 3d band relative to the top of the O^{2-}:2p band.[11] The overlap of the $Co^{3+/4+}$:t_{2g} band with the top of the O^{2-}:2p band leads to Co as the only dopant found to significantly increase the oxygen-loss plateau length.[38] Other metal ions, such as Ti^{4+}, reduce the length of the oxygen-loss plateau upon substitution due to their less covalent metal-oxygen bonds.[39] This is usually an intrinsic property of the ion, but sometimes can be caused by other factors, such as the formation of Ru-Ru dimers.[37] Figure 1.2a illustrates the effect of Co^{3+} and Ti^{4+} doping on the sloping region

and the oxygen-loss plateau, while Figure 1.2b depicts a qualitative energy band diagram of those materials.

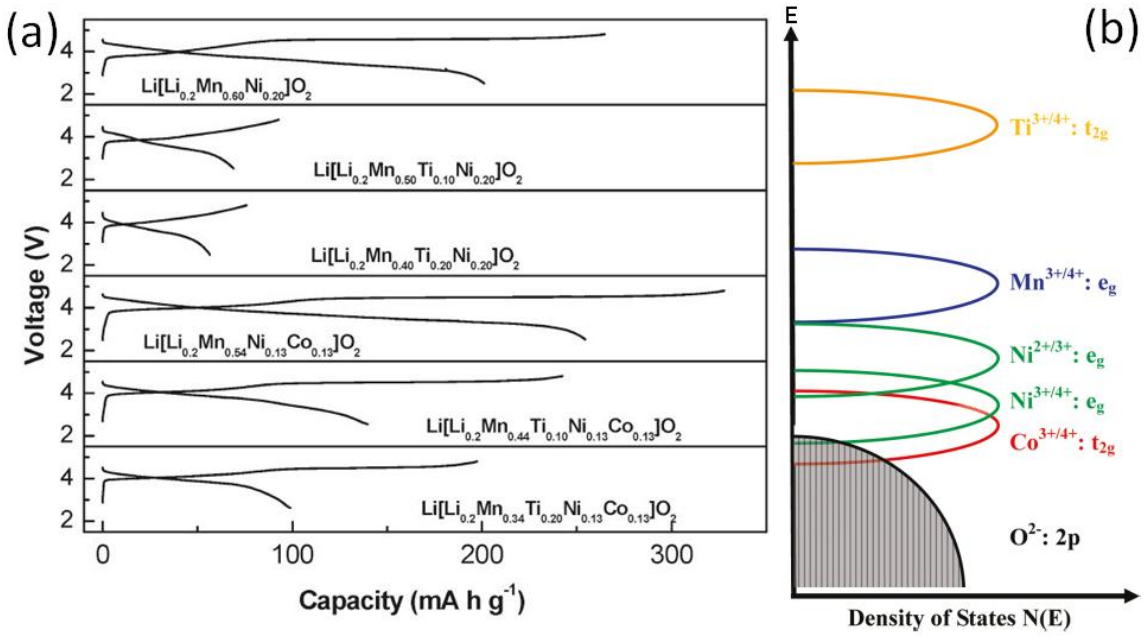

Figure 1.2. (a) The first cycle charge-discharge curves of $Li_{1.2}Mn_{0.54-x}Ti_xNi_{0.13}Co_{0.13}O_2$ and $Li_{1.2}Mn_{0.6-x}Ti_xNi_{0.2}O_2$ (x = 0, 0.1, and 0.2) are compared. (b) A qualitative diagram illustrating the relative positions of various energy bands common to LLOs. Reproduced with permission.[39] Copyright 2011 American Chemical Society.

A lot of recent work in this area has focused on better elucidating the oxygen-loss plateau mechanism. Because the oxygen-loss behavior is derived from the Li_2MnO_3 character of the LLO system, one might think that studying the cycling mechanism of Li_2MnO_3 would provide insight into the mechanism of LLO. To that end, Li_2MnO_3 has also been investigated extensively, where it was found that H^+/Li^+ ion exchange accounts for some of the electrochemical activity in the plateau region.[36] However, Dogan *et al.* and Croy *et al.* used nuclear magnetic resonance (NMR) and X-ray absorption

spectroscopy (XAS) measurements to show that not only ion exchange does not occur in LLO during the oxygen-loss plateau, but also the Li_2MnO_3 component of LLO does not behave structurally or electrochemically like pure Li_2MnO_3.[40, 41] They did, however, find the progressive build-up of proton-containing species presumably on the cathode surface during extended cycling. This leaves oxide ion oxidation and subsequent loss of Li_2O as the accepted cause of the oxygen-loss plateau. It has been confirmed by differential electrochemical mass spectrometry (DEMS), synchrotron XRD, EELS, and Rietveld refinement that oxide ions are oxidized and oxygen gas is evolved during the oxygen-loss plateau.[6, 25, 42, 43] Recently, however, Delmas *et al.* have proposed a more complicated mechanism of irreversible oxide-ion oxidation and subsequent oxygen loss at the surface of the particles coupled with reversible oxide-ion oxidation in the bulk.[15, 31, 32, 44] They used electrochemical measurements, neutron diffraction, chemical analysis, Raman spectroscopy, and HAADF-STEM to reach this conclusion by showing that oxygen gas is evolved at the surface, TM ions migrate from the surface to the bulk in a densification process, but that the bulk structure does not undergo any significant structural change.

Several studies by Tarascon *et al.* have focused on Li_2RuO_3-based materials that are similar in structure to Li_2MnO_3 in order to study the electrochemical mechanism of LLO.[33, 34, 45, 46] They were able to demonstrate that oxide ions can be reversibly oxidized to peroxide/superoxide-like species and that the propensity to do so, as opposed to being irreversibly lost as oxygen gas, can be altered by cation substitution, such as Sn, which affects the *d-sp* hybridization of the metal-oxygen bond. Other work has been done on first cycle mechanism, but it will be discussed in the sections on IRC and voltage decay.

1.4. OBSTACLES TO COMMERCIALIZATION

While researchers have made great strides in understanding the structure and properties of LLOs, as well as improving their performance and mitigating some of their deficiencies, significant progress is still required in order for LLOs to become commercially viable. The major challenges associated with LLOs include voltage decay during cycling, large 1st cycle IRC, poor rate capability, and low volumetric energy density. A brief overview of these issues and some recent progress in overcoming these challenges is presented below.

1.4.1. Voltage Decay

Voltage decay, which may also be denoted as voltage fade, is perhaps the greatest obstacle to LLO commercialization, and it refers to the fact that during extended cycling, LLOs suffer from a significant decrease in operating voltage. This in turn causes a reduced energy density and difficulty in determining the state of charge of battery cells. It is understood that there is a gradual structural change to a new phase during extended cycling, that TM ions migrate into Li sites in both the TM and Li layers, and a TM-rich and Li-poor surface phase is formed, where TM ions are reduced and react with the electrolyte.[47-51] Though the exact structure of the defect phase is not fully understood, it is commonly referred to as a spinel-type phase, which is the term used in this progress report. Numerous published reports have shown evidence of the increasing spinel-like phase growth during extended cycling through dQ/dV analysis, XAS, and HRTEM, some of which are shown in Figure 1.3a.[52-55] Because of these observations and others, some

studies conclude that the structural change begins at the surface and grows during cycling.[47, 48] On the other hand, other studies have found voltage decay to be derived from the bulk and that surface effects are not a huge factor.[41, 56] Density functional theory (DFT) calculations and neutron diffraction have shown that voltage decay is promoted primarily by two mechanisms: the migration of TM ions from the octahedral sites of the metal layer through tetrahedral sites to empty octahedral sites in the Li layer and the formation of Li dumbbell structures, which are two Li ions trapped in tetrahedral sites above and below a Li site vacancy in the metal layer.[57, 58] Sathiya *et al.*, however, found that TM ions migrating to the Li layer was not a major cause of concern, but instead problems arise when TM ions are trapped in tetrahedral sites, which can be reduced by using larger TM ions.[46]

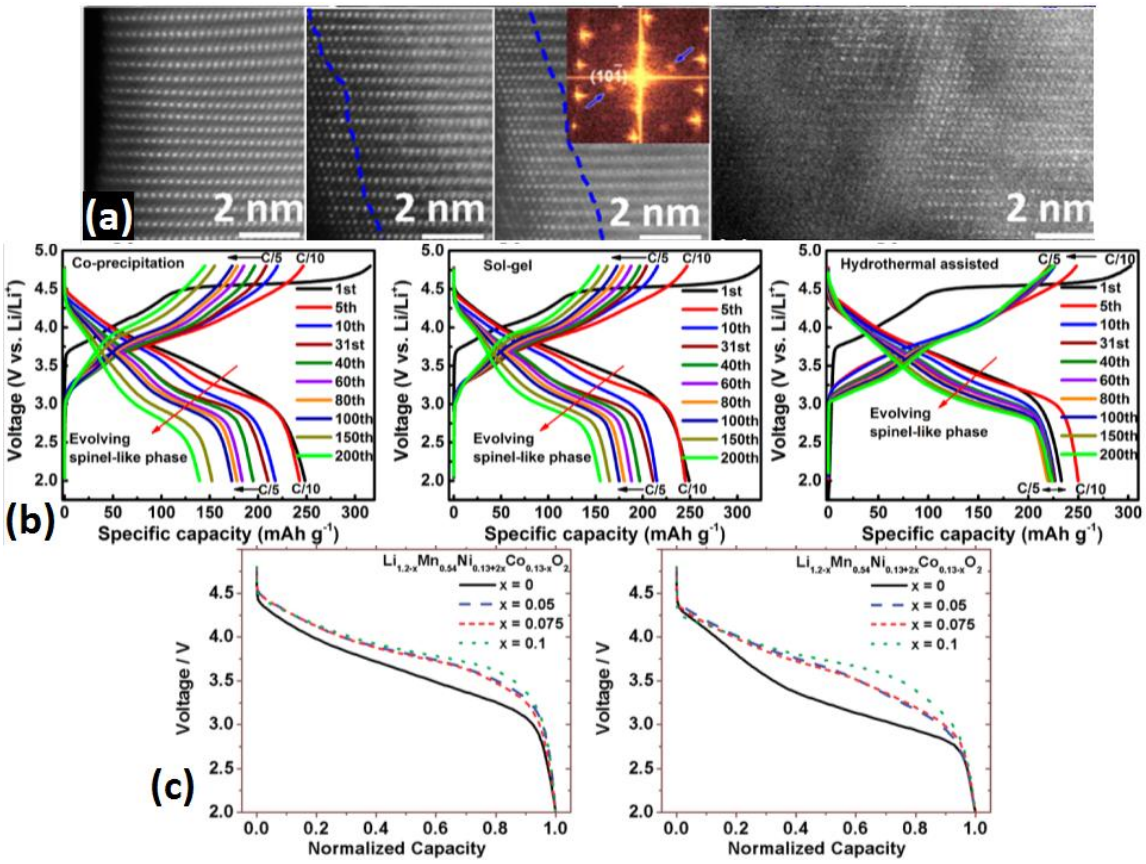

Figure 1.3. (a) High resolution HAADF-STEM images of $Li_{1.2}Mn_{0.6}Ni_{0.2}O_2$ after (from left to right) 0, 5, 45, and 100 cycles showing the gradual growth of the spinel-like surface layer. Reproduced with permission.[47] Copyright 2014 American Chemical Society. (b) Voltage profiles of $Li_{1.2}Mn_{0.6}Ni_{0.2}O_2$ synthesized using a (from left to right) co-precipitation, sol-gel, and hydrothermal assisted method showing voltage decay during extended cycling. Reproduced with permission.[59] Copyright 2014 American Chemical Society. (c) The 1st (left) and 50th (right) cycle normalized discharge profiles of $Li_{1.2-x}Mn_{0.54}Ni_{0.13+x}Co_{0.13-x}O_2$ (x = 0, 0.05, 0.075, and 0.1) showing the reduced voltage decay at higher x values. Reproduced with permission.[60] Copyright 2014 The Royal Society of Chemistry.

Extensive work has recently been done at Argonne National Laboratory to elucidate the voltage decay mechanism.[41, 56, 61-63] Among many other findings, they propose a mechanism that leads to voltage decay.[62] Upon charging, some TM ions

migrate to tetrahedral sites, and then once discharged to ~ 3.3 V, they may follow one of three paths. They may migrate back to octahedral sites in the TM layer, which leads to an energy difference that manifests as hysteresis during cycling. They may become trapped in the tetrahedral sites, which leads to decreased Li diffusion, increased impedance, and reduced capacity, or they may migrate to octahedral sites in the Li layer, which alters the local structure to one with a lower operating voltage, causing voltage decay. Synthesis technique and conditions can also affect voltage decay, as researchers have reduced voltage decay by utilizing a hydrothermal assisted synthesis method instead of the standard co-precipitation and sol-gel methods to produce greater Ni-homogeneity throughout the particles.[59] This led to a uniform $C2/m$ phase particle as opposed to a mixture of $R\bar{3}m$ and $C2/m$ phases, minimized the amount of Ni^{4+} ions at the particle surface, which are highly reactive with the electrolyte, and enhanced the Ni-Mn interactions that have been shown to stabilize the LLO structure.[47, 64, 65]

Figure 1.3b shows the vast differences in voltage decay produced by various synthesis techniques. Specific surface facets can greatly affect the mechanism, as Yan *et al.* concluded that surfaces terminating in purely cations or purely anions were resistant to structural changes, whereas surfaces terminating in a mix of cations and anions produced a surface layer that was Mn-rich on the outside but Ni-rich on the inside.[47] They proposed that Ni migrated from the bulk to the surface, where it reacted with the electrolyte at a faster rate than Mn, which led to voltage decay due to decreased redox capability and a reduction in stabilizing Mn-Ni interactions.

Other mechanistic studies have found that two competing rate laws determine the kinetics of voltage decay and that proton insertion does not play a role in the process.[41, 66] While it was originally thought that voltage decay arose due to the high voltage required to active the Li_2MnO_3 component of LLO, Li *et al.* has shown that the process occurs even when LLOs are cycled well below this activation threshold.[67] A simple analysis to visualize the voltage decay is to just compare the shapes of voltage profiles of an early cycle to one after extended cycling; however this method is not always accurate due to differences in specific capacities and the fact that electrode impedance also affects voltage decay. Normalizing voltage profiles eliminates the first issue, while Bettge *et al.* suggests a testing protocol focused on the iR-corrected average voltage of materials to overcome the second.[60, 68]

Researchers are attacking this problem from several different directions. One of which is intelligently altering the composition of LLOs through doping. Lee and Manthiram showed that while the octahedral site stabilization energy (OSSE) of the TM ions is a significant factor in the phase transformation of layered oxides, it does not play as large a role in LLO due to the differences in their dumbbell formations.[60] On the other hand, they found that decreasing the length of the oxygen-loss plateau by increasing the Ni content at the expense of the Li and Co content is an effective means of reducing voltage decay, which agrees with another study that shows increasing Li_2MnO_3 content increases voltage decay.[60, 62] This inhibits voltage decay by reducing the amount of Li ions in the TM layers, so fewer dumbbells are formed and by creating fewer oxygen

vacancies, which in turn hinders TM ion migration. The voltage decay reduction produced by their novel LLO series is depicted in Figure 1.3c.

Song *et al.* extended this idea by increasing the sloping region at the expense of the oxygen-loss plateau even further by doping with Cr and saw reduced voltage decay.[69] Ates *et al.* and Li *et al.* recently used the addition of Na^+ and K^+ ions, respectively, to show that monovalent dopants can provide structural stability to LLO and block the layered-to-spinel transformation.[70, 71] Ates *et al.* published another report that used Ni^{3+} doping to improve voltage decay by decreasing the amount of Mn^{3+} created during the first discharge, which increases the average discharge voltage and inhibits the growth of the spinel-like phase.[72] Zheng *et al.* coated LLO with AlF_3 and found that it reduces voltage decay by providing structural stability and protecting the electrode from side reactions with the electrolyte; however, a previous study did not see any improvement by various other coatings.[73, 74] Recent attempts at forming composite materials by combining LLOs with high-voltage spinel materials have had success, as the spinel additive stabilizes the layered structure and inhibits the additional growth of the spinel-like phase.[64, 75-77] Composites can be created by using less Li than is stoichiometrically required during calcining or by growing a spinel outer layer on LLO seed particles using a modified sol-gel process.

1.4.2. Rate Capability

Another significant issue with LLOs is their low rate capability. This is caused by several factors, including the insulating nature of Mn^{4+} ions in the Li_2MnO_3 component, a

large charge-transfer resistance at the interface between the particle and the electrolyte, a thick SEI layer that forms during cycling, poor delithiation kinetics (particularly in the Li_2MnO_3 component), and the often large particles of LLOs made by researchers.[78, 79]

There are several strategies that researchers have used in order to increase the rate capability of LLOs. The first and most prevalent method to enhance rate capability is through surface modification, which can refer to either coating the particle surface with a compound or treating the surface to enact a structural change. Surface modification increases rate capability by decreasing the charge-transfer resistance, increasing particle conductivity, and/or altering the SEI layer thickness and composition. Electrically conductive coatings, often made of polymers, carbon-based materials, or carbon composites, enhance the rate capability by increasing the conductivity of LLOs. Examples of these coatings include carbon, graphene-like carbon, carbon nanotubes, polyaniline, a polystyrene/polythiophene-based polymer (PEDOT:PSS), an Li_3PO_4/C composite, and reduced graphene oxide (rGO)/$AlPO_4$ composites.[80-87] A TEM image of an rGO/$AlPO_4$ composite coated particle and the rate capability improvement can be seen in Figure 1.4b and Figure 1.4c, respectively. The remaining coatings can be summarized as metal oxides and metal phosphates, and their rate capability improvement is derived from lowering the charge-transfer resistance by creating a different interface with the electrolyte. Therefore, the coatings also change the nature of the SEI layer formation, often resulting in thinner coatings that are less insulating than those on the uncoated materials. CuO, Sm_2O_3/CeO_2, Pr_6O_{11}, V_2O_5, MnO, and Al_2O_3 are examples of successful metal oxide coatings.[88-94] Some examples of metal phosphate coatings include $AlPO_4$,

$CoPO_4$, $CePO_4$, $Li_3V_2(PO_4)_3$, $LiNiPO_4$, and $Co_3(PO_4)_2$.[93, 95-99] One additional coating that has been found to markedly improve rate capability, amongst other electrochemical properties, is AlF_3.[100, 101] There are two challenges when dealing with surface coatings, however. Special care must be taken to ensure that the particles are coated uniformly and that the coating thickness is optimized. With many coatings, there is a thickness "sweet spot", where they are thick enough to impart structural stability but not too thick as to impede electronic and ionic conductivity. Surface treatment is an additional method of improving the rate capability of LLOs, which often consists of exposing the active material to a treatment solution followed by an annealing step. LLOs treated with Super P carbon, NH_4SO_4, and persulfates have been found to increase the rate capability by removing Li^+ ions from the particle surfaces, inducing a structural change to a spinel phase on the surface.[102-105] This improves conductivity and enhances rate capability.

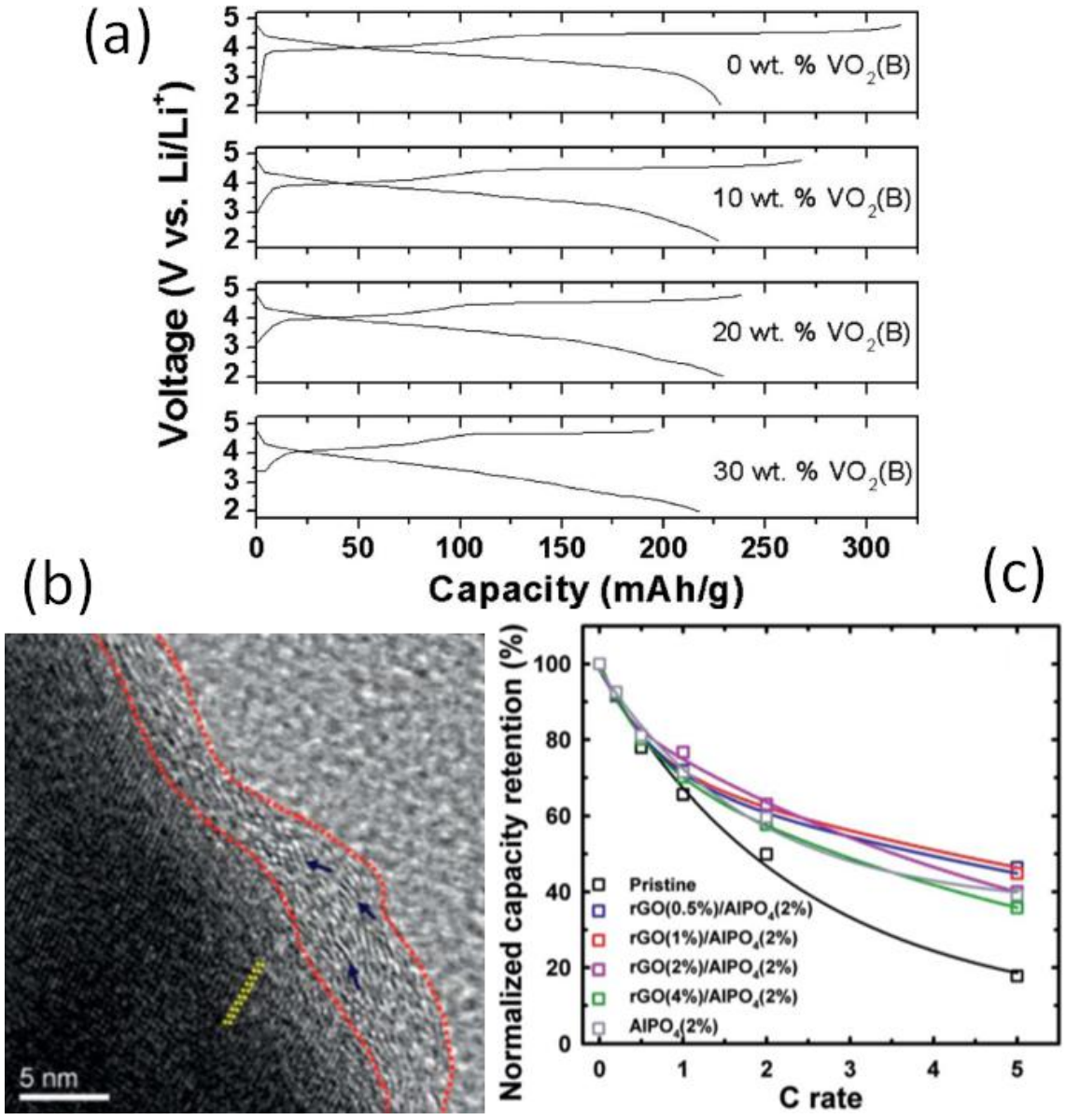

Figure 1.4. (a) First cycle charge-discharge profiles of VO_2(B)- $Li_{1.2}Mn_{0.54}Ni_{0.13}Co_{0.13}O_2$ composites displaying the reduction of IRC. Reproduced with permission.[106] Copyright 2011 The Electrochemical Society. (b) TEM image of LLO sample with rGO (4 wt%)/$AlPO_4$ (2 wt%) composite coating. Reproduced with permission.[86] Copyright 2014 The Royal Society of Chemistry. (c) Plot illustrating the increase in normalized rate capability of LLO coated with rGO/$AlPO_4$ composite coatings.

Furthermore, there are several additional methods utilized to increase the rate capability: altering the synthesis method in order to make particles with shorter Li ion diffusion paths, elemental substitution, and forming composites with other materials. In order to shrink the Li-ion diffusion paths, various nanostructures are employed. For instance, researchers have synthesized micron-sized secondary particles made up of 80 – 200 nm sized primary particles, 30 nm diameter nanowires made by ion exchange that possess a very impressive 5C discharge capacity of 275 mAh g^{-1}, and nanoplates that preferentially expose the (010) surface plane in order to increase Li-ion diffusion.[107-110] The downside to nanoparticles is that they have a drastically increased surface area, which leads to greater SEI layer formation, side reactions with the electrolyte, and safety concerns due to increased oxygen loss.

Elemental substitution is a simple approach to boost rate capability. Certain dopants are able to reduce the impedance of the bulk material and may increase lattice parameters if they have a larger ionic radius, which reduces the energy barrier and promotes Li-ion diffusion. These dopants include Mg, Al, Co, Cr, Fe, Ru, Na, and F, although F doping may actually form an LiF coating instead of going into the lattice.[8, 70, 111-118] A final method to strengthen the rate capability of LLOs is to physically blend it with another material to form a composite. Blending LLOs with high-voltage spinel ($LiMn_{1.5}Ni_{0.5}O_4$) is the most studied composite, as spinels have excellent rate capability due to their 3D Li-ion transport, and they also possess the same cubic close packed oxygen lattice as LLOs.[64, 76] Moreover, Gallagher *et al.* found that mixing LLOs with

$LiFePO_4$ enhanced the rate capabaility and pulse power due to the lower impedance provided by the olivine structure at low states of charge.[119]

1.4.3. First Cycle Irreversible Capacity Loss

A large first cycle IRC, often 60 – 100 mAh g^{-1}, is a third crucial issue for LLOs. In the literature, some researchers instead refer to this issue as a low first cycle Coulombic efficiency, where values are usually less than 80%, but both phrasings refer to the same topic. As with most other electrochemical properties of LLOs, the large IRC is tied to the unique first charge-discharge cycle.[6, 120] During the oxygen-loss plateau, Li_2O is removed from the structure, leaving oxygen vacancies and Li vacancies in both the TM and Li layers behind. At the end of the first charge cycle, some of these vacancies are eliminated through structural densification caused by TM migration.[121] Cations in the TM layer migrate through tetrahedral sites to empty Li sites in the TM layer and in the Li layer, and a corresponding amount of oxygen vacancies are also eliminated. For every oxygen vacancy eliminated, one Li vacancy is also eliminated. Because of this process, not all of the Li ions extracted during the first charge can be inserted back into the structure, causing the high IRC. These excess Li ions are then free to react with product of the electrolyte decomposition to form a thicker SEI layer. Researchers have found that most but not all of the oxygen vacancies are eliminated during the first cycle.[121] The remaining vacancies could be removed during subsequent cycles, which could manifest as fading capacity.

Researchers have used several different solutions to combat the IRC problem. Composite materials can be made by blending LLOs together with a Li-insertion host in order to recapture the Li ions that cannot be reintercalated to the LLO structure. Manthiram's group pioneered this method, initially using V_2O_5, before later investigating LiV_3O_8, $Li_4Mn_5O_{12}$, and VO_2(B).[106, 122, 123] The effect of VO_2(B) addition on the first cycle IRC can be seen in Figure 1.4a. They were able to completely eliminate the first cycle IRC using this method, but the addition of the other hosts decreases the gravimetric capacity. Gallagher *et al.* also reported a decreased IRC when they encorporated $LiFePO_4$ into an LLO composite.[119] The use of Li-insertion hosts only manages the effects of the IRC mechanism, instead of trying to solve the underlying causes of oxygen loss and TM migration. Various methods have been employed to attack the root causes of the large IRC. Surface treatment is again a prevalent and successful method for reducing the IRC. As mentioned in the rate capability section, coatings provide structural stability to LLO,[121] which also helps maintain more of the vacancies that are formed, so they reduce IRC by two different processes.[121] Almost all of the coatings mentioned in the rate capability section reduce the IRC, so they will not be listed in detail here again.[80, 86, 89, 90, 93, 94, 96, 124] One interesting example, however, is LiV_2O_5, because it serves as a coating and a Li-insertion host.[91] Some of the surface treatments previously mentioned, such as $Na_2S_2O_8$ and HNO_3, can also reduce the IRC as they chemically remove Li_2O, causing a surface structural transformation, which essentially serves as a coating layer.[104, 125]

Altering the material composition can also have beneficial effects in reducing the IRC. Substituting Ru for Mn has been found to markedly reduce the IRC, presumably due to the reduced Li_2MnO_3 character of the material.[126] Tarascon *et al.* also significantly reduced the IRC by developing another family of LLO materials, Sn-doped Li_2RuO_3.[34] The low IRC is due to the large Sn^{4+} ions that resist TM migration and the ability of Ru^{4+} to promote reversible oxide-ion oxidation, which reduces oxygen loss and vacancy formation. The IRC can also be reduced by altering the cycling protocol. Van Bommel *et al.* used stepwise charging to reduce the IRC by maintaining more oxygen vacancies after the oxygen-loss plateau.[127] Multiple groups have also found that cycling at higher temperatures decreases the IRC significantly, but this may be due to increased side reactions with the electrolyte instead of increased Li reinsertion.[128, 129] A recent study by Shunmugasundaram *et al.* used the novel idea of synthesizing LLO materials with metal site vacancies to considerably reduce the IRC.[130] By inducing metal site vacancies, they created a material that is Li-rich by having a Li:TM ratio greater than 1 and exhibiting an oxygen-loss plateau, but it is structurally analogous to traditional layered oxides due to the lack of Li^+ ions in the TM layer. These built-in metal vacancies still allow for near complete Li reinsertion even after some structural densification occurs.

1.4.4. Volumetric Energy Density

The final hurdle to LLO commercialization is their low volumetric energy density, which is caused by a combination of voltage decay, capacity fade, and often

small particle size. Voltage decay refers to the gradual structural transformation of the LLO material to a spinel-like phase, which results in reduced operating voltage. Readers can refer to Section 3.4.1 for a thorough discussion on this topic. The capacity fade of LLOs proceeds through multiple mechanisms: Li^+ ions react and become trapped in the SEI layer, HF molecules created by trace amounts of water reacting with the electrolyte attack the particles leading to TM dissolution (primarily Mn^{3+}), repeated volume change during cycling can lead to material loss, and the structural transformation to the spinel-like phase.[59, 86, 131, 132] The poor rate capability of LLOs, caused by the low Li diffusion rate in the Li_2MnO_3 component, leads researchers to synthesize smaller particles, which tend to be less dense.[133] These smaller particles have a higher surface area, which leads to increased reactivity with the electrolyte, a thicker SEI layer, increased oxygen loss, and enhanced layered-to-spinel transformation, which speeds up voltage decay.[132]

A myriad of solutions have been attempted in order to improve the volumetric energy density by increasing the particle density or by minimizing the capacity fade. Two simple methods, stepwise precycling and the use of electrolyte additives, do not require altering the LLO material at all. Electrochemical precycling has been mentioned before as a way to reduce the IRC, but the process also reduces capacity fade. Studies by Ito *et al.* and Nakahara *et al.* have shown that stepwise traversing of the oxygen-loss plateau can reduce microcrack formation at the surface and may promote the reversible oxidation of oxide ions, both of which enhance cyclability.[134-136] In order to fully activate the Li_2MnO_3 component of LLOs, cells must be cycled above 4.5 V, which is outside of the electrolyte stability window, so it decomposes and reacts with the cathode, leading to

capacity fade and other negative outcomes. Electrolyte additives have been studied extensively in order to reduce this issue, as they are a relatively inexpensive and simple method of improving the cyclability of LLOs. They are often large organic molecures, and some examples are lithium organo-phosphates and lithium organo-borates.[137-147] They promote better electrochemical performance by inhibiting electrolyte decomposition derived from both the high voltage and reactions with the superoxide ions created during the oxygen-loss plateau, acting as an HF scavenger in order to suppress TM dissolution, and forming a more stable and less insulating SEI layer.[138]

Another approach to decreasing the capacity fade is by surface coating. The topic of surface coating should be familiar to the reader by now, as it has previously been discussed how surface coating can alleviate the LLO issues of poor rate capability and large first cycle IRC. With regards to capacity fade, however, surface coating is effective because it reduces electrolyte decomposition, which leads to the creation of a thinner and more robust SEI layer containing less Li^+ ions. It also impedes surface attacks, such as TM dissolution, etching, and pitting that lead to material loss, by absorbing HF molecules.[73] There are numerous examples of coatings that reduce the capacity fade, including the previously discussed carbon-based, metal phosphates, AlF_3, and metal oxides.[73, 84, 86, 87, 90, 91, 95, 96, 100, 101] One drawback to coatings, however, is that they often reduce the energy density compared to the pristine material.

Moreover, the volumetric energy density can also be increased by altering the synthesis method or parameters in order to minimize the capacity fade or to create larger and denser particles without sacrificing rate capability. Researchers have frequently

found that producing particles that are more uniform in size, morphology, and composition, as well as more crystalline, leads to an increase in cyclability. The common methods of LLO synthesis are co-precipitation and sol-gel; however other techniques, such as combustion, organic co-precipitation, and hydrothermal-assisted synthesis can enhance cyclability.[59, 60, 148-150] Zheng *et al.* used a hydrothermal-assisted synthesis method to great success.[59] Energy dispersive spectroscopy (EDS) showed that Ni segregated to particle surfaces in the samples made by co-precipitation and sol-gel synthesis. In the hydrothermal-assisted materials, there was a uniform distribution of Ni throughout the particles, which led to decreased side reactions with the electrolyte and excellent cyclic stability.

A more promising area of research is in hierarchical structures, which are micron-sized secondary particles composed of nano-sized primary particles. The aim of these structures is to combine the often enhanced rate capability of nanoparticles with the decreased electrode/electrolyte side reactions and higher density of the micron-sized particles. Several studies have found novel ways of synthesizing hierarchical structures with varying degrees of success of producing high discharge capacity, rate capability, and cyclability.[133, 151-158] Zhang *et al.* utilized an ionic interfusion method to synthesize uniform spherical secondary particles composed of nanoplates preferentially oriented to expose planes with facile Li^+ diffusion paths, which lead to superior cyclic stability and rate capability.[151] Oh *et al.* used a co-precipitation method followed by hydrazine surface treatment to create dense 10 micron particles made of flake-like primary particles.[133] The hydrazine treatment formed a spinel-like phase on the surface, and the material exhibited

excellent density and electrochemical performance. Some representative images and electrochemical data of Zhang's and Oh's hierarchical structures can be found in Figure 1.5.

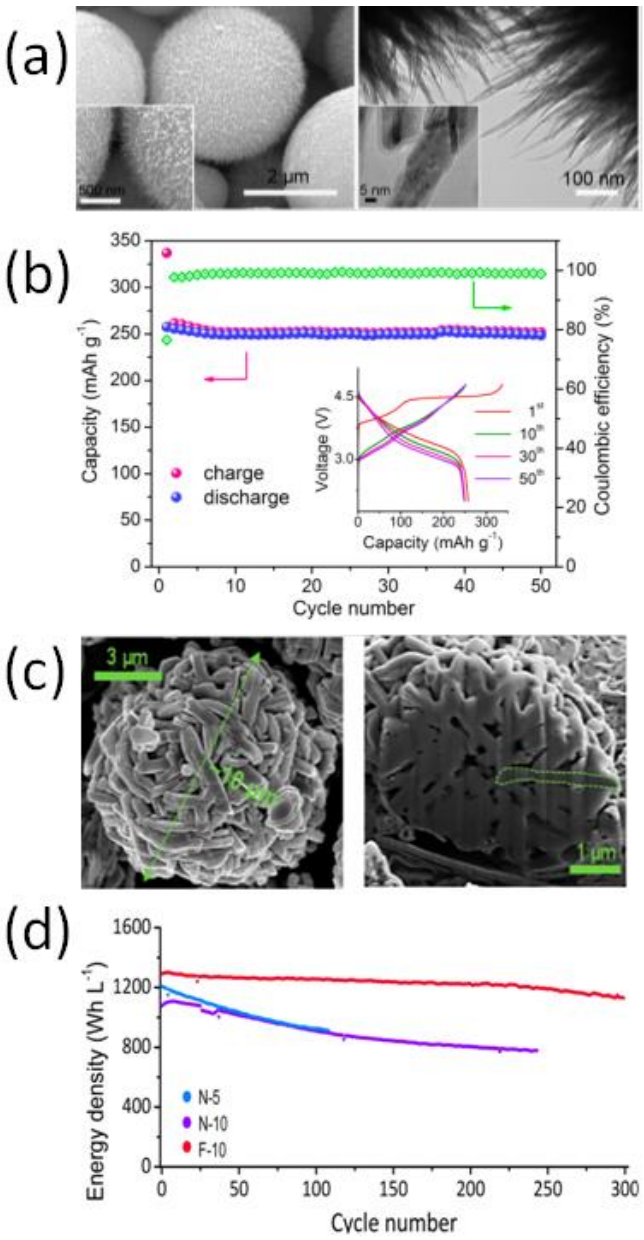

Figure 1.5. (a) Field-emission SEM images of $Li_{1.2}Mn_{0.54}Ni_{0.13}Co_{0.13}O_2$ hierarchical structures synthesized using an ionic interfusion method. Reproduced with permission.[151] Copyright 2014 American Chemical Society. (b) Cyclability and Coulomic efficiency plots showing the excellent cyclic stability of particles seen in part (a). (c) SEM images of pristine (left) and cross-sectioned (right) $Li_{1.2}Mn_{0.6}Ni_{0.2}O_2$ hierachrical structure synthesized using a modified co-precipitation method. Reproduced with permission.[133] Copyright 2014 American Chemical Society. (d) Plot illustrating the increased and stabilized energy density produced by the images seen in part (c).

1.5. Conclusions and Future Directions

LLOs are a candidate to replace the current crop of Li-ion battery cathodes due to their large discharge capacity of 250 – 300 mAh g^{-1}. They have a complex structure, as they can be viewed as a combination of Li_2MnO_3 and $LiMO_2$, and, depending on synthesis conditions and composition, they can form either a single phase solid solution or a nanocomposite. LLOs also possess a very unique two-part first charge profile that consists of an intial region where the TM ions are oxidized, which is followed by a long plateau, where oxide ions are oxidized. Some oxide ions are irreversibly oxidized and lost from the structure, while others are reversibly oxidized and contribute to the high discharge capacity. Some of the oxygen and Li vacancies created during the first charge are then eliminated through TM migration, which leads to a large first cycle IRC, creation of reduced Mn^{3+} ions, and a gradual transformation of the material to a spinel-like phase and subsequent voltage decay.

However, there are considerable challenges inherent to LLOs, including the aforementioned voltage decay and IRC, as well as low rate capability due to the Li_2MnO_3 component and low volumetric energy density. Researchers have devised several strategies to resolve these issues. New synthesis methods have been developed to produce more homogenous particles and hierarchical structures that exhibit strong electrochemical performance and dense particles. The composition can be altered by adjusting the ratio of the Li_2MnO_3 and $LiMO_2$ phases or cation substitutions, which, when done intelligently, can have positive impacts on the voltage decay, IRC, and rate capability concerns. Surface modification through coating or chemical treatment can

significantly enhance the electrochemical performance of LLOs by stabilizing the structural framework and protecting the particle surface from negative reactions with the electrolyte. Other solutions to mitigating the negative properties of LLOs include changing the cycling parameters, using electrolyte additives, and creating composite materials by blending LLOs with other compounds.

The approaches mentioned in this progress report have partially mitigated some of the challenges posed by the LLO materials; however, substantial improvements are still required in order for these materials to move to the commercial level. Multiple studies have investigated the local structure, but there is still no consensus amongst researchers. That disagreement is due in part to the various synthesis procedures and compositions used in the studies. A clearer understanding of the local structure, particularly the Li/TM ordering, with respect to synthesis conditions and composition is required. This will require a combination of characterization techniques, such as HAADF-STEM, neutron diffraction, Raman spectroscopy, and EDS, amongst others. Once a thorough understanding of the local structure is gathered, it can inform the expanding studies of the cycling mechanism and electrochemical properties. Completely elucidating the cycling mechanism, specifically the first charge-discharge cycle, is the next crucial step in LLO development because all of the electrochemical properties tie back to the unique first cycle behavior. Specifically, the prevalence and mechanism of reversible oxide-ion oxidation and how it is affected by local structure and composition is of prime importance. Other points of emphasis should be the fate of O_2 gas and oxide radicals upon removal from the cathode, figuring out how the various types of vacancies are

created and eliminated, and the process of TM and Li migration in the structure. One potential method of investigating the cycling mechanism is to look further into the results of high temperature cycling. LLOs have exhibited discharge capacities of 310 – 350 mAh g^{-1}, which is above the theoretical limit, when cycled at 55 °C or above.[35, 128] If this unexpected capacity is not due to electrolyte oxidation or proton exchange, then this behavior could provide insight into the room-temperature mechanism as well.

Also, more work needs to be done to solve the major drawbacks of LLOs. Surface coating has repeatedly been shown to improve the discharge capacity, cyclic stability, and rate capability, while reducing the IRC, but it has not been as effective at mitigating the voltage decay phenomenon, meaning this process also takes place in the bulk material. Other methods need to be developed to combat the TM migration, vacancy elimination, and subsequent phase transformation in order to halt voltage decay. Additional synthesis of hierarchical structures with new morphologies should be pursued, as they have shown the most promise in raising the volumetric energy density of LLOs. Several newer areas of LLO research are also ripe for further exploration. Electrolyte additives were briefly discussed previously, but development of new additives could greatly enhance the electrochemical performance of these materials, particularly if they were electroactive and could collect oxygen ions before they partake in negative side reactions. It may be possible to find enhanced performance and new insights in materials that are not based on the Li_2MnO_3-$LiMO_2$ system, such as how Tarascon *et al.* have developed Li_2RuO_3-based materials.[33, 34, 45, 46] Thermal stability is another area that should be further explored in LLOs. When charged to high voltages, LLOs have poor

thermal stability due to the oxygen lost from the structure.[159] This effect can be mitigated to some extent by synthesizing larger particles or coating the particles, both of which reduce the side reactions that lead to thermal runaway reactions.[95, 99, 100, 159] More in depth research, however, is required on this topic.

The number of full cell studies is limited, so more should be undertaken, as this is another obstacle towards commercialization and phenomena seen in half cells may not always match those seen in full cells.[50, 160] Unfortunately, this may add to the list of LLO problems that need to be addressed. $Li_{1.2}Mn_{0.6}Ni_{0.2}O_2$ is often seen as the "base" LLO composition, so it is frequently the subject of advanced structural studies and new synthesis techniques. This composition has a lower capacity, however, due to the lack of Co substitution. Cation substitution can significantly affect local structure and particle morphology, so while it is certainly wise to understand the "base" material before modifying it, more analyses should be completed on Co-substituted compositions and other higher capacity LLOs, as they are more likely to be the materials that are of commercial interest. Exploring the synergistic effects of techniques presented in this report should also be pursued. For example, an electrolyte additive may eliminate the capacity fade found in a dense material with superior rate capability produced by a novel synthesis procedure, thus mitigating multiple shortcomings of LLOs. Interested readers can find further discussion of the current research on LLOs in these review papers.[78, 161]

1.6 OBJECTIVES

The primary objective of this dissertation is to develop a more comprehensive understanding of the electrochemical properties and ion-exchange mechanisms of Li-rich layered oxides and spinel oxides. After the experimental details are discussed in Chapter 2, the first half of the dissertation focuses on Li-rich layered oxides, while the second half discusses spinel oxides.

Chapter 3 discusses the effect of Ru substitution on the first charge-discharge cycle of Li-rich layered oxides. This is carried out by doping various amounts of Ru^{4+} for Mn^{4+} in a common Li-rich layered oxide composition. Structural effects are studied with XRD, Rietveld refinement, and SEM imaging. The electrochemical effects are measured by cycling the materials once from 4.8 to 2.0 V. The first cycle behavior is studied with the first charge-discharge profiles, the dQ/dV profiles, and GITT measurements.

Chapter 4 investigates the effect of increasing the Ni oxidation state in Li-rich layered oxides systematically from 2+ to 3+, with several values in between. XRD and Rietveld refinement are used to analyze the structural changes. Electrochemical analysis is carried out on cells after extended cycling from 4.8 to 2.0 V. Particular attention is paid to the first charge-discharge profiles, cyclability, dQ/dV plots, and voltage decay.

Chapter 5 focuses on the lithium-extraction mechanism of Li-spinels with acids and the effect of the average oxidation state of Mn on it. The average Mn oxidation state in samples is controlled by doping other transition-metal ions for Mn. These materials

were structurally and chemically analyzed before and after the acid treatment. The methods used included XRD, ICP, and iodimetric titration.

Chapter 6 builds off of Chapter 5 by examining the extraction mechanisms of Mg and Zn from spinel oxides. Various Mg-spinels are synthesized by altering the degree of cation disorder, Mg content, and dopant ions. Zn-spinels are synthesized with various amounts of Ni-doping. Similar to Chapter 5, the materials are evaluated before and after the treatments with XRD and ICP analysis.

Chapter 7 provides an overall summary of the findings of this dissertation and future directions.

Chapter 2: Experimental Procedures

2.1 Materials Synthesis Procedures

An overview of the materials synthesis procedures used in this dissertation is given below. Complete synthesis details are given in the specific chapters.

2.1.1 Co-precipitation Synthesis

The samples used for the Ru doping of LLO in Chapter 3 were prepared by a hydroxide co-precipitation process. The necessary amounts of Mn and Ni acetates were dissolved in deionized (DI) water and added to a potassium hydroxide solution to precipitate a mixed-metal hydroxide. This powder was filtered, dried, ground together with RuO_2, and calcined to produce the final material.

2.1.2 Sol-gel Synthesis

Two different types of sol-gel synthesis were used for materials in this dissertation. The first method was used to produce the Li-spinel samples referred to in Chapter 5. Required amounts of lithium, manganese, nickel, iron, and cobalt acetates and chromium nitrate were dissolved into DI water. This solution was added to another solution of citric acid, ethylenediaminetetraacetic acid (EDTA), and ammonium hydroxide. The solution was heated at low temperature to evaporate the solvent and remove the residual organic compounds. Then the resulting powder was heated to high temperatures to produce the final material.

The second sol-gel synthesis is a simplified method, and it was used to produce the LLO samples in Chapter 4 and the Mg-spinels in Chapter 6. A single solution containing the metal acetates and the citric acid was prepared, without using any EDTA and ammonium hydroxide. The solution was then heated just as in the previous method to procure the final material.

2.1.3 Oxalate Decomposition Synthesis

Oxalate decomposition was used to prepare the Zn-spinels in Chapter 6. A metal acetate solution was added to a warm oxalic acid solution and stirred under heat for an hour. The product was filtered, dried, and heated to high temperatures to prepare the final materials.

2.2 MATERIALS CHARACTERIZATION

2.2.1 X-ray Diffraction

Several characterization methods were used on the materials in this dissertation. XRD was carried out on a Rigaku Ultima IV and a Rigaku Miniflex 600 in the range of 10° – 80° with Cu Kα radiation. The phases and lattice parameters were determined with the Rigaku PDXL software. Some samples were further analyzed by Rietveld refinement, which was carried out using the GSAS and EXPGUI programs.

2.2.2 Scanning Electron Microscopy

Scanning electron microscopy (SEM) with a JEOL JSM-5610 equipment was used for imaging samples.

2.2.3 Compositional Analysis

Compositional analysis was carried out with inductively coupled plasma optical emission spectroscopy (ICP-OES) on a Varian 715-ES. The powder samples were dissolved in a 3 : 1 mixture of hydrochloric and nitric acids and then diluted for analysis. The equipment was calibrated using four standards made in house.

2.2.4 Infrared Spectroscopy

Fourier transform infrared spectroscopy (FTIR) analysis was utilized in Chapter 6. The samples were pelletized with KBr and measured with a Thermo Fisher Scientific Nicolet iS5 instrument.

2.2.5 Oxygen Content Analysis

Iodimetric redox titration was used to determine the oxygen content of the samples in Chapter 5. Samples were weighed out and dissolved in a solution of potassium iodide and hydrochloric acid. Sodium thiosulfate was then used to titrate the liberated iodine with a starch solution as an indicator.

2.3 ELECTROCHEMICAL MEASUREMENTS

2.3.1 Cell Preparation

CR 2023 coin cells were prepared to test the LLO samples in Chapters 3 and 4. Cathodes were prepared by making a slurry containing 80 wt.% active material, 10 wt.% Super P conductive carbon, and 10 wt.% polyvinylidene difluoride and then coating it onto an aluminum foil. The cells were assembled in an Ar-filled glovebox. The separators were Celgard polypropylene, and the electrolyte was 1 M $LiPF_6$ in a 1 : 1 (v/v) mixture of ethylene carbonate and diethyl carbonate. Lithium metal was used as the anode, and nickel mesh was used as a spacer.

2.3.2 Cell Testing

The coil cells were cycled galvanostatically on a BT-2000 Arbin test system. The LLO cells were cycled from 4.8 to 2.0 V at various rates (C/50, C/25, or C/10), usually for 50 cycles.

2.3.3 Open-circuit Voltage Testing

In order to test for the open-circuit voltages during cycling, galvanostatic intermittent titration technique was used. Cells were cycled at a C/10 rate for 10 min, which was then followed by a 40 min rest.

2.4 Ion Extraction Techniques

2.4.1 Acid Treatment

Acid treatment was used in order to attempt to extract ions from the spinel structure. 0.25 g of the sample was stirred with 25 mL of 0.35 N H_2SO_4 for 24 h, filtered, and dried.

2.4.2 Chemical Treatment

Chemical treatment with nitronium tetrafluoroborate (NO_2BF_4) was also used in order to attempt to extract ions from the spinel structure. A flask containing 0.25 g of the sample was taken into an Ar-filled glovebox, where NO_2BF_4 was added and the flask was sealed. Acetonitrile was then added and the liquid was stirred for 24 h before being filtered with acetonitrile and acetone and then dried.

Chapter 3: Effect of Ru Substitution on the First Charge-Discharge Cycle of Lithium-rich Layered Oxides*

3.1. INTRODUCTION

Since the commercialization of LIBs by Sony in 1991,[162] they have become a ubiquitous part of modern society by powering cell phones, laptops, tablets, music devices, and even automobiles. The most commonly utilized LIB cathodes are $LiCoO_2$, $LiMn_{1/3}Ni_{1/3}Co_{1/3}O_2$, and $LiMn_2O_4$, but recently there has been significant interest in high-voltage cathodes, mainly the 4.7 V spinel $LiMn_{1.5}Ni_{0.5}O_4$[163] and LLOs $Li[Mn_{1-x-y-z}Ni_xM_yLi_z]O_2$[161] systems. The LLO system is particularly interesting because it provides significantly higher capacities of 250 – 280 mAh/g, but it suffers from a myriad of problems, such as capacity fade, poor rate capability, a large first cycle irreversible capacity loss, and significant voltage decay upon extended cycling. There is considerable debate on the structure of LLO, particularly on whether it is a true solid solution of Li_2MnO_3 and $LiMO_2$ or a nanocomposite of these two materials.[10, 13, 18, 164] LLO exhibit a specific first charge profile unlike any other LIB cathode material, where there is an initial sloping region corresponding to the oxidation of TM ions, followed by a plateau region caused by the oxidation of the oxide ions.[42] The oxygen-loss plateau occurs only during the first charge, and it is responsible for the higher reversible capacity of LLO; subsequent charge cycles consist only of a sloping region. Because the unique first-

* Portions of this chapter have been previously published as J. C. Knight, P. Nandakumar, W. H. Kan, and A. Manthiram, "Effect of Ru Substitution on the First Charge-discharge Cycle of Lithium-rich Layered Oxides", *Journal of Materials Chemistry A*, 2015, **3**, 2006-2011.
J. C. Knight carried out the experimental work with assistance from P. Nandakumar. W. H. Kan carried out the Rietveld refinement work. A. Manthiram supervised the project. All participated in preparing the manuscript.

charge characteristics are the cause of LLO's high capacity, several studies have focused on understanding the complex processes occurring during first charge.[31, 34, 43, 120]

One way researchers have probed the first-charge process is by substituting various TM ions for Mn^{4+} and Ni^{2+} ions.[11, 22, 39, 126, 165, 166] An interesting dopant is Ru^{4+} because the $Ru^{4+/5+}$ couple is electrochemically active, and Li_2RuO_3 is almost isostructural with Li_2MnO_3. The Li_2MnO_3 structure is monoclinic C2/m, while the Li_2RuO_3 structure is monoclinic *C2/c* or *P12/m*.[167] A couple of studies have focused on the solid solutions of Li_2MnO_3 and Li_2RuO_3,[33, 168] but there has not been much study on the effect of Ru^{4+} substitution in the LLO systems;[8, 126, 169] the work carried out has been with small amounts of Ru substitution. It has been found that the effect of TM substitution on the oxygen loss plateau is largely influenced by the overlap of the TM:*n*d band with the oxygen:2p band.[11] James and Goodenough[170] showed that the Ru:4d band significantly overlaps with the oxygen:2p band in Li_2RuO_3. Thus, the substitution of Ru is an interesting approach to increase the oxygen loss plateau similar to that found with Co^{3+}.[11, 39] Accordingly, we present here a systematic study of the effect of Ru^{4+} substitution for Mn^{4+} on the first charge-discharge characteristics of a common LLO composition, $Li_{1.2}Mn_{0.6}Ni_{0.2}O_2$, to produce the LLO series $Li_{1.2}Mn_{0.6-x}Ru_xNi_{0.2}O_2$ ($0 \leq x \leq 0.6$).

3.2. EXPERIMENTAL

3.2.1. Synthesis

The material synthesis began with a basic co-precipitation method. Required amounts of Mn and Ni acetate were dissolved in water and added dropwise to a stirring aqueous KOH solution at room temperature with no pH control. After the acetate solution was fully added, the resulting mixed-metal hydroxide particles were filtered, washed with de-ionized water, and dried overnight at 100 °C. The mixed-metal hydroxide powders were then ground together with required amounts of $RuO_2 \cdot xH_2O$ and $LiOH \cdot H_2O$ and fired to 900 °C for 15 h with heating and cooling rates of 3 °C/min and 5 °C/min, respectively. The synthesized materials have the compositions of $Li_{1.2}Mn_{0.6-x}Ru_xNi_{0.2}O_2$ (x = 0.00, 0.025, 0.05, 0.10, 0.20, 0.40, 0.50, and 0.60).

3.2.2. Characterization

Structural characterization was carried out with XRD using Cu K-α radiation with a Rigaku Ultima IV diffractometer in the range of 10 – 80° with a 0.02° step size. Rigaku's PDXL software was used to calculate the lattice parameters. The GSAS program was used to carry out the Rietveld refinement of the x = 0.6 sample.[30] The scale factors, lattice parameters, isothermal temperature factors, background, atomic coordinates, and pseudo-Voight factors were all refined. Compositional analysis was carried out with inductively coupled plasma (ICP) analysis, employing a Varian 715-ES system. Particle size and morphology characterizations were carried out with a JEOL JSM-5610 SEM. Electrochemical characterization was carried out with CR2032 coin

cells. The cathodes were made by casting a slurry of active material (80 wt %), Super P conductive carbon (10 wt %), polyvinylidene fluoride (PVDF) binder (10 wt %), and N-methyl-2-pyrrolidone (NMP) solvent onto an aluminum foil current collector. They were assembled in an Ar-filled glove box with a Li anode, Celgard polypropylene separators, and an electrolyte of 1 M $LiPF_6$ in ethylene carbonate (EC) / diethyl carbonate (DEC) (1:1 by volume). The cells were cycled galvanostatically on an Arbin test station from 4.8 to 2.0 V at a rate of C/50 using 250 mAh/g as the theoretical capacity. The slow rate was chosen to avoid the influence of increased electrical conductivity that is imparted by Ru. Galvanostatic intermittent titration technique (GITT) testing was performed by cycling at a C/10 rate for 10 min, followed by a 40 min rest over the same voltage range.

3.3. RESULTS AND DISCUSSION

3.3.1. Structure and Morphology

The ICP analysis confirmed that the synthesized materials were close to their nominal compositions, with the Li content of all samples at 1.20 ± 0.03. The SEM images of the $Li_{1.2}Mn_{0.6-x}Ru_xNi_{0.2}O_2$ samples shown in Figures 3.1a-h reveal that the average particle size increases as the Ru-content increases. The XRD patterns of the synthesized materials are displayed in Figure 3.2. The samples up to $x = 0.2$ all have the expected LLO pattern, where most of the peaks could be indexed with the α-$NaFeO_2$ structure (trigonal $R\bar{3}m$ space group). Additional weak peaks in the 20 - 25° range correspond to superlattice peaks due to the ordering of TM and Li ions in the TM layer. New peaks at ~ 32°, 42°, and 56° as well as a large increase in several peak intensities are

observed in the high Ru-content samples ($x \geq 0.40$), suggesting the formation of a different phase. The zoomed-in portion of Figure 3.2 illustrates the large intensity increase seen in the highly doped samples. The peaks shift to lower 2θ values as x increases due to the substitution of the larger Ru^{4+} ions (0.62 Å) for Mn^{4+} ions (0.53 Å). In order to better understand the phase change that occurs, the lattice parameters are plotted in Figure 3.3. Figure 3.3a depicts the lattice parameters based on the trigonal $R\bar{3}m$ space group and Figure 3.3b shows them based on the monoclinic *P12/m* space group. The lattice parameters increase linearly with Ru content in the trigonal system until the $x = 0.4$ sample, suggesting a solid solution, but shift significantly at higher Ru contents. The monoclinic system, however, exhibits erratic behavior at low Ru content but a relatively linear increase for $x \geq 0.05$. The results suggest that at low Ru content ($x < 0.05$), the materials can be best described by the trigonal $R\bar{3}m$ phase, while at moderate Ru content ($0.05 \leq x \leq 0.4$), they are a mixture of $R\bar{3}m$ and *P12/m* phases, and at high Ru content ($x \geq 0.4$), the materials appear to have significant amounts of monoclinic *P12/m* similar to Li_2RuO_3. It should be noted, however, that the LLO samples have complicated atomic structures, and advanced TEM analysis is required to fully elucidate the phase(s) of any particular sample. The *P12/m* space group has several additional peaks and other peaks that have increased intensities compared to the $R\bar{3}m$ space group, so this phase evolution accounts for all of the differences in the XRD data between the low- and high-Ru content samples.

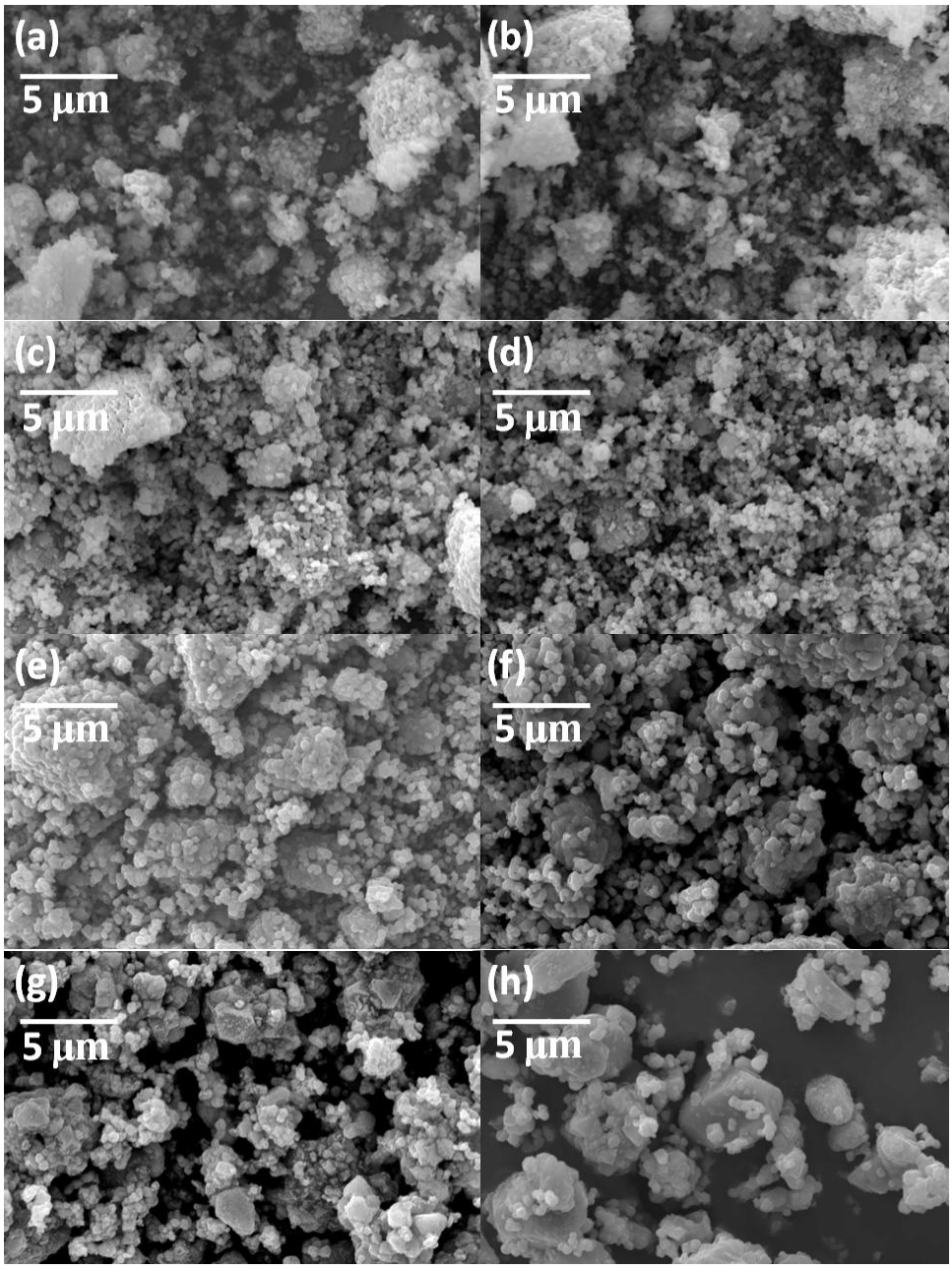

Figure 3.1. SEM images of $Li_{1.2}Mn_{0.6-x}Ru_xNi_{0.2}O_2$ series: (a) $x = 0.00$, (b) $x = 0.025$, (c) $x = 0.05$, (d) $x = 0.10$, (e) $x = 0.20$, (f) $x = 0.40$, (g) $x = 0.50$, and (h) $x = 0.60$.

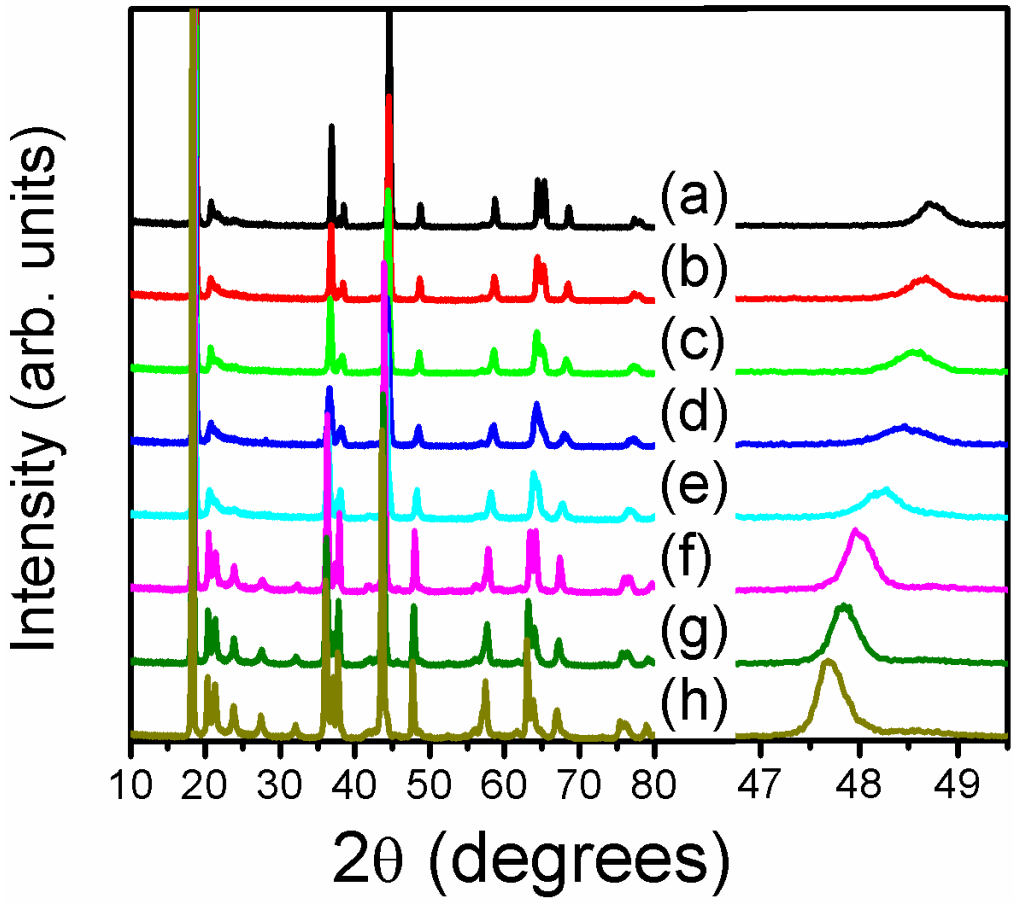

Figure 3.2. XRD patterns of the $Li_{1.2}Mn_{0.6-x}Ru_xNi_{0.2}O_2$ series: (a) $x = 0.00$, (b) $x = 0.025$, (c) $x = 0.05$, (d) $x = 0.10$, (e) $x = 0.20$, (f) $x = 0.40$, (g) $x = 0.50$, and (h) $x = 0.60$.

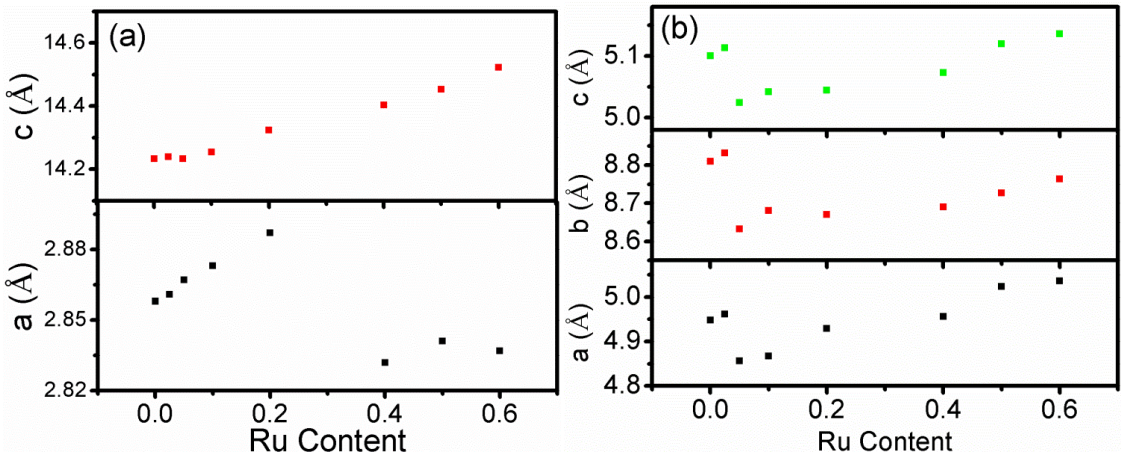

Figure 3.3. Lattice parameters of the $Li_{1.2}Mn_{0.6-x}Ru_xNi_{0.2}O_2$ series based on (a) trigonal $R\bar{3}m$ space group and (b) monoclinic *P12/m* space group.

As mentioned in the introduction, Li_2RuO_3 has been described as having either the *C2/c* or *P12/m* monoclinic structure.[167] Both structures consist of a metal layer that contains Li atoms surrounded by six Ru atoms in a hexagonal honeycomb arrangement, but in the *P12/m* structure, one Ru-Ru bond is shorter due to the formation of Ru-Ru dimers.[167] The formation of these dimers will be discussed in greater detail later in the article. In order to determine which structure best fits these materials, Rietveld refinement was carried out on the $x = 0.6$ sample. Generally, the XRD patterns of LLO can best be refined with a combination of $R\bar{3}m$ and a monoclinic phases. Normally, *C2/m* is chosen as the monoclinic phase because most LLO samples are close in composition to Li_2MnO_3, but since the $x = 0.6$ sample is closer to Li_2RuO_3, both the *C2/c* and *P12/m* phases were used and compared. When a model of $R\bar{3}m$ and *C2/c* was used,

the fit was unacceptable with an R_p of 25%; however, when a model of $R\bar{3}m$ and *P12/m* was used, the R_p decreased to an acceptable value of 8.8%, which provides some evidence of Ru-Ru dimer formation. Figure 3.4 displays the entire refined pattern using the $R\bar{3}m$ and *P12/m* model, as well as a zoomed-in portion to show the fitting of the superstructure peaks.

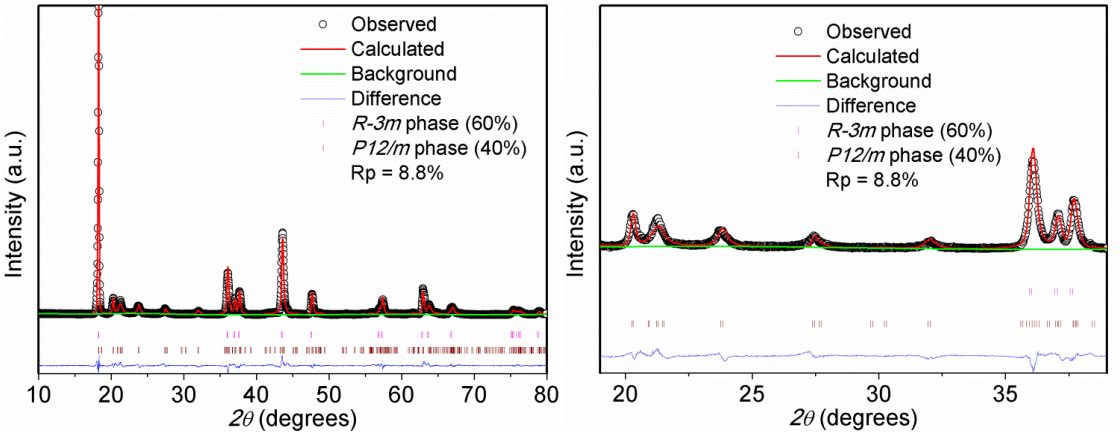

Figure 3.4. Refined XRD patterns of the x = 0.6 sample using a model of $R\bar{3}m$ and *P12/m* phases: (a) full pattern and (b) zoomed-in portion to better show the fit of superstructure peaks.

3.3.2. Effect of Ru-doping on the First Charge-Discharge Cycle

The first charge-discharge profiles of the synthesized materials are presented in Figure 3.5, and the pertinent electrochemical properties are tabulated in Table 3.1. Because Ru is much heavier than Mn, there is a wide range of molar masses (*e.g.*, 85.0298 g/mol for x = 0.00 and 112.712 for x = 0.60) for the materials in this series, so the profiles are presented in terms of the amount of Li removed as opposed to the more

common gravimetric capacity (mAh/g). As mentioned previously, the first charge profile of LLO is broken up into the sloping and plateau regions. The data reveal that the length of the sloping region increases as Ru-doping increases, which is due to the $Ru^{4+/5+}$ redox couple being electrochemically active in this voltage range.[171] On the other hand, the plateau region decreases with increasing Ru content, which will be discussed later. The decrease in the plateau region length is greater than the increase in the sloping region length, so the charge capacity decreases overall, except for a jump at $x = 0.40$. As found in a previous study,[126] the irreversible capacity loss in the first cycle decreases dramatically upon Ru substitution , which is due to the shorter plateau length. Because the plateau region is shorter, less oxygen vacancies are created and subsequently eliminated, so the number of Li sites eliminated at the end of first charge is reduced. The discharge capacities do not follow a general trend due to the competing factors of decreasing charge capacity and decreasing irreversible capacity loss in the first cycle, although samples with high Ru content ($x \geq 0.4$) exhibit the highest discharge capacities. The differential capacity (dQ/dV) plots for the first charge cycle of the samples are shown in Figure 3.6. The peaks in the 3.5 – 3.9 V range correspond to the TM oxidation that initially occurs during cycling, while the peaks in the 4.1 – 4.7 V range represent the oxygen loss plateau. As the Ru substitution increases, several changes occur in the dQ/dV peaks. First, the TM oxidation peak increases in intensity, shifts to lower voltages, and eventually splits into two peaks at high Ru contents. Second, the oxygen loss peak greatly decreases in intensity and shifts to significantly lower voltages. The cause of these effects will be discussed in the next section.

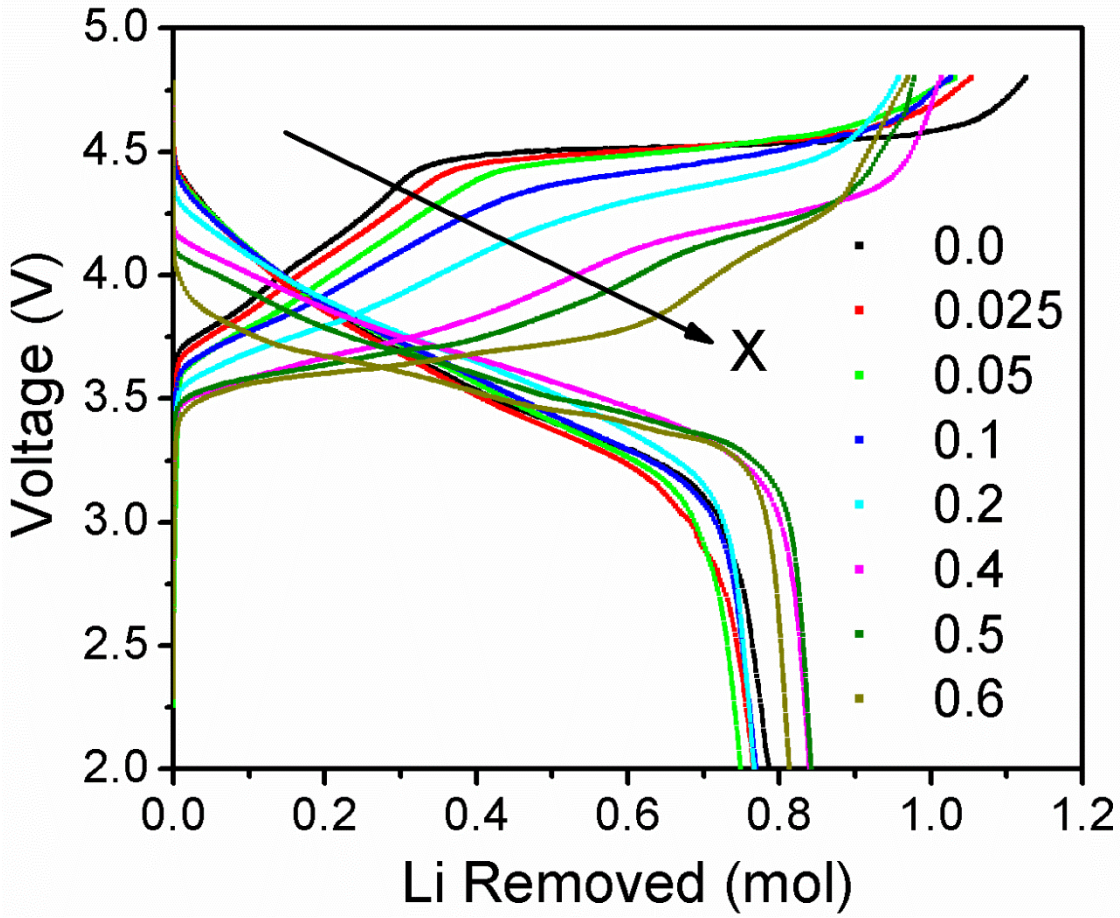

Figure 3.5. First charge-discharge profiles of the $Li_{1.2}Mn_{0.6-x}Ru_xNi_{0.2}O_2$ series.

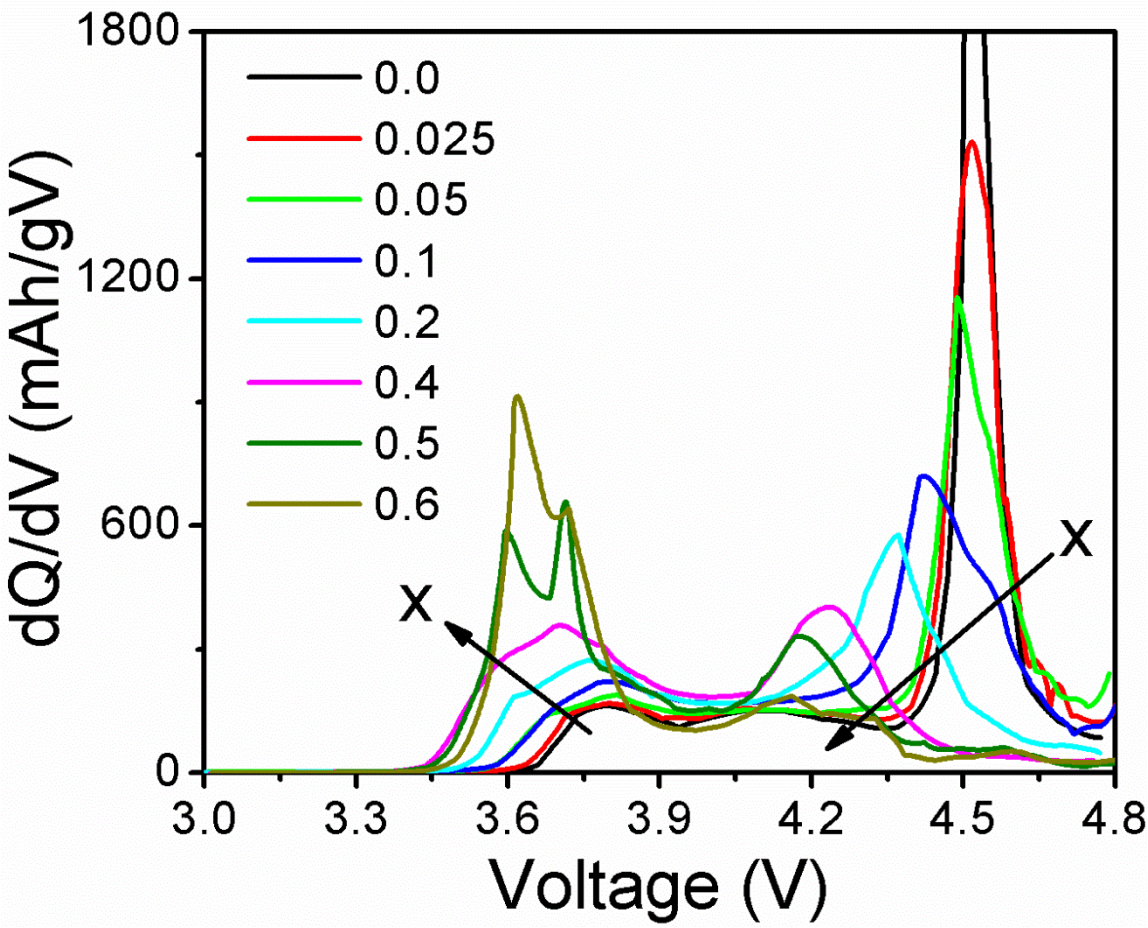

Figure 3.6. Differential capacity (dQ/dV) plots of the first charge cycle of the $Li_{1.2}Mn_{0.6-x}Ru_xNi_{0.2}O_2$ series.

Table 3.1. Summary of the electrochemical data of the $Li_{1.2}Mn_{0.6-x}Ru_xNi_{0.2}O_2$ series

	amount of Li extracted[a]				
x	charge capacity (mol Li)	discharge capacity (mol Li)	irreversible capacity loss (mol Li)	sloping region (mol Li)	plateau region (mol Li)
0	1.126	0.787	0.339	0.35	0.776
0.025	1.054	0.766	0.288	0.40	0.654
0.05	1.032	0.749	0.283	0.45	0.582
0.10	1.026	0.769	0.257	0.50	0.526
0.20	0.958	0.767	0.191	0.55	0.408
0.40	1.014	0.840	0.174	0.60	0.414
0.50	0.978	0.842	0.136	0.65	0.328
0.60	0.970	0.813	0.157	0.75	0.220

[a]These values were calculated from the charge-discharge curves in Figure 3.5. The units are in mol of Li removed due to the large change in molecular weights in this series.

3.3.3. Discussion of the Electrochemical Effects of Ru-doping

The relative positions of the TM and oxygen bands play a critical role in controlling much of the electrochemical behavior of LLO. The fact that the peaks in the dQ/dV plots are shifting in voltage can be explained by one of the two following factors. It could be due to a change in the conductivity of the material, which would affect the cell polarization. The conductivity is certainly increasing as the Ru content increases because Li_2MnO_3 is an insulator,[172] while Li_2RuO_3 is semiconducting/metallic in nature;[170, 171]

however, this effect should be somewhat mitigated by the low C rate used. Therefore, the shifts in the operating voltages could largely be due to the changes in the intrinsic redox energies. In order to confirm that a shift in the redox energy is responsible for the decrease in the TM oxidation voltage, GITT testing was performed on a few samples (x = 0.00, 0.10, and 0.50) and the results are displayed in Figure 3.7. The first open-circuit voltage (OCV) of each cell was assumed to be the onset voltage of TM oxidation. The depth of each voltage drop in the GITT is a measure of the polarization at that state of charge. As the x value increases, the TM oxidation onset voltage decreases from 3.65 V to 3.53 V to 3.42 V, illustrating that the redox energy of the TM is indeed shifting. The polarization of the sloping region decreases slightly between the x = 0.00 and 0.10 samples, but increases in the x = 0.5 sample.

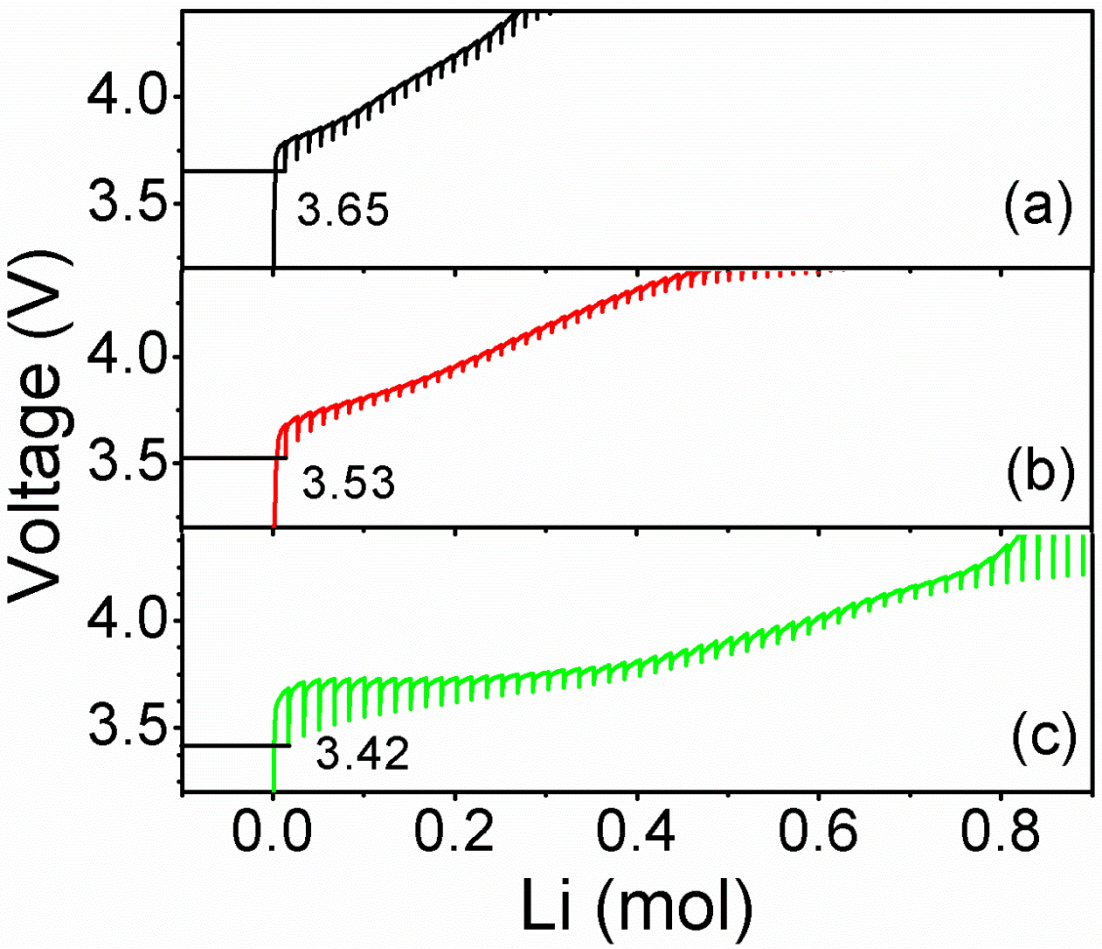

Figure 3.7. Plots of GITT testing data from the first charge cycle of the $Li_{1.2}Mn_{0.6-x}Ru_xNi_{0.2}O_2$ series: (a) $x = 0.00$, (b) $x = 0.10$, and (c) $x = 0.50$.

As Ru-doping increases, the material becomes closer in composition to Li_2RuO_3, so looking at the electrochemical properties of Li_2RuO_3 can help explain the changes seen here. Kobayashi *et al.*[171] found that the $Ru^{4+/5+}$ couple in Li_2RuO_3 proceeds via two plateaus near 3.4 and 3.6 V. This behavior is responsible for the intensity increase and eventual splitting of the TM oxidation peak in the dQ/dV plot as the Ru content increases

and partially explains why the onset voltage of TM oxidation decreases in the GITT data. The two-phase reaction that is occurring during these charge plateaus may also explain the increased polarization seen in the GITT plot of the $x = 0.50$ sample. The other cause of the decreasing TM oxidation onset voltage may be the formation of Ru-Ru dimers. The Rietveld refinement data described earlier presents some preliminary evidence of Ru-Ru dimer formation in this series of materials. Studies have found that Ru-Ru dimers form in Li_2RuO_3[167, 173-175], and the dimerization causes the t_{2g} orbitals to split into bonding and antibonding orbitals. The d_{xy} orbitals, which overlap more directly in the dimerization, experience strong σ bonding/antibonding, while the d_{xz} and d_{yx} orbitals experience weaker π and δ bonding/antibonding.[173] With 8 valence electrons from the two Ru^{4+}:t_{2g}^4 ions, 6 electrons fill the bonding orbitals completely and the last 2 electrons fill the antibonding states, which results in a raising of the Fermi energy compared to the non-dimerized Ru ions. This effect would increase with more Ru substitution as dimerization would occur more as the amount of Ru ions increases. The raising of the Fermi energy explains the decreasing onset voltage of the TM oxidation.

The decrease in the intensity of the dQ/dV oxygen loss-peak arises because as the voltage decreases, the oxidation of oxide ions proceeds concurrently with the oxidation of Ni^{2+} ions, so the oxygen-loss plateau region is actually becoming a separate second quasi-sloping region. Finally, the shortening of the oxygen-loss plateau with higher Ru substitution could possibly be somewhat explained to be due to the increase in particle size with increasing Ru content since a larger particle would decrease Li diffusion and increase polarization loss. The particle size increase leads to a surface area reduction,

which makes it more difficult for oxygen gas to be evolved. The reduction in the amount of oxygen loss may also be due to the band shift caused by Ru-Ru dimerization. By raising the $Ru^{4+/5+}$:4d band, it overlaps less with the O^{2-}:2p band, resulting in a decrease in metal-oxygen covalence and an oxidation/ loss of fewer oxide ions. However, other factors could also play a role, and more detailed future investigations with computational modeling or neutron diffraction could shed more light on this issue.

3.4. CONCLUSIONS

The effect of substituting Ru^{4+} ions for Mn^{4+} ions on the first charge-discharge cycle of the common LLO system $Li_{1.2}Mn_{0.6}Ni_{0.2}O_2$ has been systematically investigated. As Ru substitution increases, primary particle size increases as well, as indicated by SEM analysis. The XRD patterns of the materials with low to moderate Ru contents display the typical LLO pattern, but additional peaks appear in high-Ru content samples. This is explained by the increasing presence of the monoclinic *P12/m* phase as Ru content increases. Rietveld refinement of the $x = 0.6$ sample shows that the *P12/m* phase better models the XRD patterns as opposed to the *C2/c* phase, which provides some evidence of Ru-Ru dimer formation. Although the substitution of Ru would be anticipated to increase the electrochemical performance of the LLO system due to the electrochemical activity of the $Ru^{4+/5+}$ couple and its higher degree of covalent bonding with the oxide-ion framework, the electrochemically active Ru does increase the sloping region length, but the plateau region suffers from a dramatic decrease in length with increasing Ru doping which may be due to the increase in particle size and the formation of Ru-Ru dimers.

The Ru-Ru dimers would raise the $Ru^{4+/5+}$:4d band relative to the top of the O:2p band and consequently decrease the metal-oxygen covalence and oxygen loss plateau length. The addition of Ru to the LLO system causes it to behave electrochemically more like Li_2RuO_3, *i.e.*, the sloping TM oxidation region decreased in voltage and became more plateau-like, while the oxygen-loss plateau also decreased in voltage and became more slope-like, as it proceeded concurrently with the oxidation of Ni^{2+} ions. Overall, the results show that the relative positions of the metal:*n*d and O:2p bands play a critical role in controlling the complex electrochemical properties of lithium-rich layered oxides.

Chapter 4: Effect of Nickel Oxidation State on the Structural and Electrochemical Characteristics of Lithium-rich Layered Oxides*

4.1. INTRODUCTION

Li-ion batteries have been used successfully and extensively as power sources in today's society.[176] They power personal electronic devices, such as cell phones and laptops, and have been scaled up for use in electric vehicles. Significant effort is being put into designing new battery systems, such as Li-sulfur,[177] Li-air,[178] Na-ion,[179] and Mg-ion batteries,[180] but these technologies are not ready yet for practical use. On the other hand, attention is also paid towards improving the energy density of current Li-ion batteries by exploring cathodes and anodes with higher charge-storage capacities. The most common cathodes currently in use are layered Li[Co, Mn, Ni]O_2 oxides, spinel $LiMn_2O_4$, and olivines $LiFePO_4$, but each of them have advantages and disadvantages. Some of the drawbacks include low capacity, low rate capability, thermal instability, and high cost.[176] With respect to increasing the capacity, two of the most promising types of materials are Ni-rich layered oxides and LLOs.[181] Both possess layered oxide structures similar to $LiCoO_2$. Ni-rich layered oxides are essentially $LiNiO_2$ doped with other TM ions. They exhibit higher discharge capacities than other layered oxides (200 – 220 mAh/g) but suffer from reduced thermal stability and increased capacity fade.

* Portions of this chapter have been submitted for publication as J. C. Knight and A. Manthiram, "Effect of Nickel Oxidation State on Structural and Electrochemical Characteristics of Lithium-rich Layered Oxides", *Journal of Materials Chemistry A*, submitted 2015.
J. C. Knight carried out the experimental work. A. Manthiram supervised the research work. Both participated in preparing the manuscript.

LLOs, however, are much more complicated. They possess the same structure as layered oxides, with alternating layers of Li ions and TM ions in the octahedral sites of a cubic-close-packed oxygen lattice, except they have additional Li ions in the TM layer. They can also be thought of as nanocomposites of Li_2MnO_3 ($Li[Li_{1/3}Mn_{2/3}]O_2$ in layered notation) and $LiMO_2$ (M = Mn, Ni, and Co).[23] Their structure is complex, and there is no consensus on its nature.[10, 26-30] LLOs also have a unique first charge-discharge profile that can be broken into two different regions. The first region consists of the TM ions being oxidized to the 4+ state, just like other layered oxides. This region is referred to as the sloping region. The second region is a longer plateau that corresponds to the irreversible oxidation and partial loss of oxide ions from the structure. This is referred to as the oxygen loss plateau, and it is believed to be derived from the Li_2MnO_3 component of the material. At the end of the first charge, oxygen vacancies are formed due to the loss of oxygen from the lattice, so structural rearrangement occurs, causing a loss of oxygen and Li vacancies through densification. This elimination of Li vacancies leads to a large 1st cycle IRC. The first discharge cycle proceeds by reducing the TM ions, bur because of the oxygen loss, an additional species needs to be reduced. Therefore, some Mn^{4+} ions (their initial oxidation state) are reduced to Mn^{3+}. It has recently been suggested, however, that some oxide ions are reversibly oxidized, so they also contribute to the discharge capacity.[15, 31, 32, 44] The Mn reduction and redox active oxide ions lead to a high discharge capacity (250 – 300 mAh/g) in LLOs. This high discharge capacity is why the battery community is so interested in pursuing LLOs.

Unfortunately, LLOs also have several disadvantages. They have low rate capability due to poor Li diffusion kinetics caused by the Li_2MnO_3 component and a low volumetric energy density.[79] As mentioned previously, they also have a large first cycle IRC. The largest hurdle to commercialization, however, is the gradual but significant drop in operating voltage during extended cycling (termed as voltage decay), causing a large drop in energy density with cycling. Extensive research has been carried out to understand the mechanism of voltage decay. It is generally understood that a structural transformation occurs gradually, primarily through the migration of TM ions into Li sites in the TM and Li layers, resulting in the formation of a spinel-like phase.[41, 56, 57, 61-63]

There have been numerous studies focused on reducing voltage decay in LLOs. For instance, Zheng *et al.* found that a hydrothermal-assisted synthesis method leads to higher Ni homogeneity, which stabilizes the LLO structure by increasing Ni-Mn interactions.[59] Lee and Manthiram and Song *et al.* chose compositions with larger sloping regions and smaller oxygen loss plateau regions that experienced less voltage decay because the shorter oxygen loss plateau reduced the amount of cation migration at the end of the first charge.[60, 69] The partial replacement of Li ions with other alkali metals, such as Na and K, was also found to impede the structural transformation to the spinel-like phase, thus reducing voltage decay.[70, 71] Another interesting method of reducing voltage decay is to design compositions with Ni^{3+} ions,[72] which slows the layered-to-spinel transformation, and raises the operating voltage.

However, a more thorough investigation of the effect of Ni oxidation state on LLOs is not available in the literature. Accordingly, with two common LLO

compositions, $Li_{1.2}Mn_{0.6}Ni_{0.2}O_2$ and $Li_{1.2}Mn_{0.54}Ni_{0.13}Co_{0.13}O_2$, we present here an investigation of a systematic increase in the Ni oxidation state by increasing the Ni content. It can be thought of as doping 2 Ni^{3+} ions for a Mn^{4+} and a Ni^{2+} ion. Each series begins with all Ni ions in the 2+ state and ends with all Ni ions in the 3+ state. It should be noted that each composition has the same amount of electroactivity in the sloping region, *i.e.,* the amount of TM oxidation occurring in the sloping region is the same across all compositions. The two series of samples are systematically characterized by structural and electrochemical analysis.

4.2. EXPERIMENTAL

4.2.1. Synthesis

Two series of materials were synthesized: $Li_{1.2}Mn_{0.6-x}Ni_{0.2+x}O_2$ (x = 0, 0.02, 0.05, 0.1, 0.15, and 0.2) series, referred to hereafter as the "undoped series", and the $Li_{1.2}Mn_{0.54-x}Ni_{0.13+x}Co_{0.13}O_2$ (x = 0, 0.04, 0.09, and 0.14) series, referred to hereafter as the "Co series". In each series, the Ni oxidation state increases with increasing x value. When x = 0, the average Ni oxidation state is 2+, and the maximum x value gives an average Ni oxidation state of 3+. Table 4.1 lists the x values and the corresponding average Ni oxidation state in each sample. Both series were synthesized by a solution-based method, where required amounts of manganese acetate (Acros 99+%), nickel acetate (Acros 99+%), cobalt acetate (Acros 98+%), and lithium acetate (Acros 98%) were dissolved in 100 mL of stirring deionized (DI) water. A 2% excess of lithium acetate was used to account for Li loss during high-temperature heating, but the excess

amount of Li acetate had to be increased at higher *x* values due to the difficulty in maintaining a higher Ni^{3+} content at the high synthesis temperatures and the consequent increase in the degree of lithium volatilization. For example, the $x = 0.2$ sample in the undoped series required 11% excess lithium acetate to produce the desired composition. The total amount of TM acetates used was 0.025 mol. Then 0.025 mol of citric acid (Fisher 98%) was added to the same beaker. The solution was then heated until the DI water evaporated, leaving a gel behind. The gel was heated at 450 °C for 5 h in order to boil off the residual organics. This produced a brown powder that was heated at 900 °C for 12 h with heating and cooling rates of 3 °C/min.

Table 4.1. Summary of the first charge-discharge cycle electrochemical data for the undoped and Co-doped series

Series	x Value	Ni Ox. State	Li/Ni Site Mixing	Charge Capacity (mAh/g)	Discharge Capacity (mAh/g)	Slope Capacity (mAh/g)	Plateau Capacity (mAh/g)	IRC (mAh/g)
Undoped	0	2.00+	7.22%	303	245	100	203	58
	0.02	2.18+	6.31%	290	222	105	185	68
	0.05	2.40+	6.27%	281	217	105	176	64
	0.1	2.67+	5.59%	272	192	110	162	80
	0.15	2.86+	5.90%	277	176	130	147	101
	0.2	3.00+	4.48%	274	162	130	144	112
Co-doped	0	2.00+	4.84%	325	253	110	215	72
	0.04	2.41+	2.78%	301	228	110	191	73
	0.09	2.77+	0.98%	294	211	110	184	83
	0.14	3.00+	1.05%	290	195	125	165	95

4.2.2. Characterization

The materials were characterized with several methods. XRD analysis was carried out with a Rigaku Miniflex 600 in the range of 10° – 80° with a step size of 0.02° and a speed of 2°/min using Cu Kα radiation. Further structural analysis was performed with the Reitveld refinement method and the General Structure Analysis Software (GSAS, Los Alamos National Laboratory). ICP analysis was carried out with a Varian 715 ES. Electrochemical measurements were carried out with CR2032 coin cells. The cathode consisted of 80 wt. % active material, 10 wt. % Super P conductive carbon, and 10 wt. % polyvinylidene fluoride (PVDF, Kureha KF 1120) coated onto aluminum foil. The anode was lithium metal, while the separators were polypropylene and the electrolyte (BASF Selectilyte Series) was a mixture of ethylene carbonate (EC) and diethyl carbonate (DEC) (1 : 1 by volume) with 1 M $LiPF_6$. Cells were cycled galvanostatically on an Arbin test system (BT-2000) at a rate of C/10 from 4.8 to 2.0 V.

4.3. Results and Discussion

4.3.1. Structure

Figure 4.1 displays the XRD patterns for the synthesized samples. Figures 4.1a-f are for the undoped series, while Figures 4.1g-j are for the Co series. Each pattern exhibits the typical LLO pattern, where all peaks, except some weak reflections in the 20° - 25° range, can be indexed by the α-$NaFeO_2$ structure with the trigonal $R\bar{3}m$ space group. The small peaks in the 20° – 25° range are superstructure peaks that arise from

Li/Mn ordering in the TM layer. One of the key differences between Ni^{2+} and Ni^{3+} ions is their size difference. Low spin Ni^{3+} ions (0.56 Å) are much smaller than Ni^{2+} ions (0.69Å) and Li^{+} ions (0.76 Å), so Ni^{2+} ions are known to occupy the Li sites in the Li layer. Thus, the addition of Ni^{3+} ions would presumably lead to a decrease in Li/Ni site mixing.[182] Ni ions in the Li layer can impede Li^{+} ion diffusion, leading to decreased rate capability, and it jump starts the layered-to-spinel phase transformation that occurs during voltage decay.[57, 183] Rietveld refinement was carried out on the samples in order to quantify the amount of Li/Ni site mixing. The calculated Li/Ni site mixing can be found in Table 4.1. The amount of site mixing decreases (except in two cases) with increasing Ni oxidation state. This trend occurs despite the fact that as the Ni oxidation state increases, the amount of Ni is also increasing. The decreased site mixing should impede the layered-to-spinel phase transformation and the resulting voltage decay.

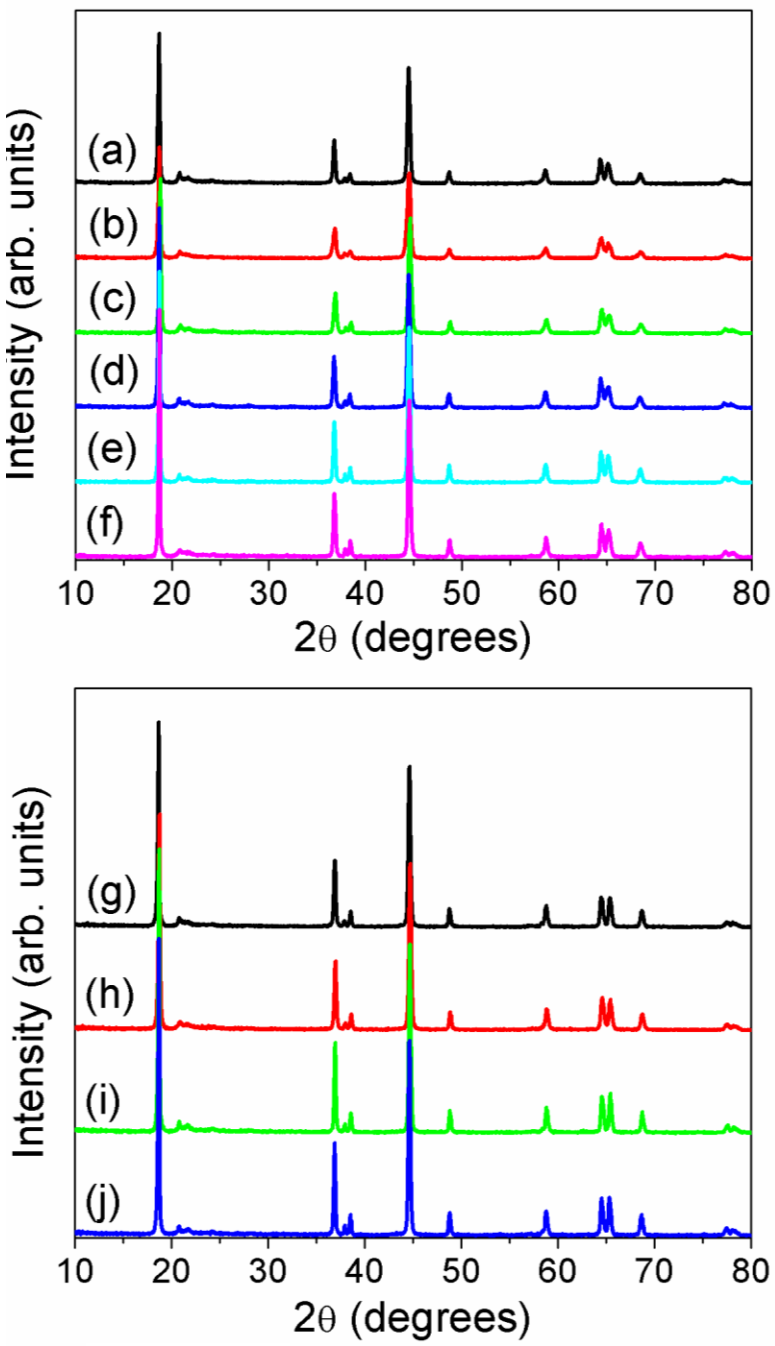

Figure 4.1. XRD patterns of the synthesized materials: $Li_{1.2}Mn_{0.6-x}Ni_{0.2+x}O_2$ (a) $x = 0.00$, (b) $x = 0.02$, (c) $x = 0.05$, (d) $x = 0.10$, (e) $x = 0.150$, and (f) $x = 0.20$; $Li_{1.2}Mn_{0.54-x}Ni_{0.13+x}Co_{0.13}O_2$ (g) $x = 0.00$, (h) $x = 0.04$, (i) $x = 0.09$, and (j) $x = 0.14$.

4.3.2. Electrochemical Analysis

Altering the Ni oxidation state has a more dramatic effect on the electrochemical behavior of LLOs than on the structure. The first charge-discharge cycle is discussed first. Figures 4.2a and 4.2b display the first charge-discharge cycles of the undoped and Co series, respectively. Looking at the undoped series first, it is clear that the sloping region increases with increasing Ni oxidation state. This is most likely due to the reduction in the amount of the insulating Mn^{4+} ions that occurs with increasing *x* value. Also, with increasing *x* value, less Ni is found in the Li layer, resulting in faster Li-ion diffusion. Unlike the sloping-region capacity, however, the plateau-region capacity decreases with increasing *x*. This is most likely due to the reduction in the Mn^{4+} content and decreased Li/Ni site mixing, both of which cause a decrease in the Li_2MnO_3 character of the material. Because the decrease in the oxygen loss plateau region is greater than the increase in the sloping region, the charge capacity generally decreases with increasing *x* value.

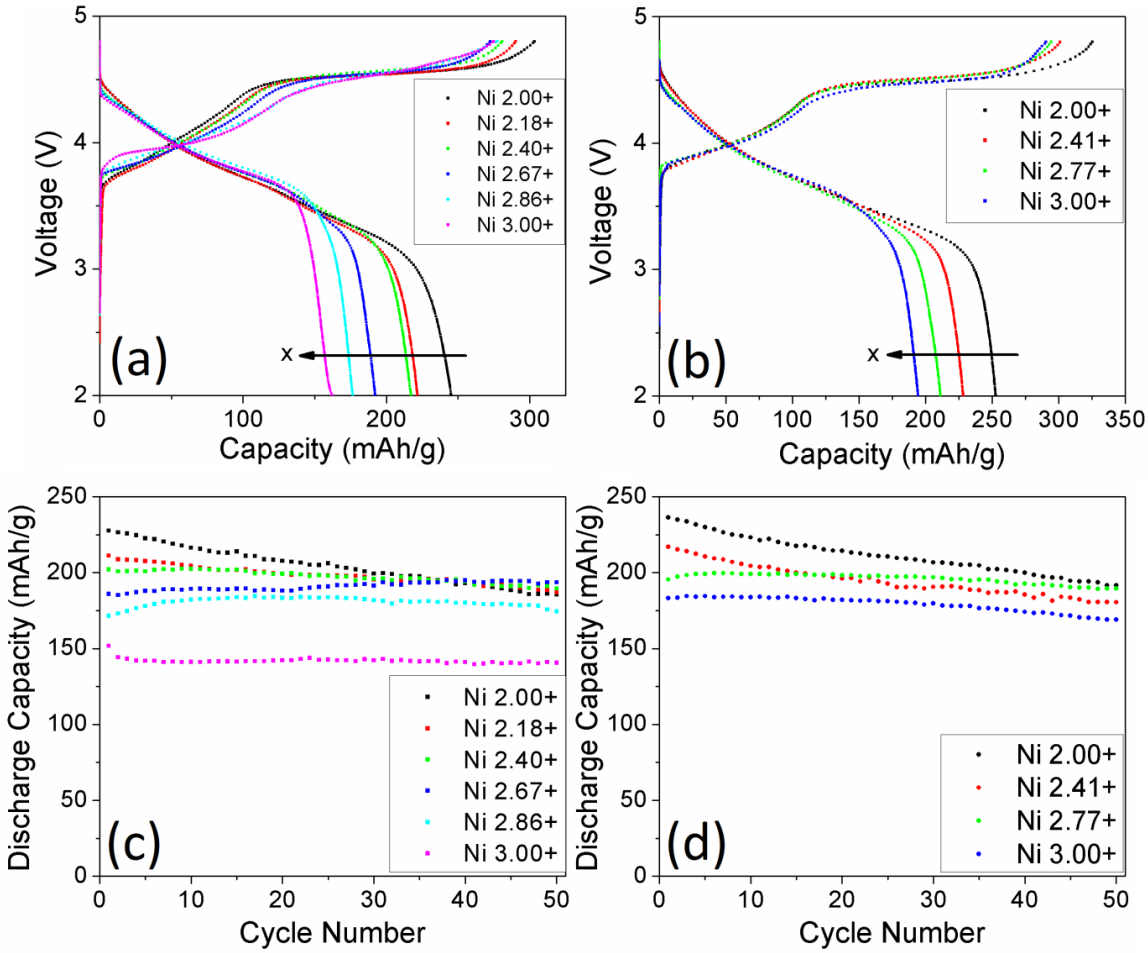

Figure 4.2. First charge-discharge profiles of (a) the undoped series and (b) the Co series. Cyclability plots of the (c) undoped series and the (d) Co series.

Looking at the discharge curves, it is clear that the effect on discharge capacity is very dramatic. Despite the relatively similar charge capacities, the discharge capacities decrease significantly with increasing Ni oxidation state. Almost all of the capacity reduction comes below 3.5 V, which will be discussed further in a later section. The effect is magnified because of an increasing IRC, which is caused by three factors. First,

as mentioned previously, Ni^{3+} ions are smaller in size than Ni^{2+} ions, so it may be easier for them to migrate through the LLO structure at the end of the first charge and thereby densify easily by eliminating more oxygen and Li vacancies, causing a larger IRC. Second, studies have shown that in $LiNiO_2$ a higher amount of the Jahn-Teller active Ni^{3+} ion leads to the formation of an additional hexagonal phase near the end of the first charge cycle.[183, 184] This new phase has smaller interlayer spacing, which causes it to be an electrochemically inactive domain, thus increasing the already large IRC of LLOs. Third, the higher reactivity of Ni with the electrolyte at higher charge voltages, resulting in side reactions, could also contribute to the larger IRC.

The trends seen in the undoped series can also be found in the Co series (Figure 4.2b) as well. The effect is somewhat mitigated, however, because there is less Ni content in the Co series as opposed to the undoped series. The sloping region slightly increases with increasing *x*, while the plateau region and overall charge capacity decrease. The IRC increases and the discharge capacity decreases with increasing Ni oxidation state. Table 4.1 lists the pertinent electrochemical data from the first charge-discharge cycles.

Figures 4.2c and 4.2d show, respectively, the cyclability plots of the materials. As seen before in the first charge-discharge cycle plots, the discharge capacity decreases as the Ni oxidation state increases. This is initially true, but after extended cycling, this trend falls apart because the cyclability of the samples generally increases as the Ni oxidation state increases. For example, in the undoped series, despite initially having a discharge capacity of ~ 40 mAh/g less than that of the Ni^{2+} sample, the $Ni^{2.67+}$ sample has

a higher capacity after 50 cycles due to its superior cyclability. While the samples with a lower *x* value all show significant capacity fade over 50 cycles, the higher *x* value samples show flat or even increasing cyclability plots. This trend also holds in the Co series, although the effect is again reduced due to the lower Ni content in that series. One cause for the reduced capacity fade could be a reduction in TM dissolution. TM ions, particularly Mn, slowly dissolve into the electrolyte during cycling, so the decreased Mn content with increasing Ni content should lead to less metal dissolution and less capacity loss during cycling. Another factor may be the reduction in oxygen loss. Because the oxygen loss plateau is shorter at higher Ni oxidation states, less oxygen gas is released, which could lead to reduced electrolyte reactions and a thinner solid-electrolyte interphase (SEI) layer.

Differential capacity (dQ/dV) plots are helpful to understand the electrochemical processes occurring in cells. The dQ/dV plots of the 1st discharge cycle of the undoped and Co series are shown in Figures 4.3a and 4.3c, respectively. The dQ/dV plots of the 50th discharge cycle of the undoped and Co series are shown in Figures 4.3b and 4.3d, respectively. In the 1st cycle plots, the peaks at ~ 4.3 V and ~ 3.7 V correspond to the reduction of $Ni^{2+/3+/4+}$ and, in the case of the Co series, to the reduction of $Co^{3+/4+}$ as well. The peak at ~ 3.5 V is attributed to the $Mn^{3+/4+}$ reduction that occurs in response to the oxygen loss during the initial charge cycle. Increasing the Ni oxidation state results in significant changes to the 1st cycle dQ/dV plots. As *x* increases, the Ni/Co reduction peaks increase in magnitude and, more importantly, the Mn reduction peak markedly decreases. In fact, for the undoped sample with all Ni^{3+} ions, the Mn reduction peak does

not even show up. Because the Ni content increases with *x*, the Ni/Co reduction peak current increases with increasing Ni oxidation state. The decrease in the Mn reduction peak current has a more complex origin. As *x* increases, the oxygen loss plateau and the capacity values decrease, causing less TM reduction to occur during discharge. Also, Ni reduction occurs at a higher voltage than Mn^{4+} reduction to Mn^{3+}. These two facts, combined with the increased Ni content, result in a significant decline in the amount of Mn^{4+} reduction. The same trends are seen in both the undoped and Co series, although the effect is mitigated in the Co series due to the decreased Ni content compared to that in the undoped series. For instance, in the Co series, the sample with all Ni^{3+} ions still shows some Mn reduction, which is due to the lengthened oxygen loss plateau that Co incorporation produces. An additional benefit of the reduction in Mn^{3+} creation is a corresponding reduction in Mn dissolution. As mentioned previously, Mn^{3+} ions readily dissociate and dissolve into the electrolyte faster than the other TM ions, so by reducing the Mn^{3+} ion creation, the TM dissolution should also be decreased. This may be another cause of the increased cyclability with increasing Ni oxidation state.

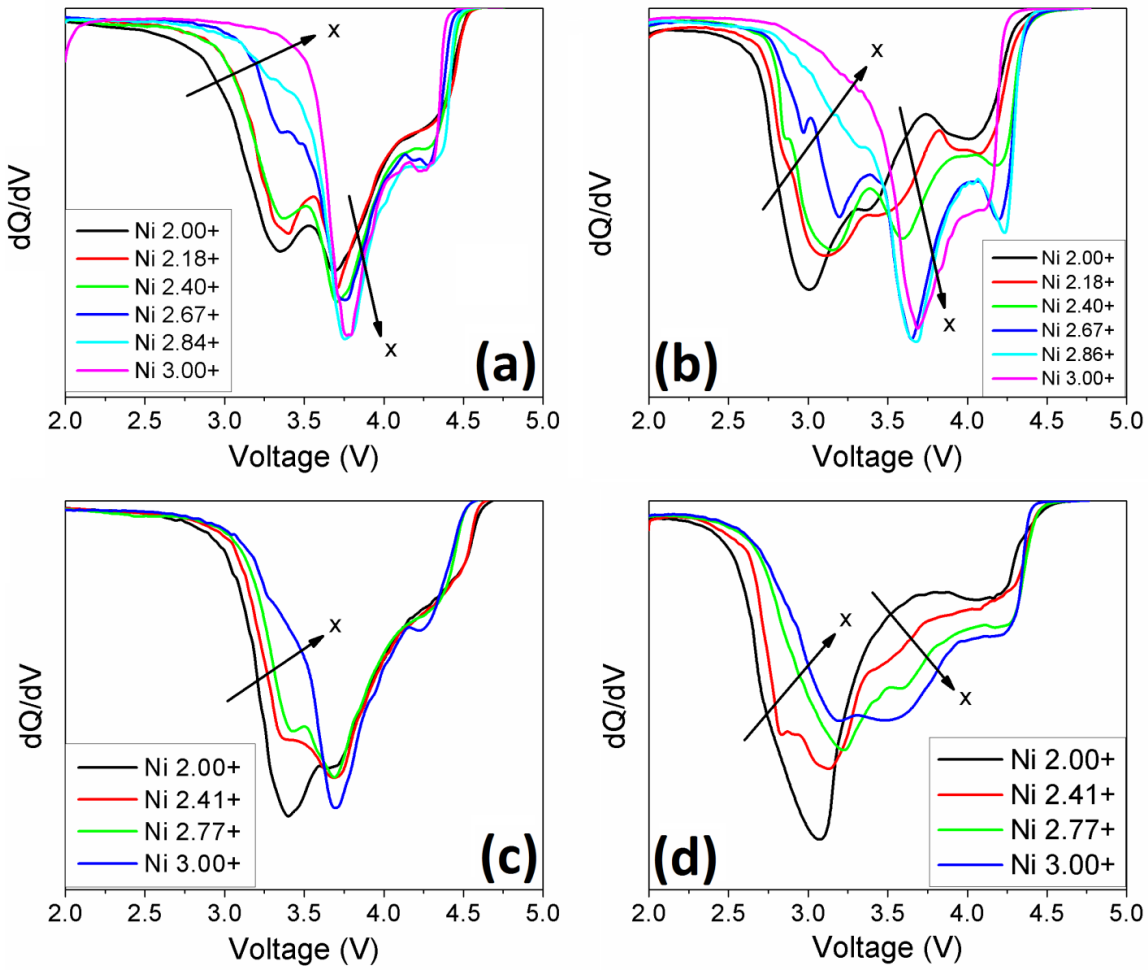

Figure 4.3. dQ/dV plots of (a) the undoped series 1st cycle, (b) the undoped series 50th cycle, (c) the Co series 1st cycle, and (d) the Co series 50th cycle.

Looking at the 50th discharge cycle dQ/dV plots, these trends are maintained and have even been enhanced over extended cycling. The Ni/Co reduction increases and the Mn reduction decreases with increasing Ni oxidation state. The amount of Mn reduction has increased dramatically, however, for each sample, which demonstrates how voltage decay occurs gradually but continuously during extended cycling. The undoped Ni^{3+}

sample still shows the smallest amount of Mn reduction. All of the Co series samples exhibit a large amount of Mn reduction, confirming that the addition of Co and its corresponding increase in capacity and oxygen loss leads to greater amounts of voltage decay.

As voltage decay is one of the largest issues with LLO, the effect of Ni oxidation state on it is very important. As mentioned previously, voltage decay is the gradual transformation of the layered phase to a spinel-like phase that leads to a decreased operating voltage. It is exacerbated by several factors, including TM migration and Mn reduction, so impeding these processes can slow down the phase transformation as well. Figures 4.4a and 4.4b, respectively, display the 2^{nd} and 50^{th} charge-discharge profiles of the undoped series. Figures 4.4c and 4.4d do the same for the Co series. It is clear that in the 2^{nd} cycle, despite different discharge capacities, the samples have nearly identical discharge voltages. This is true for both the undoped and Co series. After 50 cycles, however, there is a large difference in the discharge voltages, as the samples with lower Ni oxidation states have suffered from severe voltage decay. Again, the degree of voltage decay reduction in the Co series is less than that in the undoped series because of the presence of Co and the decrease in Ni content. The Co series experiences more voltage decay overall. The reduction in voltage decay is induced by the decrease in Mn^{4+} reduction to Mn^{3+}. This decrease is caused by the combination of the increase in Ni content, shortened oxygen loss plateau, and the fact that Ni^{4+} ions are reduced to Ni^{2+} before Mn^{4+} ions are reduced to Mn^{3+}. A decrease in the Mn^{4+} reduction will result in the formation of less Mn^{3+}, resulting in less layered-to-spinel transformation since Mn^{3+} ions

readily dissociate into Mn^{4+} and Mn^{2+} ions, which migrates easily to the Li layer through the neighboring tetrahedral sites.[23]

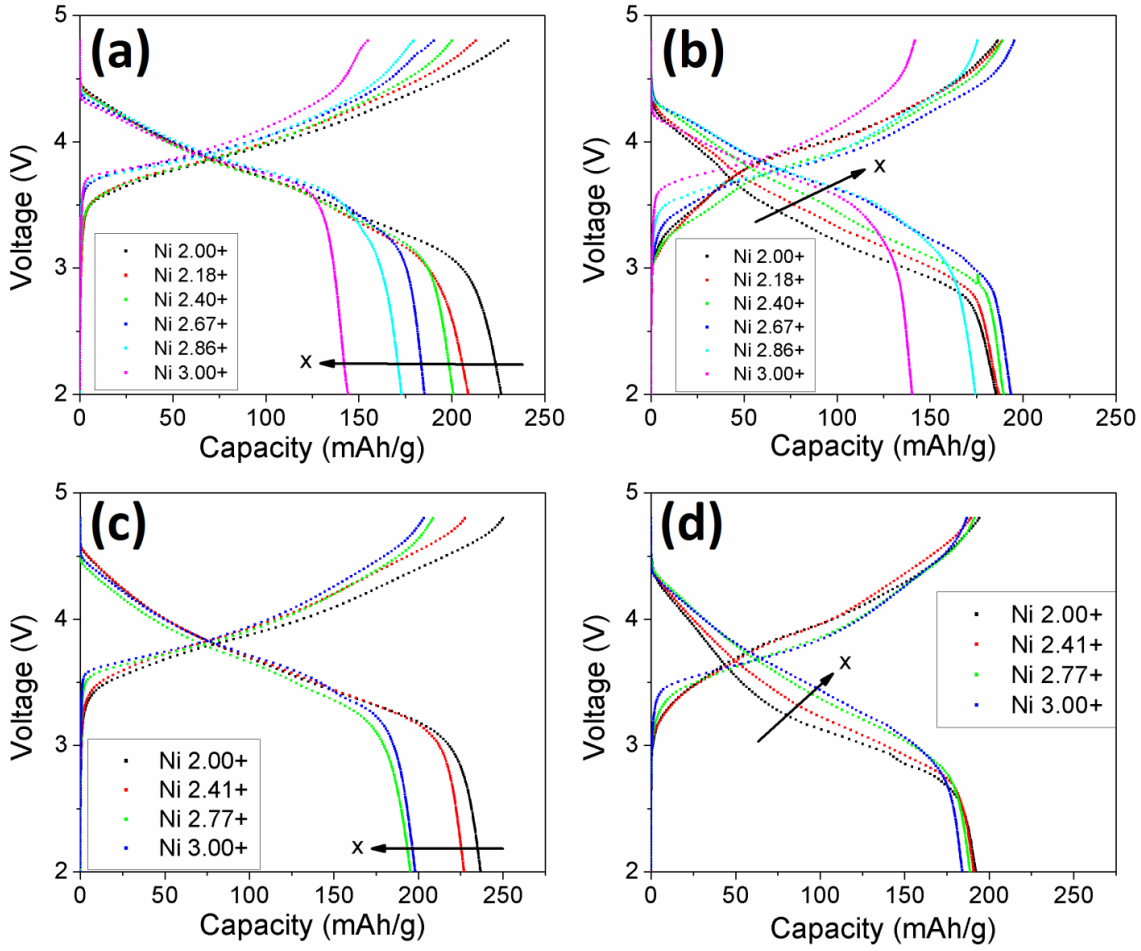

Figure 4.4. Charge-discharge profiles of (a) the undoped series 2nd cycle, (b) the undoped series 50th cycle, (c) the Co series 2nd cycle, and (d) the Co series 50th cycle to show the voltage decay over extended cycling.

While it is useful to compare the charge-discharge profiles of materials to study voltage decay, there are issues with that method. The large differences in discharge

capacities of these samples can make the voltage decay reduction look more exaggerated. An easy way to overcome this is to normalize the discharge capacities of each sample and then compare the resulting charge-discharge profiles. This has been done in Figure 4.5. Figures 4.5a and 4.5b, respectively, display the 2^{nd} and 50^{th} normalized charge-discharge profiles of the undoped series. Figures 4.5c and 4.5d do the same for the Co series. Looking at the 2^{nd} charge-discharge cycle plots, one can see that now there is a variation in the discharge voltage of the various samples in both series. The samples with higher Ni oxidation states have higher discharge voltages because they derive less of their capacity from the lower voltage Mn reduction process. The 50^{th} charge-discharge cycle plots show the voltage decay progression after extended cycling. Even after normalizing the capacities, it is clear that increasing the Ni oxidation state reduces the amount of voltage decay experienced in LLOs. The apparent reduction is minimized, however, by the normalization process. The decrease in voltage decay is also illustrated for several samples in Figure 4.6. Here the normalized voltage decay over extended cycling is shown in Figures 4.6a and 4.6b, respectively, for the undoped samples with all Ni^{2+} ions and all Ni^{3+} ions. The same plots are shown for the Co series in Figures 4.6c and 4.6d. Again, it is clear to see that the increase in Ni oxidation state leads to a smaller amount of voltage decay during cycling.

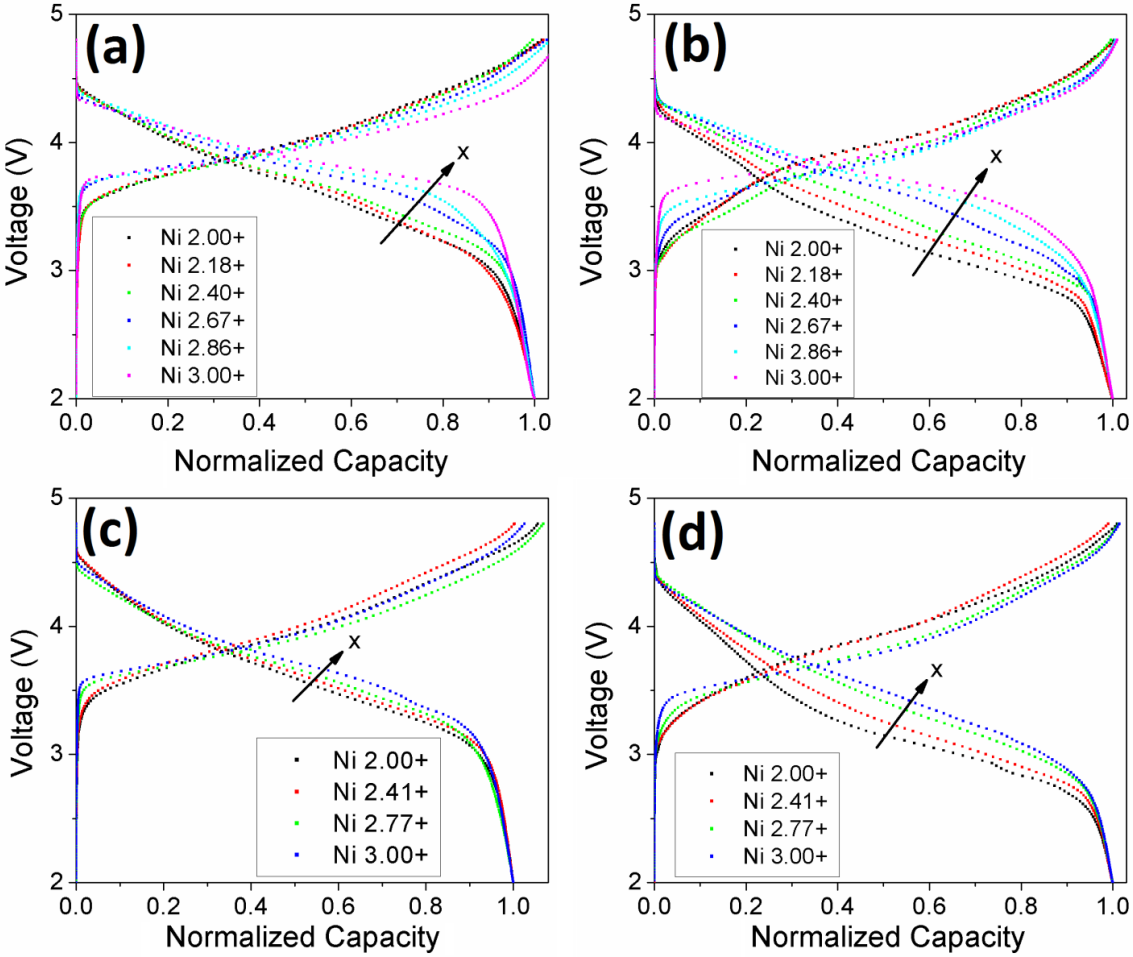

Figure 4.5. Normalized charge-discharge profiles of (a) the undoped series 2nd cycle, (b) the undoped series 50th cycle, (c) the Co series 2nd cycle, and (d) the Co series 50th cycle to show the normalized voltage decay over extended cycling.

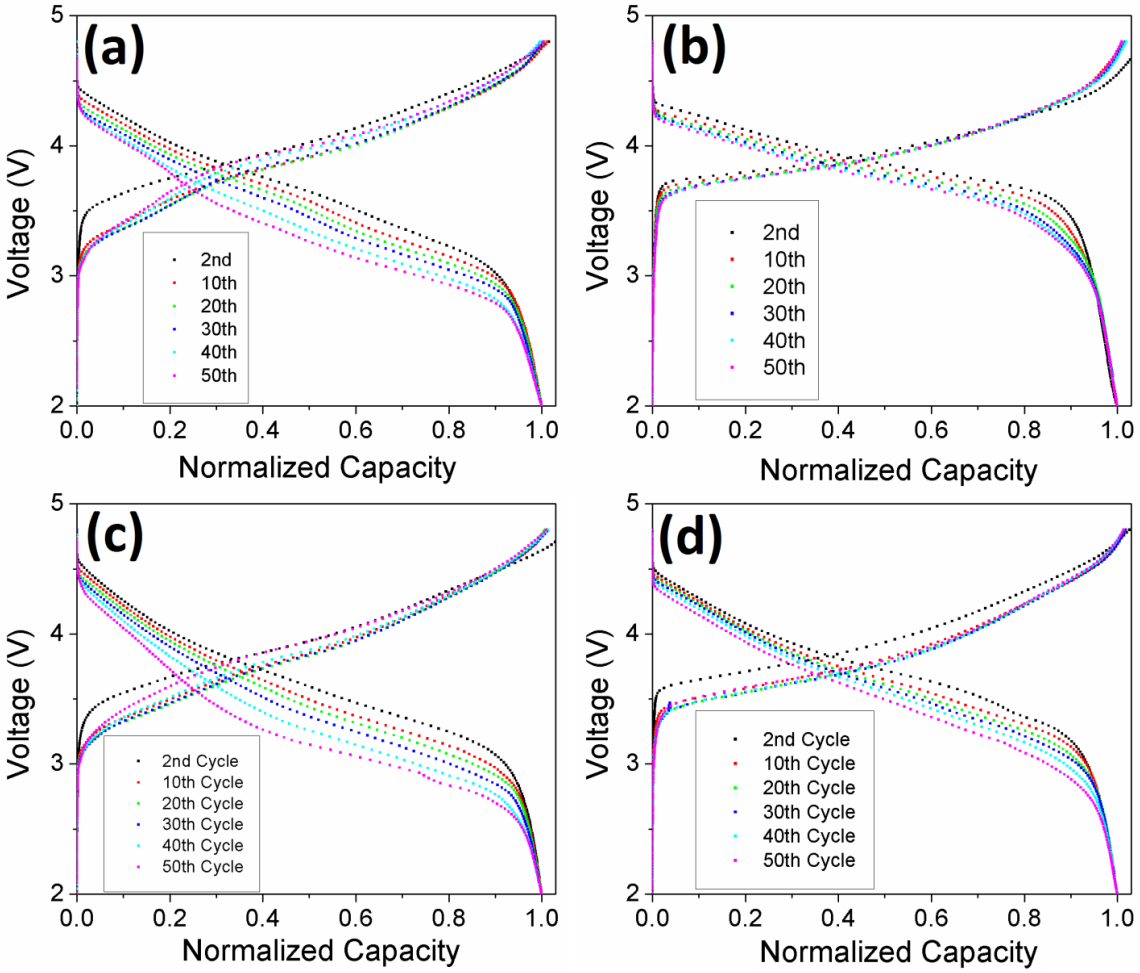

Figure 4.6. Charge-discharge profiles of various cycles for (a) undoped series $x = 0.00$, (b) undoped series $x = 0.20$, (c) Co series $x = 0.00$, and (d) Co series $x = 0.14$ samples.

4.4. CONCLUSIONS

The effect of Ni oxidation state on the properties of LLOs has been investigated systematically with two series of materials, $Li_{1.2}Mn_{0.6-x}Ni_{0.2+x}O_2$ (x = 0, 0.02, 0.05, 0.1, 0.15, and 0.2) and $Li_{1.2}Mn_{0.54-x}Ni_{0.13+x}Co_{0.13}O_2$ (x = 0, 0.04, 0.09, and 0.14), by varying the Ni oxidation state from 2+ to 3+ in each series. Increasing the Ni oxidation state has

several effects on LLOs. The addition of smaller Ni^{3+} ions decreases the amount of Li/Ni site mixing, which enhances Li-ion diffusion and impedes the layered-to-spinel transformation and the voltage decay process. The increase in Li-ion diffusion manifests as a slightly increased sloping region during charging. The oxygen loss plateau decreases with increasing Ni oxidation state due to the reduction in the Li_2MnO_3 character of the material from the decreased Mn content and the reduction of Li ions in the TM layer. This helps to delay the layered-to-spinel phase transformation because less oxygen vacancies are created, meaning there is less TM reduction and migration at the end of the 1^{st} charge cycle. The first cycle IRC increases dramatically due to the tendency of layered oxides with Ni^{3+} ions to form an inactive domain during the 1^{st} charge cycle. The shortened oxygen loss plateau and increased IRC lead to significantly decreased discharge capacity with increasing Ni oxidation state. The higher Ni oxidation state reduces the amount of Mn^{3+} ion formation during discharge due to the lower discharge capacity values, and the consequent decrease in the amount of TM reduction overall. The reduction in Mn^{3+} formation means less Mn^{3+} disproportionation into Mn^{4+} and Mn^{2+} ions, which reduces Mn dissolution into the electrolyte and impedes the layered-to-spinel phase transformation. In closing, increasing the Ni oxidation state is potentially a useful method for improving the cyclability and reducing the voltage decay in LLOs, but it comes at the expense of lowering the discharge capacity. If the discharge capacity can be increased through other mechanisms, such as surface coating or doping, then increasing the Ni oxidation state could benefit the performance.

Chapter 5: Delithiation Mechanisms in Acid of Spinel $LiMn_{2-x}M_xO_4$ (M = Cr, Fe, Co, and Ni) Cathodes*

5.1 INTRODUCTION

Lithium-ion batteries have become an integral part of modern society as they power most of the consumer electronic devices due to their high energy density; they are also being intensively pursued for electric vehicles (EV) and plug-in hybrid electric vehicles (PHEV).[185] Lithium-insertion compounds based on layered, spinel, and olivine structures, *e.g.*, $LiCoO_2$, $LiMn_2O_4$, $LiFePO_4$, as well as their solid solutions with other metal ions, have become the dominant cathode materials for lithium-ion batteries.[176] One of the major issues with lithium-ion batteries is the dissolution of transition-metal ions from the cathode into the electrolyte, especially at higher operating voltages and under conditions of over charge.[186-189] The dissolved metal ions migrate into the graphite anode, get reduced, plate on the anode, and lead to performance degradation during cycling.[190] The amount of metal ions dissolved from the cathode is generally determined by analyzing the transition-metal ion content on the cycled anode or by soaking the cathode powder in electrolyte for a certain amount of time and analyzing the transition-metal-ion content in the electrolyte. It is widely accepted that manganese ions dissolve more than other ions like cobalt or nickel and, therefore, the manganese ions play a larger role in poisoning the graphite anode.

---

* Portions of this chapter have previously been published as J. C. Knight, S. Therese, and A. Manthiram, "Delithiation Mechanisms in Acid of Spinel $LiMn_{2-x}M_xO_4$ (M = Cr, Fe, Co, and Ni) Cathodes", *Journal of The Electrochemical Society*, 2015, **162**, A426-A431.
J. C. Knight carried out the experimental work with assistance from S. Therese. A. Manthiram supervised the research. All participated in preparing the manuscript.

The manganese dissolution in lithium-ion cells is believed to occur due to a disproportionation of Mn^{3+} into Mn^{4+} and Mn^{2+} in the presence of trace amounts of protons originating from ppm levels of H_2O, which generates HF by reacting with the $LiPF_6$ salt in the electrolyte. This is supported by an elegant experiment carried out by Hunter in 1981.[2] He showed that stirring the spinel $LiMn_2O_4$ powder with dilute sulfuric acid resulted in an extraction of lithium from $LiMn_2O_4$ due to the disproportionation of Mn^{3+} into Mn^{4+} and Mn^{2+} ions to give MnO_2 as shown in Reaction 5.1:

$$LiMn^{3+}Mn^{4+}O_4 \rightarrow 0.75\ Mn_2O_4 + 0.5\ Li_2O + 0.5\ MnO \qquad (5.1)$$

While both Li_2O and MnO go into solution as Li_2SO_4 and $MnSO_4$ by reaction with sulfuric acid, Mn_2O_4 (or MnO_2) remains in the solid with the maintenance of the spinel framework structure in which the 8a tetrahedral sites are completely empty. This spinel form of MnO_2 is designated commonly as λ-MnO_2. The lithium extraction process in acid medium from spinel $LiMn_2O_4$ following Reaction 5.1 is pictorially depicted in Figure 5.1.

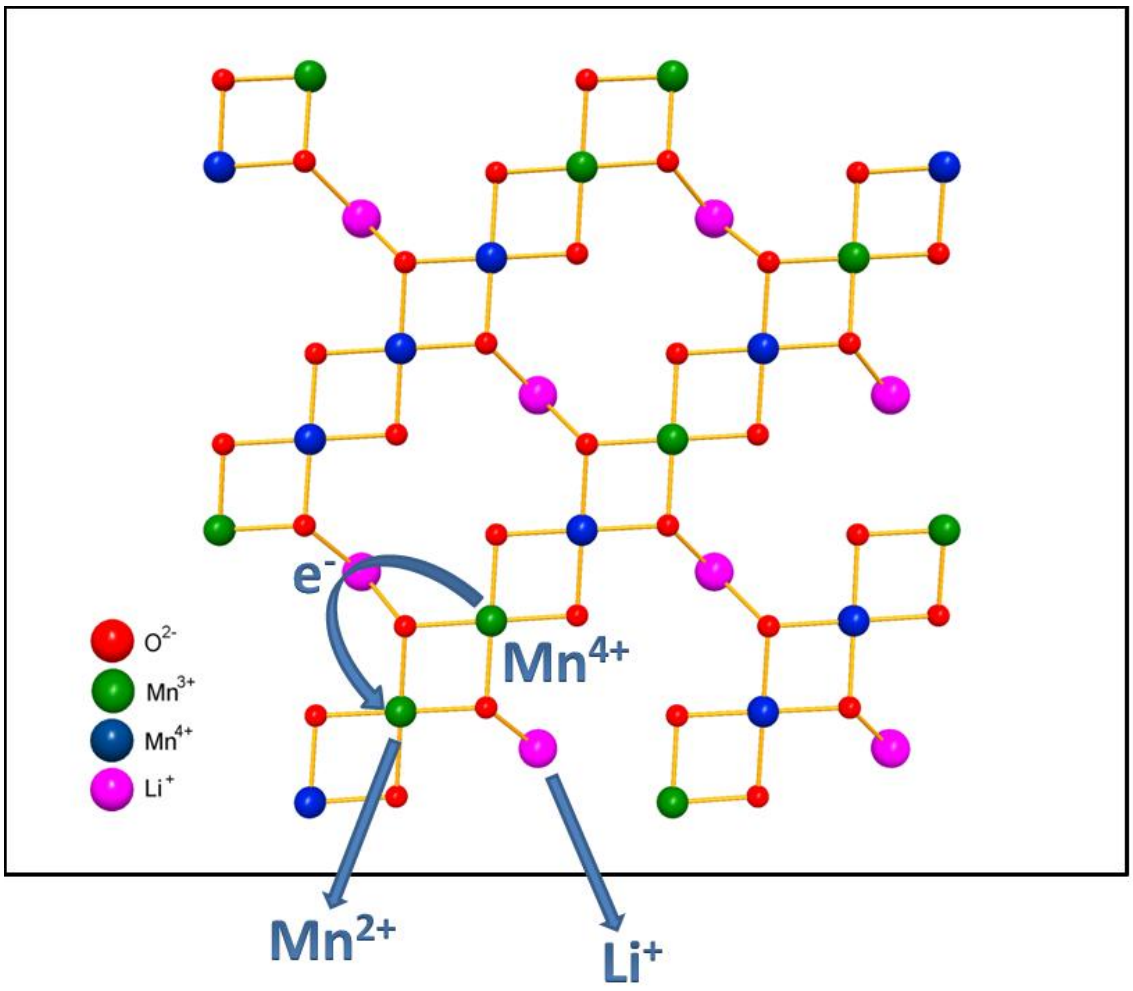

Figure 5.1. Atomic model depicting the mechanism of lithium extraction from spinel $LiMn_2O_4$ with acid as proposed by Hunter.[2]

Following the early work by Hunter, several studies have focused on the extraction of lithium from $LiMO_2$ (M = Mn, Co, and Ni) layered oxides.[191-194] However, the delithiation of layered oxides with dilute sulfuric acid is often complicated by an exchange of Li^+ ions in the lattice by H^+ ions. Protons are inserted into the layered oxides even when lithium extraction is carried out in a nonaqueous medium such as acetonitrile

with oxidizing agents like NO_2BF_4[195, 196] and chlorine.[194] In fact, the ability of layered oxides to readily accommodate protons into the lithium layer seems to adventitiously improve the cyclability of spinel $LiMn_2O_4$ when they are employed together in a cathode because the layered oxide can trap the trace amount of protons present in the electrolyte and suppress manganese dissolution from the spinel phase.[197] For example, composite cathodes consisting of spinel $LiMn_2O_4$ and layered $Li[Mn,Ni,Co]O_2$ (~ 2:1 ratio) are used effectively in the Chevy Volt and Nissan Leaf to overcome the common challenge with spinel $LiMn_2O_4$ cathodes. Interestingly, the extraction of lithium from spinel $LiMn_2O_4$ with the oxidizing agent NO_2BF_4 does not seem to be accompanied by an exchange of Li^+ ions with protons since the oxidation state of Mn (determined by a redox titration) increases proportionately with the degree of lithium extraction from $LiMn_2O_4$.[198] However, there have been some reports on the exchange of Li^+ ions by protons in spinel oxides[199-201], but further clarification is necessary. It seems that such an exchange occurs only when the lithium content is > 1.0 or with spinel oxides prepared at low temperatures that have cation defects.

The layered and spinel oxide cathodes are based mostly on Mn, Co, and Ni; however, the substitutions of small amounts of Cr and Fe have shown improvement in performance, particularly with the high voltage spinel $LiMn_{1.5}Mn_{0.5}O_4$.[163, 202-206] In order to develop a better understanding of the mechanisms that lead to capacity fade, a comprehensive understanding of which ions among Cr, Mn, Fe, Co, and Ni tend to disproportionate and which ions do not in the presence of acid needs to be developed. Since the delithiation reactions of layered oxides with acid are complicated by the

exchange of Li^+ ions by H^+ ions, it is difficult to establish the disproportionation reaction phenomenon in layered oxides. Spinel oxides synthesized at high temperatures with a lithium content of 1.0 are the best materials to establish this phenomenon as they do not seem to incorporate protons[198], but spinel oxides like $LiCo_2O_4$ and $LiNi_2O_4$ that would contain Co^{3+} and Ni^{3+} ions are not known as pure well-developed spinel samples. Accordingly, we present here a systematic investigation of the delithiation with acid of four series of spinel oxides, $LiMn_{2-x}Ni_xO_4$ ($0 \leq x \leq 0.5$) and $LiMn_{2-x}M_xO_4$ ($0 \leq x \leq 1.0$) (M = Cr, Fe, and Co). The products formed before and after delithiation with acid are characterized by XRD, lithium content analysis, and oxygen content analysis to establish (i) the delithiation mechanism, (ii) whether or not Cr^{3+}, Fe^{3+}, Co^{3+}, and Ni^{2+} ions also disproportionate similar to Mn^{3+}, and (iii) whether or not protons are inserted into the spinel lattice due to an exchange of Li^+ ions by H^+ ions.

5.2 EXPERIMENTAL

5.2.1 Synthesis

The spinel $LiMn_{2-x}M_xO_4$ (M = Cr, Fe, Co, and Ni) samples were synthesized by a solution-based method employing ethylenediaminetetraacetic acid (EDTA) and citric acid as chelating agents, analogous to that reported previously for layered oxides.[39] Required amounts of lithium, manganese, nickel, iron, and cobalt acetate and chromium nitrate were dissolved in water, while a separate aqueous solution consisting of EDTA, citric acid, and ammonium hydroxide was also prepared. The metal acetate solution was then added dropwise into the EDTA/citric acid/NH_4OH solution, while maintaining a metal

ions : EDTA : citric acid molar ratio of 1 : 1 : 1.5. The transparent solution formed was stirred for 12 h at ~ 120 °C to obtain a viscous gel, which was then heated at ~ 450 °C for ~ 6 h until the organics mostly decomposed. The resulting powder was then calcined at 800 °C for 24 h. The $LiMn_{1.5}Ni_{0.5}O_4$ sample was annealed at 700 °C for 48 h to eliminate most of the rocksalt impurity, which also increased the degree of cation ordering between Mn^{4+} and Ni^{2+} ions. The delithiation procedure consisted of suspending 250 mg of the spinel oxide in 25 mL of 0. 35 N H_2SO_4 and stirring it for 24 h at room temperature, followed by filtering with a sintered glass filter, washing thoroughly with de-ionized water to remove the acid and other soluble products completely, and drying in an air oven at 100 °C overnight. It should be noted that much higher solution acidity than would be experienced inside an actual lithium-ion cell is used here in order to speed up the delithiation process to occur at a reasonable time scale and assess the products and understand the mechanism.

5.2.2. Characterization

The samples were characterized by XRD with a Rigaku Ultima IV diffractometer with Cu K-α radiation in the 2θ range of 10 – 80° with a 0.03° step size. Lattice parameters were calculated using the Reitveld refinement program in Rigaku's PDXL software. Lithium and transition-metal contents in the sample were determined with a Varian 715-ES inductively coupled plasma – optical emission spectroscopy (ICP-OES) analyzer. The compositions of the initial samples were found to be close to the nominal compositions, with a Li content of 1.00 ± 0.03. The oxygen content in the samples was

determined by the iodimetric redox titration.[207] A known amount of the sample was dissolved in a mixture of potassium iodide and a 3.5 N HCl solution. The liberated iodine was titrated against a 0.03 N sodium thiosulfate solution using a starch solution as an indicator. Based on the amount of sodium thiosulfate consumed, the oxygen content in the sample was calculated employing the charge neutrality principle.

5.3. RESULTS AND DISCUSSION

As pointed out in the introduction (Section 5.1), the delithiation of spinel oxides with acid has been proposed to occur by a disproportionation of Mn^{3+} ions into Mn^{2+} and Mn^{4+} ions that is accompanied by the loss of soluble Li_2O and MnO into the solution while Mn^{4+} remains in the solid (Reaction 5.1).[2] Using this mechanism and assuming only Mn^{3+} undergoes disproportionation, the expected (calculated) compositions after delithiation with acid are given in Table 5.1 for the $LiMn_{2-x}Ni_xO_4$ ($0 \leq x \leq 0.5$) and $LiMn_{2-x}M_xO_4$ ($0 \leq x \leq 1.0$) (M = Cr, Fe, and Co) series. The oxidation states of the ions in the initial samples are indicated in column 2, the species dissolving into the solution are given in column 3, and the calculated compositions of the solid remaining after delithiation are given in column 4 of Table 5.1. The compositions in column 4 are then normalized to obtain an oxygen content of 4 to be consistent with the spinel formula and are given in column 5. As the transition-metal dopant content in the initial samples increases, the amount of Mn^{3+} content decreases (column 2 in Table 5.1).

Table 5.1. Initial compositions and calculated compositions after acid delithiation based on the disproportionation of Mn^{3+} as shown in Reaction 5.1

Initial composition[a]	Oxidation state of metal ions in the initial composition	Calculated amounts of species dissolved into the solution	Calculated solid composition after delithiation	Calculated normalized solid composition after delithiation
$LiMn_2O_4$	$LiMn^{3+}Mn^{4+}O_4$	$0.5Li_2O + 0.5MnO$	$Mn_{1.5}^{4+}O_{3.0}$	Mn_2O_4
$LiMn_{1.75}Ni_{0.25}O_4$	$LiMn_{0.5}^{3+}Mn_{1.25}^{4+}Ni_{0.25}^{2+}O_4$	$0.25Li_2O + 0.25MnO$	$Li_{0.5}Mn_{1.5}^{4+}Ni_{0.25}^{2+}O_{3.5}$	$Li_{0.57}Mn_{1.71}Ni_{0.29}O_4$
$LiMn_{1.5}Ni_{0.5}O_4$	$LiMn_{1.5}^{4+}Ni_{0.5}^{2+}O_4^{2-}$	No disproportionation	$LiMn_{1.5}^{4+}Ni_{0.5}^{2+}O_4$	$LiMn_{1.5}Ni_{0.5}O_4$
$LiMn_{1.75}M_{0.25}O_4$	$LiMn_{0.75}^{3+}Mn^{4+}M_{0.25}^{3+}O_4$	$0.375Li_2O + 0.375MnO$	$Li_{0.25}Mn_{1.375}^{4+}M_{0.25}^{3+}O_{3.25}$	$Li_{0.31}Mn_{1.69}M_{0.31}O_4$
$LiMn_{1.5}M_{0.5}O_4$	$LiMn_{0.5}^{3+}Mn^{4+}M_{0.5}^{3+}O_4$	$0.25Li_2O + 0.25MnO$	$Li_{0.5}Mn_{1.25}^{4+}M_{0.5}^{3+}O_{3.5}$	$Li_{0.57}Mn_{1.43}M_{0.57}O_4$
$LiMn_{1.25}M_{0.75}O_4$	$LiMn_{0.25}^{3+}Mn^{4+}M_{0.75}^{3+}O_4$	$0.125Li_2O + 0.125MnO$	$Li_{0.75}Mn_{1.125}^{4+}M_{0.75}^{3+}O_{3.75}$	$Li_{0.8}Mn_{1.2}M_{0.8}O_4$
$LiMnMO_4$	$LiMn^{4+}M^{3+}O_4$	No disproportionation	$LiMn^{4+}M^{3+}O_4$	$LiMnMO_4$

[a] (M = Cr, Fe, or Co)

Figures 5.2 through 5.5 compare the XRD patterns of the $LiMn_{2-x}Ni_xO_4$ ($0 \leq x \leq 0.5$) samples, the $LiMn_{2-x}Co_xO_4$ ($0 \leq x \leq 1.0$) samples, the $LiMn_{2-x}Cr_xO_4$ ($0 \leq x \leq 1.0$) samples, and the $LiMn_{2-x}Fe_xO_4$ ($0 \leq x \leq 1.0$) samples, respectively, before and after delithiation. Their lattice parameters can be seen in Table 5.2. All of the reflections in the samples before and after delithiation could be indexed based on the $Fd\bar{3}m$ cubic spinel structure, indicating the absence of impurity phases, except for a few samples. A trace amount of $Ni_{1-x}Li_xO$ impurity can be found in the $x = 0.5$ sample in the Ni series. In the case of $LiMnCoO_4$, a small amount of a Co-rich layered oxide phase is present. In the Fe series, when $x \geq 0.75$, there are several additional peaks on the lower 2θ side of the existing peaks, which are most likely from an Fe-rich spinel impurity.[208, 209] The initial $LiMn_{2-x}Co_xO_4$ samples in the Co series exhibit increased peak broadening with increasing Co content. The Co and Mn ions do not order in the spinel structure, so increasing the Co content increases the structural disorder and leads to peak broadening. However, the trend reverses upon going from the x = 0.75 sample to the x = 1.0 sample, as the 1:1 ratio of Mn:Co may provide a better structural order and crystallinity due to the lack of Mn^{3+} ions. This behavior was also seen by Amarillo *et al.*[210] Although another study has reported Cr ions in the 8a tetrahedral sites depending on the composition and synthesis method,[211] this was not found to be the case in our study as the (111) peaks at ~19° did not show a decrease in intensity and the (220) peaks at ~ 31° did not exhibit an increase in intensity as would occur if an appreciable amount of Cr were in the tetrahedral sites.[209, 212]

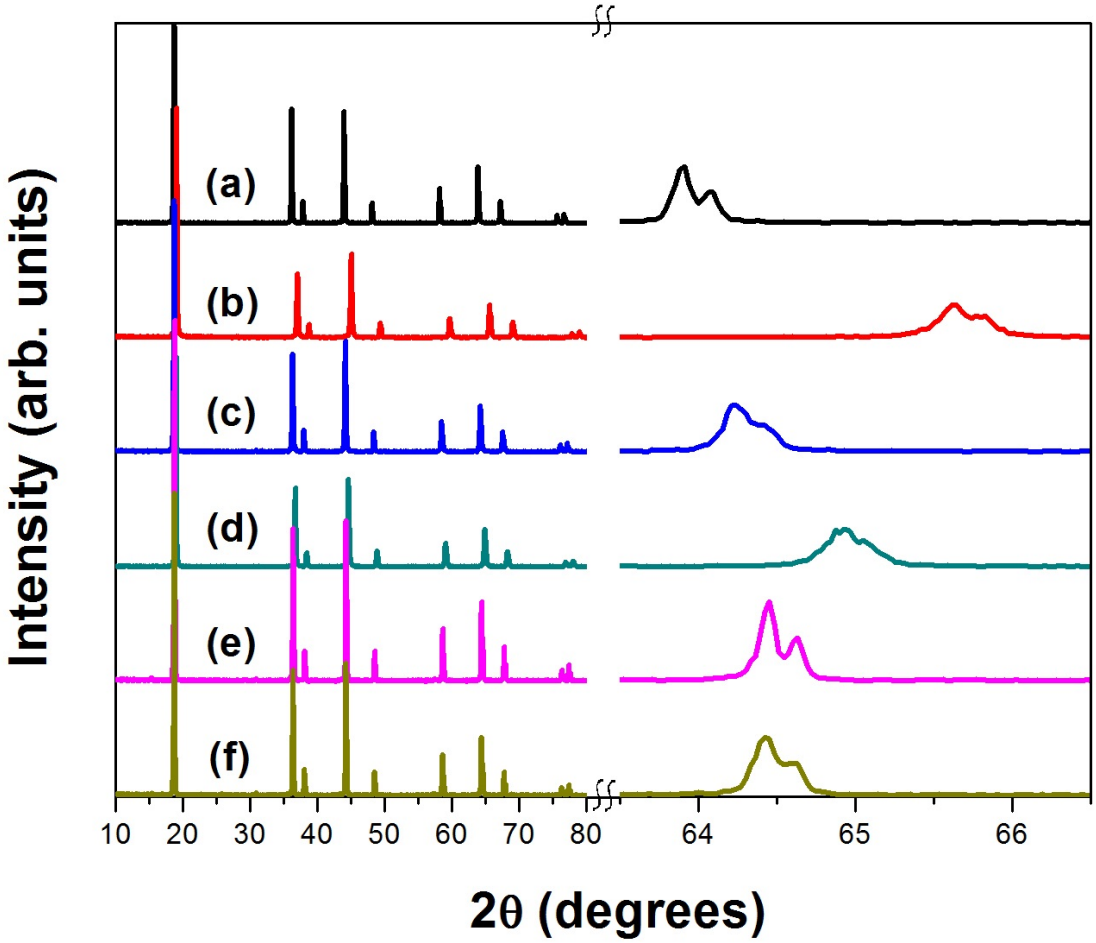

Figure 5.2. XRD patterns of $LiMn_{2-x}Ni_xO_4$ series before and after delithiation with acid. The expanded region over a small 2θ range on the right reveals the shifts in the peaks to higher angles upon delithiation. (a) $x = 0$ before delithiation, (b) $x = 0$ after delithiation, (c) $x = 0.25$ before delithiation, (d) $x = 0.25$ after delithiation, (e) $x = 0.5$ before delithiation, and (f): $x = 0.5$ after delithiation.

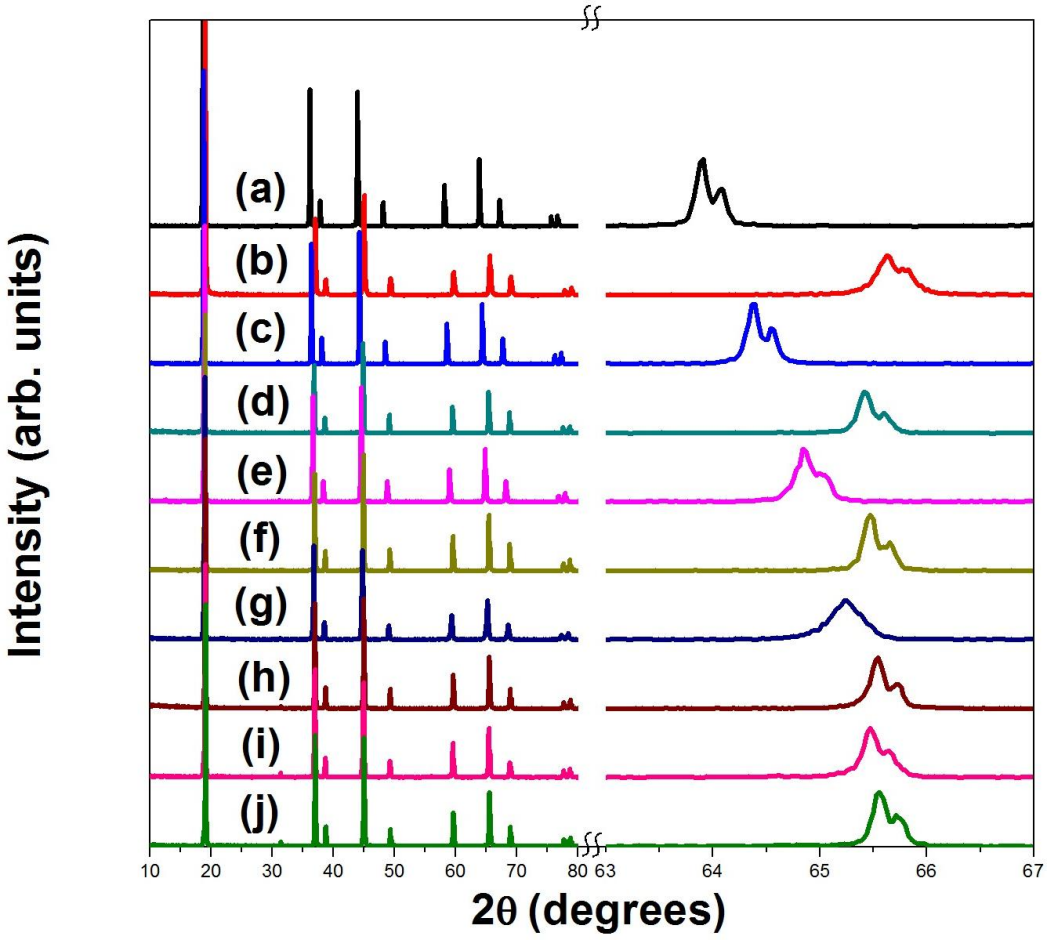

Figure 5.3. XRD patterns of $LiMn_{2-x}Co_xO_4$ series before and after delithiation with acid. The expanded region over a small 2θ range on the right reveals the shifts in the peaks to higher angles upon delithiation. (a) $x = 0$ before delithiation, (b) $x = 0$ after delithiation, (c) $x = 0.25$ before delithiation, (d) $x = 0.25$ after delithiation, (e) $x = 0.5$ before delithiation, (f) $x = 0.5$ after delithiation, (g) $x = 0.75$ before delithiation, (h) $x = 0.75$ after delithiation, (i) $x = 1$ before delithiation, and (j) $x = 1$ after delithiation.

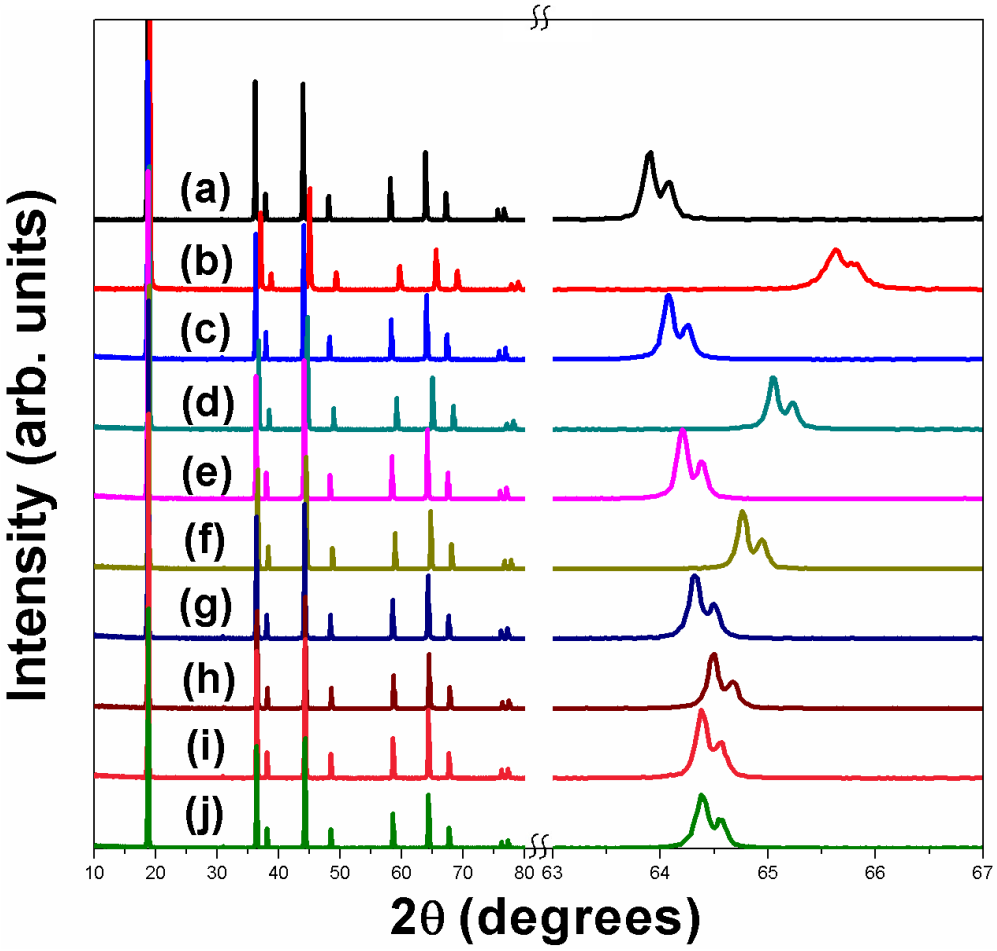

Figure 5.4. XRD patterns of $LiMn_{2-x}Cr_xO_4$ series before and after delithiation with acid. The expanded region over a small 2θ range on the right reveals the shifts in the peaks to higher angles upon delithiation. (a) $x = 0$ before delithiation, (b) $x = 0$ after delithiation, (c) $x = 0.25$ before delithiation, (d) $x = 0.25$ after delithiation, (e) $x = 0.5$ before delithiation, (f) $x = 0.5$ after delithiation, (g) $x = 0.75$ before delithiation, (h) $x = 0.75$ after delithiation, (i) $x = 1$ before delithiation, and (j) $x = 1$ after delithiation.

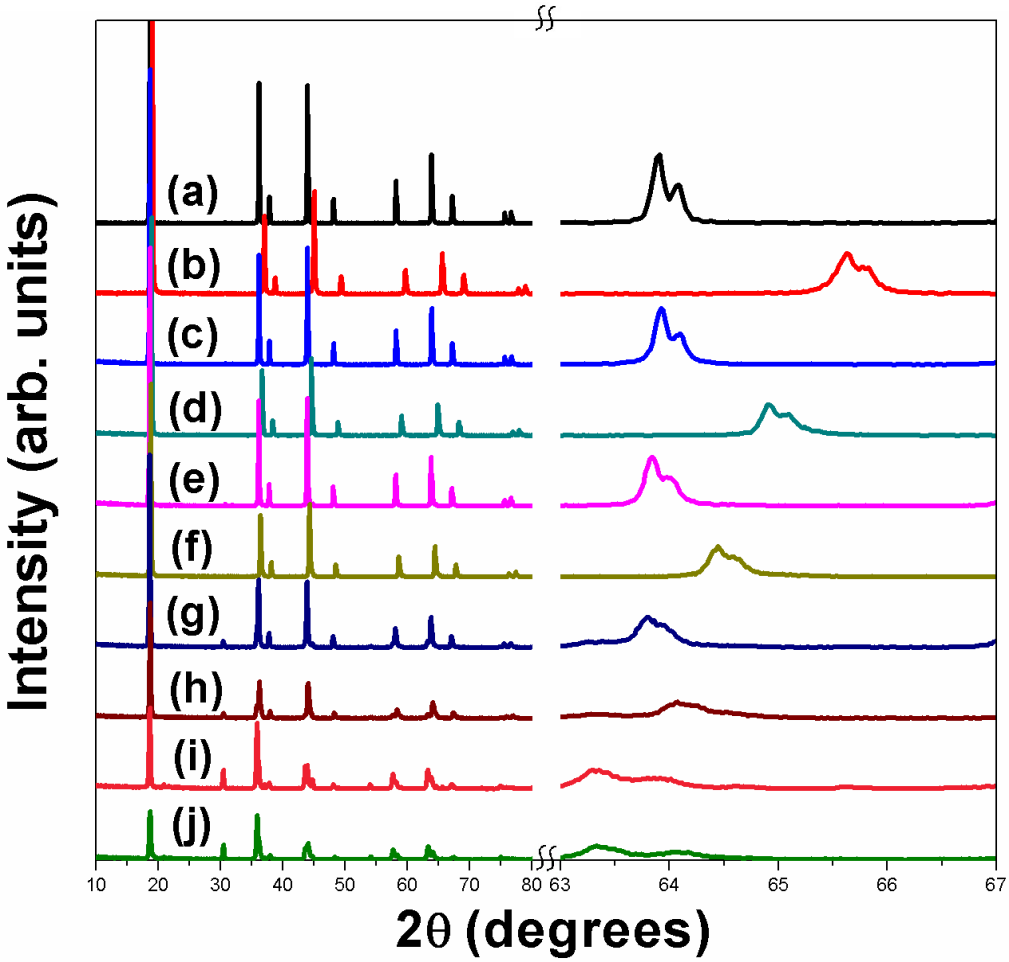

Figure 5.5. XRD patterns of $LiMn_{2-x}Fe_xO_4$ series before and after delithiation with acid. The expanded region over a small 2θ range on the right reveals the shifts in the peaks to higher angles upon delithiation. (a) $x = 0$ before delithiation, (b) $x = 0$ after delithiation, (c) $x = 0.25$ before delithiation, (d) $x = 0.25$ after delithiation, (e) $x = 0.5$ before delithiation, (f) $x = 0.5$ after delithiation, (g) $x = 0.75$ before delithiation, (h) $x = 0.75$ after delithiation, (i) $x = 1$ before delithiation, and (j) $x = 1$ after delithiation.

Table 5.2. Compositions, lattice parameters, and oxygen content values before and after delithiation with acid

Initial samples			Samples obtained after delithiation				
Composition	Lattice parameter (Å)	Oxygen content[a]	Calculated composition[b]	Experimentally observed composition	Lattice parameter (Å)	Change in lattice parameter (Å)	Oxygen content[a]
$LiMn_2O_4$	8.24140(6)	4.01	Mn_2O_4	$Li_{0.07}Mn_{2.00}O_4$	8.03665(5)	-0.20475	3.98
$LiMn_{1.75}Ni_{0.25}O_4$	8.19559(3)	3.98	$Li_{0.57}Mn_{1.71}Ni_{0.29}O_4$	$Li_{0.56}Mn_{1.71}Ni_{0.24}O_4$	8.12134(3)	-0.07425	3.98
$LiMn_{1.5}Ni_{0.5}O_4$	8.17194(2)	------	$LiMn_{1.5}Ni_{0.5}O_4$	$Li_{1.01}Mn_{1.5}Ni_{0.50}O_4$	8.17122(2)	-0.00072	-----
$LiMn_{1.75}Co_{0.25}O_4$	8.18126(3)	4.02	$Li_{0.31}Mn_{1.69}Co_{0.31}O_4$	$Li_{0.31}Mn_{1.69}Co_{0.26}O_4$	8.06331(2)	-0.11795	4.01
$LiMn_{1.5}Co_{0.5}O_4$	8.12514(2)	3.99	$Li_{0.57}Mn_{1.43}Co_{0.57}O_4$	$Li_{0.58}Mn_{1.43}Co_{0.52}O_4$	8.05857(4)	-0.06657	4.02
$LiMn_{1.25}Co_{0.75}O_4$	8.08457(4)	3.98	$Li_{0.8}Mn_{1.2}Co_{0.8}O_4$	$Li_{0.75}Mn_{1.2}Co_{0.76}O_4$	8.05642(6)	-0.02815	3.97
$LiMnCoO_4$	8.05679(3)	-----	$LiMnCoO_4$	$Li_{0.91}MnCo_{1.00}O_4$	8.04968(8)	-0.00711	-----
$LiMn_{1.75}Cr_{0.25}O_4$	8.22183(3)	3.97	$Li_{0.31}Mn_{1.69}Cr_{0.31}O_4$	$Li_{0.28}Mn_{1.69}Cr_{0.26}O_4$	8.10656(5)	-0.11527	4.02
$LiMn_{1.5}Cr_{0.5}O_4$	8.20536(4)	4.03	$Li_{0.57}Mn_{1.43}Cr_{0.57}O_4$	$Li_{0.54}Mn_{1.43}Cr_{0.51}O_4$	8.14018(3)	-0.06518	4.03
$LiMn_{1.25}Cr_{0.75}O_4$	8.19352(4)	-----	$Li_{0.8}Mn_{1.2}Cr_{0.8}O_4$	$Li_{0.81}Mn_{1.2}Cr_{0.77}O_4$	8.17403(4)	-0.01949	-----
$LiMnCrO_4$	8.18917(4)	-----	$LiMnCrO_4$	$Li_{1.01}MnCr_{0.99}O_4$	8.18639(4)	-0.00278	-----
$LiMn_{1.75}Fe_{0.25}O_4$	8.23916(4)	4.01	$Li_{0.31}Mn_{1.69}Fe_{0.31}O_4$	$Li_{0.30}Mn_{1.69}Fe_{0.29}O_4$	8.12548(4)	-0.11368	3.97
$LiMn_{1.5}Fe_{0.5}O_4$	8.25261(4)	4.03	$Li_{0.57}Mn_{1.43}Fe_{0.57}O_4$	$Li_{0.59}Mn_{1.43}Fe_{0.49}O_4$	8.17862(5)	-0.07399	4.02
$LiMn_{1.25}Fe_{0.75}O_4$	8.32608(4)	-----	$Li_{0.8}Mn_{1.2}Fe_{0.8}O_4$	$Li_{0.62}Mn_{1.2}Fe_{0.74}O_4$	8.21365(8)	-0.11243	-----
$LiMnFeO_4$	8.24981(3)	-----	$LiMnFeO_4$	$Li_{0.85}MnFe_{1.03}O_4$	8.30227(9)	0.05246	-----

[a] The oxygen content values for some compositions could not be determined as the samples could not be fully dissolved
[b] The calculated compositions were obtained as illustrated in Table 5.1

The peaks in the as-prepared Co and Cr samples shift to higher 2θ values as the dopant content increases due to the substitution of smaller Co^{3+} ions (0.61 Å) and Cr^{3+} ions (0.615 Å) for the larger Mn^{3+} ions (0.645 Å). The peaks in the as-prepared Ni samples also shift to higher 2θ values as the Ni content increases since the substitution of Ni for Mn creates a Ni^{2+} ion (0.69 Å) and a Mn^{4+} ion (0.53 Å) at the expense of two Mn^{3+} ions (0.645 Å), so the net effect is a decrease in lattice parameter. However, the peaks in the as-prepared Fe samples have relatively constant locations with increasing Fe content since Fe^{3+} ions (0.645 Å) and Mn^{3+} ions (0.645 Å) have identical size. Except for the materials where no delithiation occurs, the peaks in the delithiated samples all shift to higher 2θ values and the lattice parameter values given in Table 5.2 decrease due to the oxidation of the larger Mn^{3+} ions to smaller Mn^{4+} ions. As expected, the shift to higher 2θ values and the change in lattice parameters after delithiation decrease with increasing dopant content due to the decrease in Mn^{3+} content in the initial samples and amount of the disproportionation Reaction 5.1. For the highest-doped sample in each series, which contains little or no Mn^{3+}, the reflections should not shift and the lattice parameters should not change after the delithiation treatment with the acid. This is true for the Ni and Cr series. However, $LiMnCoO_4$, which may contain a small amount of Mn^{3+} due to the Co-rich layered oxide impurity, shows a very small change in lattice parameter after the acid-delithiation treatment. The difficulty in keeping all Mn as Mn^{4+} in $LiMnCoO_4$ during the high-temperature synthesis may lead to the small amount of Mn^{3+}, which would be accompanied by the presence of a trace amount of layered oxide impurity phase

or oxygen deficiency. Similarly, $LiMnFeO_4$, which also contains an impurity phase, exhibits a slight peak shift and lattice parameter change upon delithiation.

Table 5.2 gives the experimentally obtained compositions based on the Li, Cr, Mn, Fe, Co, and Ni contents determined by ICP-OES analysis for the $LiMn_{2-x}Ni_xO_4$ ($0 \leq x \leq 0.5$) and $LiMn_{2-x}M_xO_4$ ($0 \leq x \leq 1.0$) (M = Co, Cr, and Fe) series. As seen in Table 5.2, the experimentally determined lithium contents in the samples match well with the values calculated based on the disproportionation reaction of Mn^{3+} (Reaction 5.1). The experimental compositions of the transition-metal dopants in column 5 are all slightly lower than the expected values in column 4, except the samples where no delithiation occurs. To investigate this issue, the dilute sulfuric acid solvent was also tested using the ICP, and it was found that 0.03 – 0.04 moles of Cr, Fe, Co, and Ni were dissolved in addition to the expected amounts of Li and Mn. This explains the discrepancy between the actual and expected transition-metal contents found in Table 5.2. This can be understood by the fact that as Li_2O and MnO are dissolved from the solid, the transition-metal dopants left on the surface may slightly dissolve into the sulfuric acid medium during the extended reaction time. This dissolution, however, does not cause any additional delithiation.

There are a few other discrepancies in Table 5.2 as well. Although no lithium is expected to be extracted from $LiMnCoO_4$, the small amount of lithium extracted from it is due to the following. As pointed out by Andriiko *et al.*[213], $LiMnCoO_4$ lies just past a phase boundary ($LiMn_{1.1}Co_{0.9}O_4$ was the homogenous limit) and two phases are formed: one is the desired spinel phase, while the other is a Co-rich layered oxide phase. From

our XRD pattern, we can see that our $LiMnCoO_4$ sample shows a small amount of layered oxide impurity phase. Because Co is preferentially present in the layered oxide impurity phase, the spinel phase is slightly richer in Mn and deficient in Co compared to the nominal composition of $LiMnCoO_4$. This results in a small amount of Mn^{3+} in the spinel phase and a consequent extraction of a small amount of lithium from the spinel phase. A similar reason also causes the delithiated $x = 0.75$ and 1.00 samples in the Fe series to contain much less Li than expected. As mentioned above in the XRD discussion, those two samples have significant amounts of an Fe-rich spinel impurity phase: one closer to Fe_3O_4 and the other closer to $LiMn_2O_4$. The $LiMn_2O_4$-like phase would experience delithiation due to its Mn^{3+} content.

These data presented in this investigation with four series of samples clearly establish that acid delithiation of spinel oxides occurs by a disproportionation of Mn^{3+} into Mn^{4+} and Mn^{2+} that is accompanied by a leaching out of corresponding amounts of Li_2O and MnO into solution according to Reaction 5.1 proposed by Hunter.[2] The data also establish that in spinel solid solutions consisting of Li, Mn, and either Cr, Fe, Co, or Ni, the amount of lithium extracted with acid is proportional to the Mn^{3+} content in the initial sample. Thus, the amount of lithium extracted with acid could be used to reveal quantitatively the Mn^{3+} content in such complex spinel oxides.

The experimental composition data presented in Table 5.2 reveal that $M^{3+} = Cr^{3+}$, Fe^{3+}, and Co^{3+} ions in spinel oxides do not disproportionate into M^{4+} and M^{2+}. For example, if Co^{3+} ions also disproportionate similar to Mn^{3+} ions, then one would expect to obtain spinel-like λ-$MnCoO_4$, but that is not the case. The same statements can be

made for Cr^{3+} and Fe^{3+} ions as well. However, lithium extraction with acid has been reported in the literature with layered oxides such as $LiCoO_2$ and $LiNi_{1-x}Co_xO_2$.[191-194] This could be largely related to the ion exchange of Li^+ ions by H^+ ions in acid. However, such ion exchange of Li^+ ions by H^+ ions does not occur in these spinel oxides as illustrated by the compositional analysis data in Table 5.2, which shows final compositions very close to the expected values. If such an ion exchange occurred, then the calculated and observed lithium contents and compositions in Table 5.2 would not match with each other. For example, if an exchange of Li^+ ions by H^+ ions occurs in acid, then the $LiMn_{1.5}Ni_{0.5}O_4$ composition would not remain identical (Table 5.2) before and after treating with the acid. Because ICP analysis cannot provide compositional data for H and O, one could argue that protonation may be occurring with a corresponding increase in oxygen content, but the experimentally determined oxygen contents of 4.0 ± 0.03 for the initial materials and delithiated samples further confirm that no ion exchange has occurred during the acid delithiation process of these spinel oxides. It is possible that the protons could not be accommodated or stabilized in the 8a tetrahedral sites of the spinel lattice, while they may be readily accommodated or stabilized in the octahedral sites of the lithium layer in layered oxides.

Furthermore, the $Ni^{2+/3+}$ redox energy is close to that of $Mn^{3+/4+}$ energy in oxides, so one may anticipate the following equilibrium under some conditions:

$$Mn^{4+} + Ni^{2+} \leftrightarrow Mn^{3+} + Ni^{3+} \qquad (5.2)$$

The fact that no lithium could be extracted from $LiMn_{1.5}Ni_{0.5}O_4$ with acid (Table 5.2) reveals that Reaction 5.2 remains completely towards the left without the formation of

any Mn^{3+} in the initial and delithiated samples. In other words, the $Ni^{2+/3+}$ and $Mn^{3+/4+}$ bands do not overlap in these spinel oxides as depicted in Figure 5.6, which is consistent with the neutron scattering and computational calculation data found in the literature [5, 214, 215]. The compositional analysis data in Table 5.2 are also consistent with a lying of the $Mn^{3+/4+}$ energy well above that of the $Co^{3+/4+}$ energy as depicted in Figure 5.6.

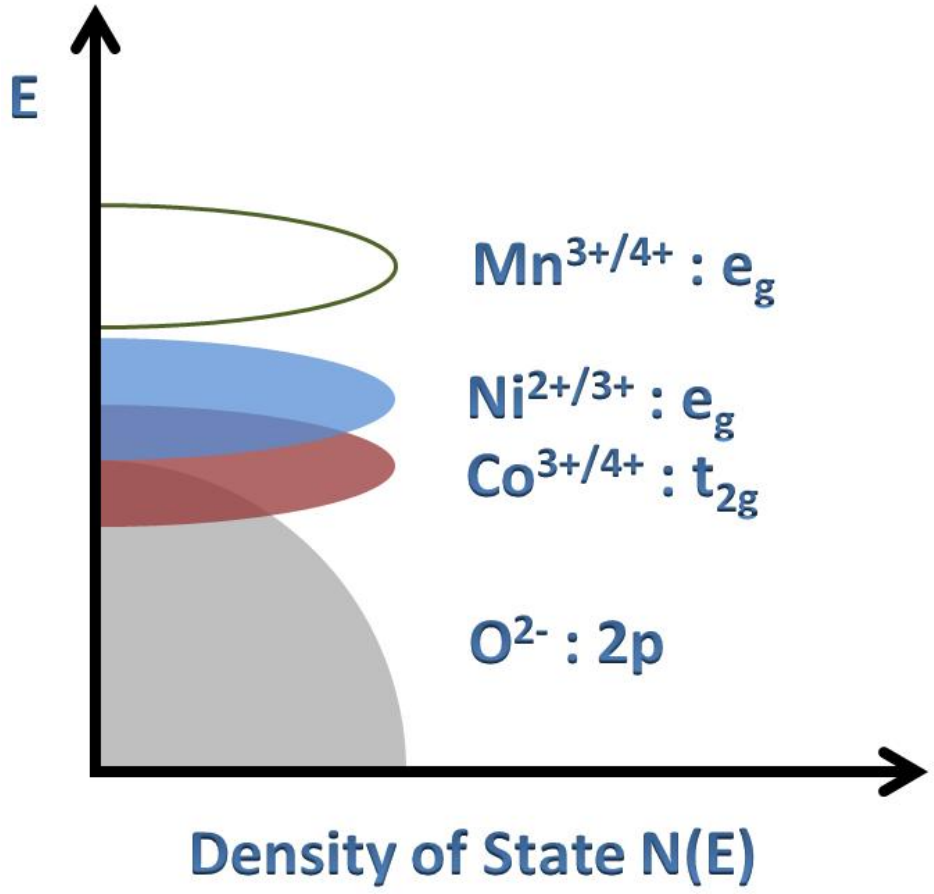

Figure 5.6. Qualitative energy diagram depicting the relative positions of the $Mn^{3+/4+}$, $Co^{2+/3+}$, and $Ni^{2+/3+}$ redox energies relative to the top of O^{2-}:2p band.

5.4. CONCLUSIONS

Extraction of lithium from four series of spinel oxides, $LiMn_{2-x}Ni_xO_4$ ($0 \leq x \leq 0.5$) and $LiMn_{2-x}M_xO_4$ ($0 \leq x \leq 1.0$) (M = Cr, Fe, and Co), with acid has been investigated systematically with an aim to establish the lithium extraction mechanism. XRD and chemical-compositional analysis data establish that the lithium extraction from spinel oxides occurs by a disproportionation of Mn^{3+} ions into Mn^{4+} and Mn^{2+} ions, with the latter being leached out into the solution, as was proposed by Hunter in 1981. The amount of lithium extracted is proportional to the amount of Mn^{3+} in the initial samples. The chemical-composition analysis of the delithiated samples in the four series of samples also reveal that other M^{3+} (M = Cr, Fe, and Co) ions in spinel oxides do not disproportionate into M^{4+} and M^{2+} ions unlike the Mn^{3+} ions. Furthermore, the data indirectly establish that the $Mn^{3+/4+}$ band does not overlap with the $Ni^{2+/3+}$ band, so in mixed oxides the $Mn^{4+} + Ni^{2+} \leftrightarrow Mn^{3+} + Ni^{3+}$ equilibrium (Reaction 5.2) lies completely towards the left and no Mn^{3+} is formed. Moreover, ion exchange of Li^+ ions by H^+ ions does not occur in spinel oxides as the H^+ ions may not be stabilized in tetrahedral sites of the spinel framework, while such ion exchange is known to occur readily in layered $LiMO_2$ oxides, as the H^+ ions may be readily stabilized in octahedral sites of the lithium layer in layered oxides.

Since only Mn^{3+} disproportionates into Mn^{4+} and Mn^{2+} while the other transition-metal ions do not, the study suggests that Mn dissolution could become much more pronounced than other transition-metal-ion dissolutions in mixed-metal oxide cathodes in the presence of trace amounts (ppm levels) of acid (*e.g.*, HF) in the electrolyte when the

cells are operated within the electrolyte stability region of < 4.3 V vs. Li/Li^+. However, at higher operating voltages (> 4.3 V vs. Li/Li^+), the cathode surface could become unstable in contact with the organic liquid electrolyte, which could lead to the dissolution of other metal-ions as well, even when no Mn^{3+} ions are present in the samples. Moreover, the chemical instability of cobalt-rich compositions due to an overlap of the $Co^{3+/4+}$:3d band with the top of the O^{2-}:2p band (Figure 5.4) could further exacerbate the metal-ion dissolution since the oxidation of O^{2-} ions at higher operating voltages of > 4.3 V in the Co-containing samples[198] could promote the chemical reactivity and side reactions of the cathode with the electrolyte. Although the present work has been carried out at a much higher concentration of acid than would be encountered in an actual lithium-ion cell, the results clearly provide a trend and could provide insights in designing high-performance cathodes for lithium-ion batteries.

Chapter 6: On the Utility of Spinel Oxide Hosts for Magnesium-ion and Zinc-ion Batteries*

6.1. INTRODUCTION

Li-ion batteries have become increasingly prevalent in modern society as they power personal electronic devices and automobiles due to their high energy density.[176] There are several issues, however, with Li-ion batteries, such as safety concerns, high cost, and limited charge-storage capacity.[176] With an aim to increase the capacity, much attention is focused towards multivalent cation systems (Mg^{2+}, Zn^{2+}, Al^{3+}, *etc.*) because of their ability to hold greater amounts of charge.[216-222] Mg-ion batteries also offer additional advantages such as reduced cost and better safety with Mg-metal anodes.[180] However, Mg-ion batteries pose numerous challenges such as incompatibility of Mg-metal anode with non-aqueous electrolytes due to the formation of a passivating layer that blocks Mg-ion diffusion, poor kinetics of Mg^{2+}-ion diffusion, lack of electrolytes with wide stability windows, and lack of cathode hosts with high operating voltages.[180]

Significant efforts are being put into finding suitable cathodes for Mg-ion batteries, but it is challenging due to the 2+ charge on Mg^{2+} ions, which leads to strong interactions with the host structure ions that limit the Mg diffusion kinetics.[223] This leads to the failure of most metal-oxide hosts analogous to lithium-ion cathodes as Mg-insertion hosts. The most successful cathodes to date are Chevrel-phase compounds

* Portions of this chapter have been submitted for publication as J. C. Knight, S. Therese, and A. Manthiram, "On the Utility of Spinel Oxide Hosts for Magnesium-ion Batteries", *ACS Applied Materials and Interfaces*, submitted 2015, and J. C. Knight, S. Therese, and A. Manthiram, "Chemical Extraction of Zn from $ZnMn_2O_4$-based Spinels", *Journal of Materials Chemistry A*, submitted 2015.
J. C. Knight carried out the experimental work with assistance from S. Therese. A. Manthiram supervised the research. All participated in preparing the manuscripts.

based on Mo_6S_8, which is able to accommodate the electrons within the Mo_6-clusters.[224] However, despite good cyclability, the Chevrel-phase is not promising for commercial applications because of their low operating voltage and capacity.[225-228] Other materials that have inserted Mg to various extents, include V_2O_5,[223, 229] MoO_3,[230] olivine silicates,[231, 232] and fluorinated graphite,[233, 234] amongst others.[235-240] Theoretical calculations have suggested the post-spinel structure, which is a denser polymorph of the spinel structure formed under high pressure with distorted MO_6 octahedra, may be a suitable host, but this has not been experimentally confirmed.[241]

There is interest in Zn-ion batteries being utilized for electrical grid storage due to the safety, lower cost, use of aqueous electrolyte, and abundance of Zn compared to Li.[220] Kang *et al.* proposed a rechargeable Zn-ion battery utilizing an α-MnO_2 cathode, a zinc metal anode, and an aqueous electrolyte with either $ZnSO_4$ or $Zn(NO_3)_2$ as the electrolyte.[218, 219] They were able to deliver a capacity of 210 mAh/g at an operating voltage of 1.3 V, which is superior to any published Mg-ion battery system. However, this system suffers from initial capacity fade and poor rate capability, so significant improvements are necessary.

The spinels are another family of materials being studied as potential cathodes for Mg- and Zn-ion batteries because of their success in Li-ion batteries, fast ion diffusion derived from its 3-dimensional ion mobility, high operating voltage, and structural stability.[176] Spinels have the chemical formula AB_2O_4, where the oxide ions form a cubic-close-packed structure. The A ions reside in 8a tetrahedral sites, and the B ions reside in alternating octahedral sites along the three crystallographic axes, designated as

16d sites. The remaining empty octahedral sites are designated as 16c sites. In fact, several researchers claim to have used spinel-structured Mn_2O_4 (λ-MnO_2) to intercalate Mg^{2+} ions in aqueous environments.[242, 243] Kim *et al.* recently verified the intercalation of Mg ions into λ-MnO_2 through the use of high-resolution imaging, spectroscopic measurements, and structural diffraction analysis.[244] They found that Mg^{2+} ions could be reversibly inserted into the spinel structure and that water molecules do not accompany the Mg ions into the structure.

Because of the success of spinel $LiMn_2O_4$ as a Li-ion battery cathode, an investigation of the mechanism of Mg/Zn extraction from $MgMn_2O_4$/$ZnMn_2O_4$ and other Mg-/Zn-spinels could provide important insights into their applicability as multivalent-ion battery cathodes. With this perspective, we employ two different chemical methods to attempt to extract Mg and Zn from the spinel structure. The samples studied include $Mg_{1+x}Mn_{2-x}O_4$ (x = 0, 0.1, and 0.5), $MgMnAlO_4$, and $ZnMn_{2-x}Ni_xO_4$ (x = 0, 0.5, and 1). The first method uses dilute H_2SO_4 medium to extract Mg or Zn. Hunter used this method previously to remove Li from $LiMn_2O_4$, involving the disproportionation of Mn^{3+} ions into Mn^{4+} and Mn^{2+} and resulting in the formation of λ-MnO_2 maintaining the Mn_2O_4 spinel framework.[2] The mechanism is shown below in Reaction 6.1:

$$LiMn_2^{3.5+}O_4 \rightarrow 0.75Mn_2^{4+}O_4 + 0.5MnO + 0.5Li_2O \qquad (6.1)$$

The MnO and Li_2O are soluble in the acidic medium used, so only the Mn_2O_4 powder is left. Technically, $Mn_{1.5}O_3$ is the composition of the remaining solid, but it has been normalized to indicate that it still has the spinel structure.

We have previously used this method in Chapter 5 to examine the delithiation mechanism of doped $LiMn_2O_4$ and demonstrated that the amount of delithiation is dependent on the amount of Mn^{3+} ions present in the structure.[245] This will be referred to as acid demagnesiation in this study. The second method will be referred to as chemical demagnesiation in this study, and it involves stirring the samples in an acetonitrile solution containing the oxidizer NO_2BF_4. This reaction mechanism is controlled by the amount of NO_2BF_4 used, as opposed to the acid treatment, which depends on the material composition, viz., Mn^{3+} content. The ability to extract Mg^{2+} or Zn^{2+} oxidatively with the oxidizing agent NO_2BF_4 can shed light on whether or not spinels can serve as potential hosts for Mg-ion batteries. The samples before and after the treatments are characterized by compositional and structural analyses to elucidate the Mg and Zn extraction mechanisms.

6.2. EXPERIMENTAL

6.2.1. Synthesis

The Mg-spinel samples were synthesized with a sol-gel method, and a representative description is given here. Required amounts of Mg acetate, Mn acetate, and Al nitrate were dissolved in 100 mL of stirring deionized (DI) water. The total amount of metal ions was 0.025 mol in each reaction. Citric acid was then dissolved in the solution, with a 1 : 1 mol ratio of metal ions to citric acid. The solution was stirred and heated on a hot plate until all of the liquid evaporated. The resulting material was calcined in a furnace to 450 °C for 5 h with heating and cooling rates of 3 °C/min. The

powder obtained was then pelletized and heated at a designated temperature for 12 h with a heating rate of 3 °C/min, followed by quenching into liquid nitrogen. $MgMn_2O_4$, $Mg_{1.1}Mn_{1.9}O_4$, and $MgMnAlO_4$ were calcined at 1000 °C, while $Mg_{1.5}Mn_{1.5}O_4$ was calcined at 850 °C. An additional $MgMn_2O_4$ sample was calcined at 1200 °C. After this high temperature heat treatment, some samples were annealed at 400 °C for 12 h with heating and cooling rates of 3 °C/min.

The $ZnMn_{2-x}Ni_xO_4$ samples were synthesized by an oxalate decomposition method. Three samples with x = 0, 0.5, and 1 were synthesized, and they are referred to hereafter as Zn 0, Zn 0.5, and Zn 1. Required amounts of zinc acetate (Acros, 98%), manganese acetate (Acros, 99+%), and nickel acetate (Acros, 99+%) were dissolved in 100 mL of deionized (DI) water, so that the total amount of metal ions in the resulting solution was 0.045 M. Oxalic acid (Fisher, 99%) was dissolved in a separate beaker of deionized water and heated to 80 °C. A 5% molar excess of oxalic acid was used, so that the molar ratio of total metal ions to oxalic acid was 1 : 1.05. The metal acetate solution was then quickly added to the oxalic acid solution and allowed to stir for 60 min. The precipitated powder was then filtered and dried overnight in an air oven at 100 °C. The dried powder was then pelletized and heated at high temperatures for 12 h with heating and cooling rates of, respectively, 3 °C/min and 1 °C/min. The heating temperature varied from sample to sample. Zn 0 and Zn 0.5 were heated at 900 °C, while Zn 1 was heated at 680 °C.

6.2.2. Chemical Treatments and Characterization

Two different methods were utilized to extract magnesium or zinc from the spinel lattice. The acid treatment involved the addition of 0.25 g of active material to 25 mL of 0.35 N H_2SO_4 and stirring in a flask for 24 h. The product was then recovered by filtration and dried at 100 °C overnight. The chemical treatment involved placing 0.25 g of active material in a flask inside an Ar-filled glovebox, followed by the addition of 1 g of NO_2BF_4 and capping the flask. Then, 10 mL of anhydrous acetonitrile was added into the capped flask and stirred for 24 h under Ar with a Schlenk line. The product formed was recovered after filtration with acetonitrile and acetone and drying overnight at 100 °C.

The samples were characterized before and after the treatment with acid or NO_2BF_4 by XRD and inductively coupled plasma (ICP) analysis. A Varian 715-ES was used for ICP analysis. The ICP values had an error bar of ± 0.02, and the percent relative standard deviations (% RSDs) for each measurement were under 3%. XRD analysis was carried out with a Rigaku Miniflex 600 with Cu Kα radiation at 10° – 80° with a step size of 0.02° and a scan rate of 2°/min. Cation disorder values for the $MgMn_2O_4$ samples were obtained by the Rietveld refinement method using the General Structure Analysis Software (GSAS, Los Alamos National Laboratory) program. The tetragonal spinel structure ($I4_1/amd$) was used for the refinement for all the samples, allowing both the Mg and Mn ions to reside in the tetrahedral and octahedral sites. Fourier transform infrared spectroscopy (FTIR) analysis was carried out with pelletized KBr samples employing a Thermo Fisher Scientific Nicolet iS5 instrument.

6.3. RESULTS AND DISCUSSION

6.3.1. Acid Treatment of $MgMn_2O_4$

The first compound studied was $MgMn_2O_4$, which is structurally similar to spinel $LiMn_2O_4$. The Mg ions reside in the 8a tetrahedral sites like Li, and the Mn ions reside in the 16d octahedral sites. However, there are some key differences between the two materials. In $LiMn_2O_4$, half of the Mn ions are in the 3+ state and half are in the 4+ state, whereas $MgMn_2O_4$ has all Mn^{3+} ions due to the higher valence of Mg. This increase in Jahn-Teller active Mn^{3+} ions causes $MgMn_2O_4$ to be a tetragonal spinel instead of the cubic spinel. Another variation between the structures is the degree of cation disorder in them. Cation disorder refers to ions supposedly in the tetrahedral sites residing in the octahedral sites and vice versa.[246] The degree of cation disorder in spinel structures is influenced by several factors, including composition, ionic size, ion valence state, octahedral site stabilization energies, calcining temperature, and cooling rate.[247-250] Due to the large size and charge differences between Li^+ and $Mn^{3+/4+}$ ions, the Li spinel possesses essentially no cation disorder. On the other hand, $MgMn_2O_4$ can experience significant cation disorder because Mg^{2+} and Mn^{3+} ions are closer in size and charge. Various degrees of cation disorder can be created by altering the heating protocol.[246, 251-258] Cation disorder can also affect the oxidation state of ions in the prepared samples. For example, when an Mg^{2+} ion moves to an octahedral site, it remains an Mg^{2+} ion. However, when an Mn^{3+} ion migrates to a tetrahedral site to take the place of an Mg^{2+} ion, it is reduced to Mn^{2+} and creates a corresponding Mn^{4+} ion in an octahedral site. The

average Mn oxidation state is still the same, but this can affect other properties of the material.

Four samples with different amounts of cation disorder were created, and their XRD patterns can be seen in Figure 6.1, as well as a reference pattern for ordered $MgMn_2O_4$. Two samples, which will be referred to as Mg 1200 and Mg 1000, were obtained by quenching, respectively, from 1200 °C and 1000 °C. The other two samples, which will be referred to as Mg 1200A and Mg 1000A, were obtained by annealing at 400 °C after quenching from 1200 °C and 1000 °C, respectively. Going from the most disordered to the least disordered, the samples are Mg 1200, Mg 1000, Mg 1200A, and Mg 1000A. A higher firing temperature promotes disorder by imparting greater thermal energy to the ions, making them more likely to hop to energetically unfavorable sites. Quenching the samples in liquid nitrogen attempts to lock in the high temperature cation configuration at ambient temperatures. Annealing the samples at a lower temperature after quenching allows for the more thermodynamically stable cation arrangement to form. Mg 1000 and Mg 1200 produce very similar patterns, except for changes in peak intensity. The annealed samples, however, show significant shifts in peak positions, as the reduction in cation disorder alters the lattice parameters. The two annealed samples are similar to each other, just as the two quenched samples are, except for changes in peak intensity.

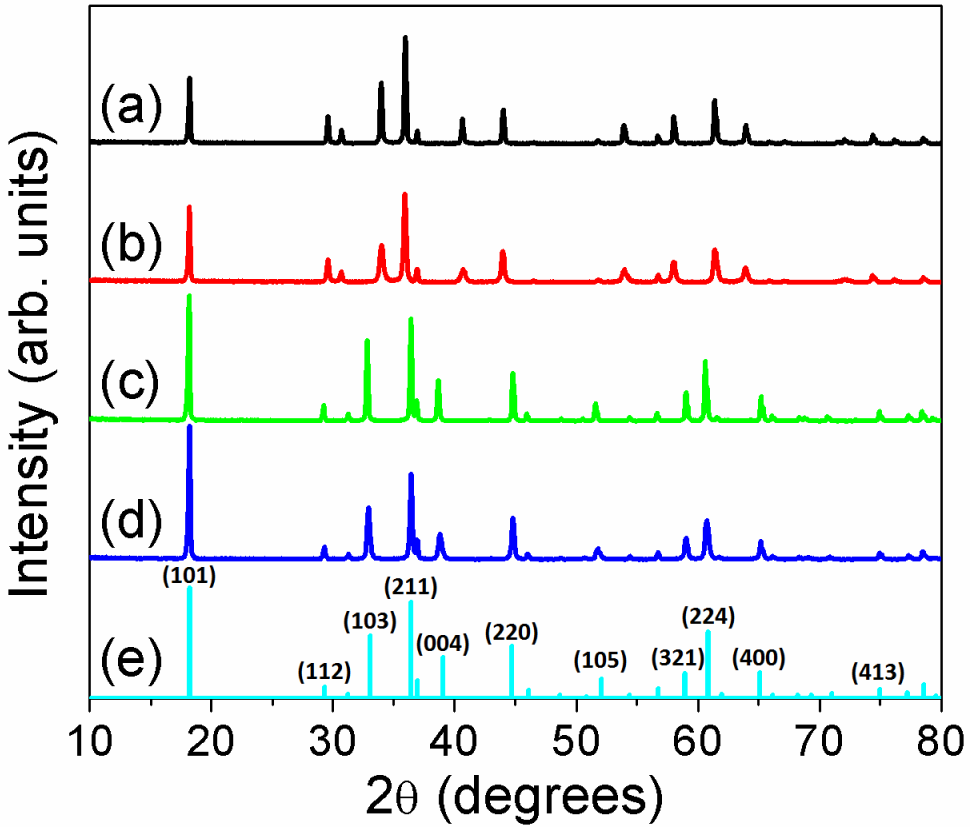

Figure 6.1. XRD patterns of the four $MgMn_2O_4$ starting materials with varying degrees of cation disorder: (a) Mg 1200, (b) Mg 1000, (c) Mg 1200A, and (d) Mg 1000A. A reference pattern for the ordered $MgMn_2O_4$ is given in (e).

A qualitative method of comparing the cation disorder between samples is to look at the peak ratios of the (101) and (211) peaks.[256] The (211) peak at ~ 36.3° is often the most intense peak in the $MgMn_2O_4$ pattern, and it is not sensitive to changes in cation disorder. Conversely, the (101) peak at ~ 18.5° drastically decreases in intensity with increasing cation disorder, so an increasing ratio of the (101) to (211) peaks qualitatively shows a decrease in cation disorder. To quantify the cation disorder, however, Rietveld

refinement was used. The findings can be found in Table 6.1, where the inversion degree refers to the fractional amount of Mg ions that migrate out of the tetrahedral sites and reside in the 16d octahedral sites. The samples are listed from the most disordered to the least disordered, with the most disordered sample Mg 1200 at the top. The Rietveld refinement data confirms the previously described ranking of cation disorder amongst the samples.

Table 6.1. The inversion degree (cation disorder) in the four $MgMn_2O_4$ samples and the theoretical and experimental Mg content after acid treatment of the 7 $Mg_{1+x}Mn_{2-x}O_4$ samples

Sample	Inversion Degree	Expected Composition After Acid Treatment	Mg Content After Single Acid Treatment	Actual Composition After Acid Treatment
Mg 1200	34%	Mn_2O_4	0.46	$Mg_{0.06}Mn_2O_4$
Mg 1000	29%	Mn_2O_4	0.31	$Mg_{0.05}Mn_2O_4$
Mg 1200A	6%	Mn_2O_4	0.13	$Mg_{0.06}Mn_2O_4$
Mg 1000A	1%	Mn_2O_4	0.05	$Mg_{0.05}Mn_2O_4$
Mg 1.1	–	$Mg_{0.36}Mn_{1.82}O_4$	0.31	$Mg_{0.02}Mn_{1.82}O_4$
Mg 1.1A	–	$Mg_{0.36}Mn_{1.82}O_4$	0.08	$Mg_{0.08}Mn_{1.82}O_4$
Mg 1.5	–	$Mg_{1.33}Mn_{1.33}O_4$	0.63	$Mg_{0.14}Mn_{1.33}O_4$

As Hunter previously showed,[2] $LiMn_2O_4$ can be fully delithiated by treating with dilute H_2SO_4 as depicted earlier in Reaction 6.1. Despite the change in the oxidation state of Mn, $MgMn_2O_4$ should experience full Mg extraction as well, which is illustrated in Reaction 6.2:

$$MgMn_2^{3+}O_4 \rightarrow 0.5Mn_2^{4+}O_4 + MnO + MgO \qquad (6.2)$$

The MnO and MgO are again soluble, leaving behind only Mn_2O_4 (technically MnO_2). All four samples were stirred with acid for 24 h, and their XRD patterns after acid treatment are shown in Figure 6.2, along with a reference pattern for λ-MnO_2. The XRD patterns for all samples, except Mg 1000A, showed several additional peaks in addition to those of the expected λ-MnO_2 pattern, signaling incomplete Mg extraction. Indeed, ICP analysis showed that the samples, except Mg 1000A, had significant amounts of Mg remaining in the structure. Those Mg content values are listed in Table 6.1. This is in contrast to our previous study, where all reactions were completed in this time frame.[245] Figure 6.2 also demonstrates the effect that cation ordering has on the structure of the acid-treated materials. Mg 1200 has almost half of the Mg remaining, so despite its high degree of cation disorder, it still has several peaks from the parent tetragonal spinel structure. Mg 1000, despite having significant Mg remaining in the structure, has relatively weak tetragonal spinel peaks remaining due to the disordered nature of the starting material. On the other hand, Mg 1200A experiences a higher degree of Mg extraction than Mg 1200 and Mg 1000, but it still produces a two-phase material with clear XRD reflections after acid treatment since the starting tetragonal spinel phase was well crystalline and ordered. Finally, Mg 1000A exhibits a single-phase λ-MnO_2 pattern after acid treatment because of the essentially complete Mg extraction and its highly ordered starting material, which allows for a more crystalline material after treatment. It should also be noted that as the cation disorder decreases, the amount of Mg extracted increases. In other words, increasing cation order increases the rate of Mg removal. The

relationship is somewhat linear as depicted in Figure 6.3. Further discussion of this topic will appear in the next section.

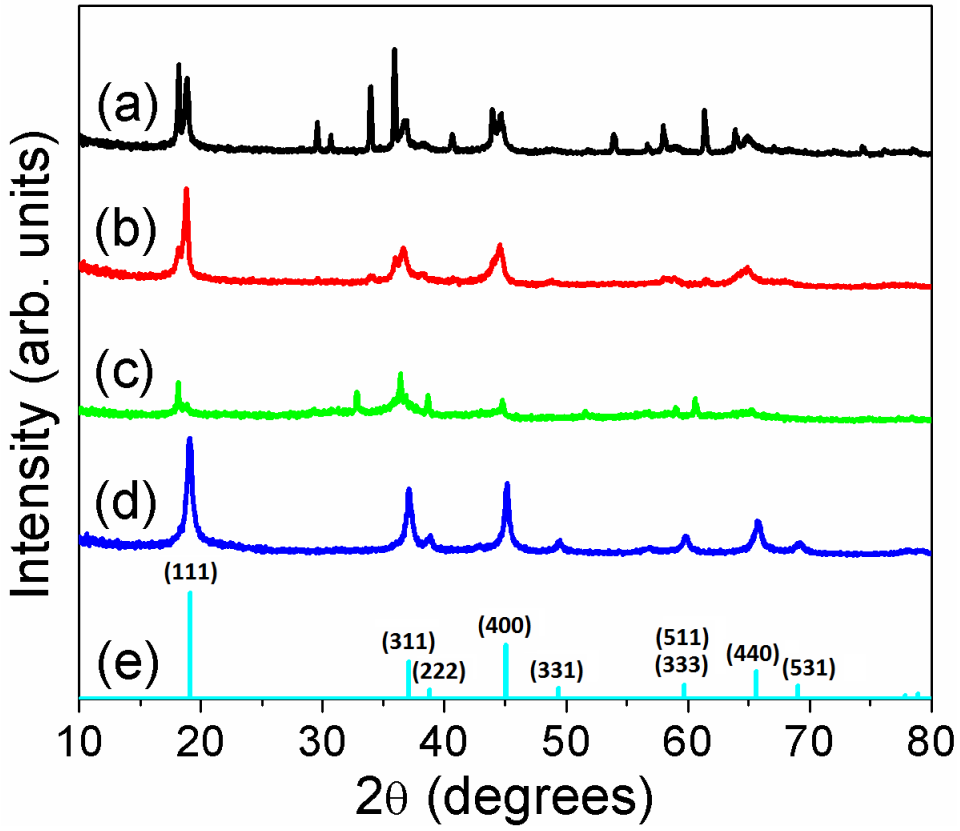

Figure 6.2. XRD patterns of the four $MgMn_2O_4$ samples with varying degrees of cation disorder after their first acid treatment: (a) Mg 1200, (b) Mg 1000, (c) Mg 1200A, and (d) Mg 1000A. A reference pattern for λ-MnO_2 is given in (e).

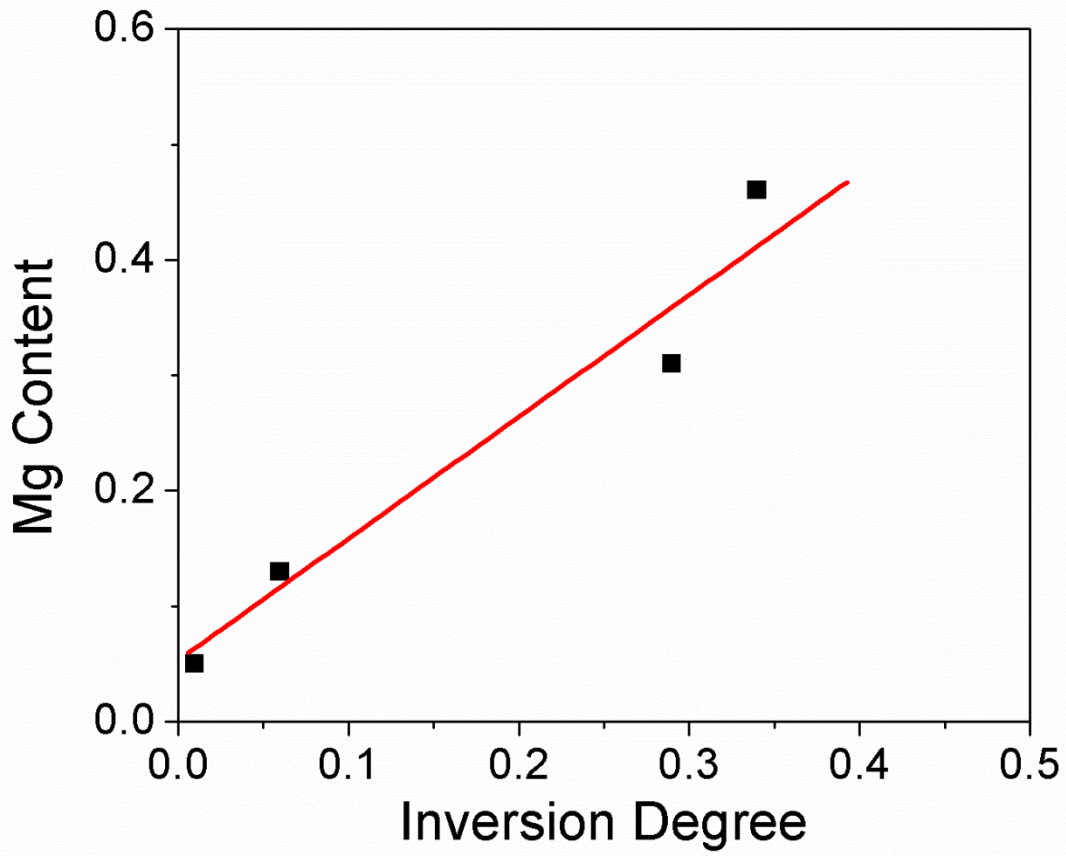

Figure 6.3. Plot of inversion degree (cation disorder) vs. Mg content after a single acid treatment for the four $MgMn_2O_4$ samples with various heating protocols. A linear fit is also included.

There may be a couple of forces causing the incomplete Mg removal. The most likely cause is the increased electrostatic repulsion felt by Mg^{2+} ions as they have a higher charge than Li^+ ions. In order to be extracted from the structure, the Mg^{2+} ions must diffuse between the 8a tetrahedral and 16c octahedral sites from the interior to the surface of the particle, so the increased repulsion between the Mg^{2+} ions in the 8a tetrahedral and 16c octahedral sites may inhibit Mg^{2+} ion diffusion through these sites. A secondary factor could be the difference in the ionic sizes and masses between Mg^{2+} and

Li^+. However, Li^+ ions, with 0.59 Å in tetrahedral sites and 0.76 Å in octahedral sites, are only slightly larger than Mg^{2+} ions, with 0.57 Å in tetrahedral sites and 0.72 Å in octahedral sites, so the size difference should not affect the extraction rate much. $MgMn_2O_4$, however, has all Mn^{3+} ions (unless Mn^{4+} ions are created through cation disorder), which are larger (0.645 Å) than Mn^{4+} ions (0.53 Å). The $LiMn_2O_4$ structure has a much higher amount of the smaller Mn^{4+} ions present, possibly allowing for better ion transport. On the other hand, this size argument contradicts the finding that increased ordering leads to faster Mg removal. In a highly ordered $MgMn_2O_4$ sample, there should be almost no Mn^{4+} ions, so only the larger Mn^{3+} ions are present, which should slow down Mg removal. This, however, does not match with the experimental outcomes. The differences in the atomic masses of Li^+ (6.94 g mol^{-1}) and Mg^{2+} (24.35 g mol^{-1}), on the other hand, can slow down Mg^{2+} diffusion.

In order to see if Mg could be fully extracted from the samples, additional acid treatments were carried out after filtering and washing the samples. Mg 1000A was deemed fully converted after the first acid treatment. Mg 1200 and Mg 1000 required two additional treatments, while Mg 1200A required one more. The final Mg contents of the materials are listed in Table 6.1. The XRD patterns of these final materials are displayed in Figure 6.4 along with a λ-MnO_2 reference pattern. Clearly, increased cation ordering in the starting material led to a more crystalline phase after acid treatment. Only Mg 1000A produced a single-phase material of the expected λ-MnO_2. The other samples produced less crystalline samples with some additional peaks from other Mn oxides.

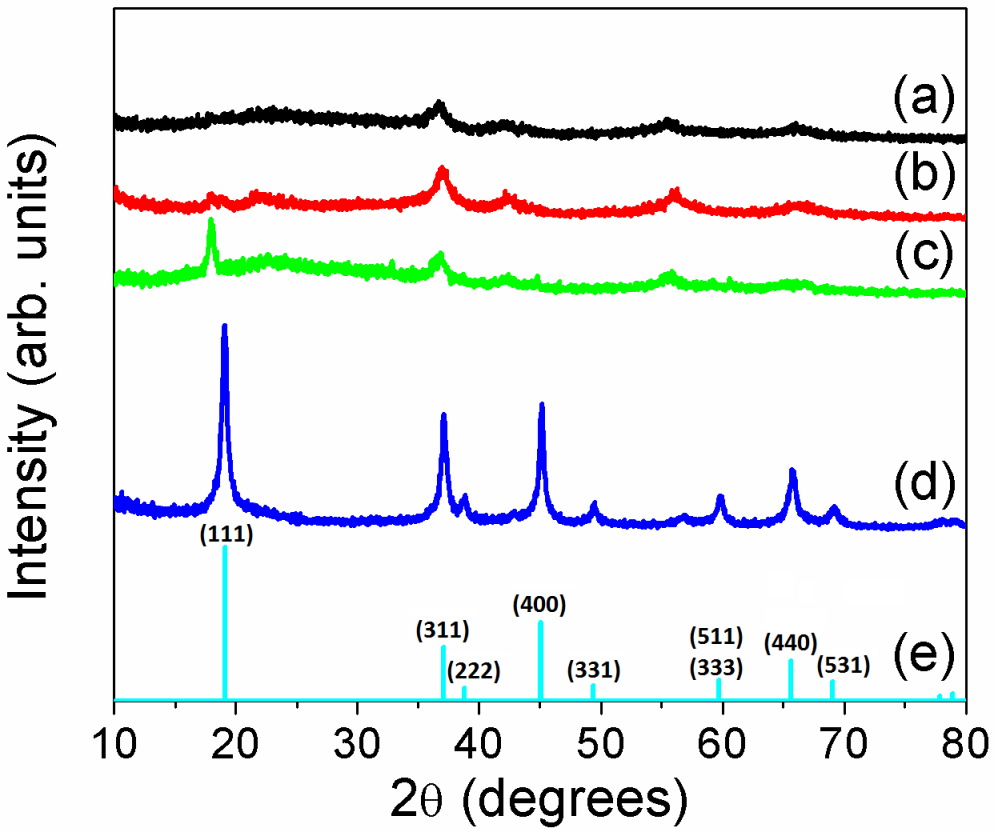

Figure 6.4. XRD patterns of the four $MgMn_2O_4$ samples with varying degrees of cation disorder after multiple acid treatments and full Mg removal: (a) Mg 1200, (b) Mg 1000, (c) Mg 1200A, and (d) Mg 1000A. A reference pattern for λ-MnO_2 is given in (e).

6.3.2. Acid Treatment of $Mg_{1+x}Mn_{2-x}O_4$

Additional samples were made to test the effect of Mn oxidation state on the acid treatment mechanism. The Mn oxidation state was altered by replacing some Mn by Mg in the series $Mg_{1+x}Mn_{2-x}O_4$. As the Mg content (or *x* value) increases, the Mn oxidation state increases to maintain charge neutrality. The samples synthesized were $Mg_{1.1}Mn_{1.9}O_4$ (Mg 1.1) and $Mg_{1.5}Mn_{1.5}O_4$ (Mg 1.5), which have average Mn oxidation

states of 3.05+ and 3.33+, respectively. Other compositions were attempted, but they all produced a mixture of cubic and tetragonal phases. A third sample was created by annealing an Mg 1.1 sample, hereafter referred to as Mg 1.1A. Even if these samples are perfectly ordered, some (*x* amount) Mg^{2+} ions are located on the octahedral sites. As they are replacing Mn^{3+} ions, they also create a corresponding number of Mn^{4+} ions, which is what causes the increased Mn oxidation state. The XRD patterns of the three starting materials and a reference pattern of a cubic Mg spinel are shown in Figure 6.5. The Mg 1.1 sample is a single-phase tetragonal spinel, and the Mg 1.1A sample shows the expected significant peak shift due to changes in the cation disorder. The pattern for Mg 1.5 is surprising, however. As mentioned above, the average Mn oxidation state in Mg 1.5 is 3.33+. This compound is expected to be a tetragonal spinel because the average Mn oxidation state is below 3.5+, but this is not the case, as Mg 1.5 forms a cubic spinel. This is due to the cation disorder in the sample. It was previously stated that when Mn^{3+} ions migrate to 8a tetrahedral sites, they are reduced to Mn^{2+} ions and oxidize a corresponding amount of Mn^{3+} ions to Mn^{4+} in the 16d octahedral sites. If this process occurs enough, the average oxidation state of the Mn ions in the octahedral sites will reach above 3.5+, causing the structure to convert to a cubic spinel. While the average Mn oxidation state of the entire structure is still 3.33+, the Mn ions in the 16d octahedral sites have an average oxidation state of > 3.5+, which is what actually determines the tetragonal vs. cubic phase formation.

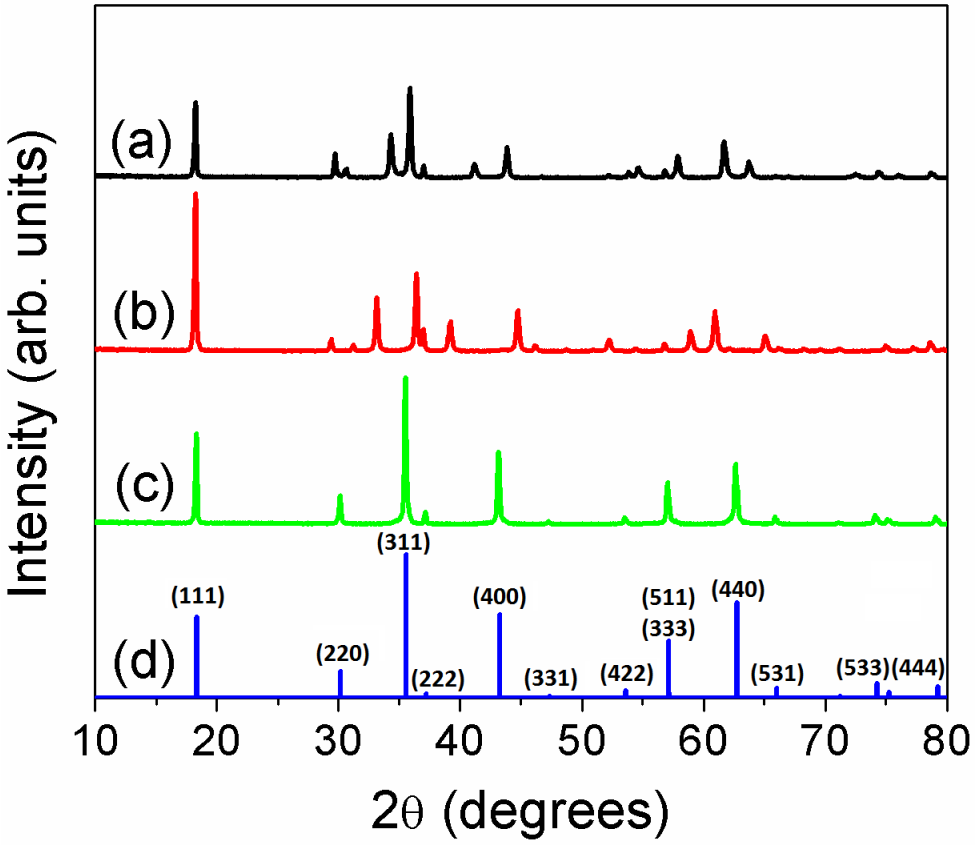

Figure 6.5. XRD patterns of the starting materials of the three samples in the $Mg_{1+x}Mn_{2-x}O_4$ series: (a) Mg 1.1, (b) Mg 1.1A, and (c) Mg 1.5. A reference pattern for a cubic Mg spinel is shown in (d).

Because raising the Mn oxidation state limits the extraction of Mg by the acid treatment mechanism, these samples are not expected to experience full Mg extraction. Table 6.1 details the expected final composition of the material left behind after acid treatment, which shows that significant Mg should remain in the structures after acid treatment. Reactions 6.3 and 6.4 convey the expected mechanism of Mg extraction in these two compounds:

$$Mg_{1.1}Mn_{1.9}^{3.05+}O_4 \rightarrow 0.55Mg_{0.36}Mn_{1.82}^{4+}O_4 + 0.9MnO + 0.9MgO \quad (6.3)$$

$$Mg_{1.5}Mn_{1.5}^{3.33+}O_4 \rightarrow 0.75Mg_{1.33}Mn_{1.33}^{4+}O_4 + 0.5MnO + 0.5MgO \quad (6.4)$$

Table 6.1 shows, however, that after a single acid treatment, all three samples, especially Mg 1.1A and Mg 1.5, have substantially less Mg than expected if only Hunter's mechanism is occurring. It also shows that, as expected, Mg 1.1A had a much higher rate of Mg extraction than Mg 1.1. To see if Mg could be fully extracted from these samples, additional acid treatments were performed on Mg 1.1 and Mg 1.5. It was deemed that Mg was fully extracted from Mg 1.1A after a single treatment. Mg 1.1 required an additional two acid treatments, while Mg 1.5 required an additional four treatments. Mg 1.1 experienced full Mg extraction, and Mg 1.5 nearly did, but the amount of remaining Mg 1.5 sample was too low to do further acid treatments. The final compositions can be seen in Table 6.1, and their final XRD patterns can be seen in Figure 6.6. The XRD data show the same behavior as seen in the $MgMn_2O_4$ samples. Mg 1.1A produces a much more crystalline sample after acid treatment due to the increased cation order in its starting material. The acid treated Mg 1.5 is still relatively crystalline because there is minimal cation disorder due to the increased ratio of Mg to Mn ions. Mg ions are more likely to reside in the tetrahedral sites, so increasing their population impedes Mn migration to the tetrahedral sites.

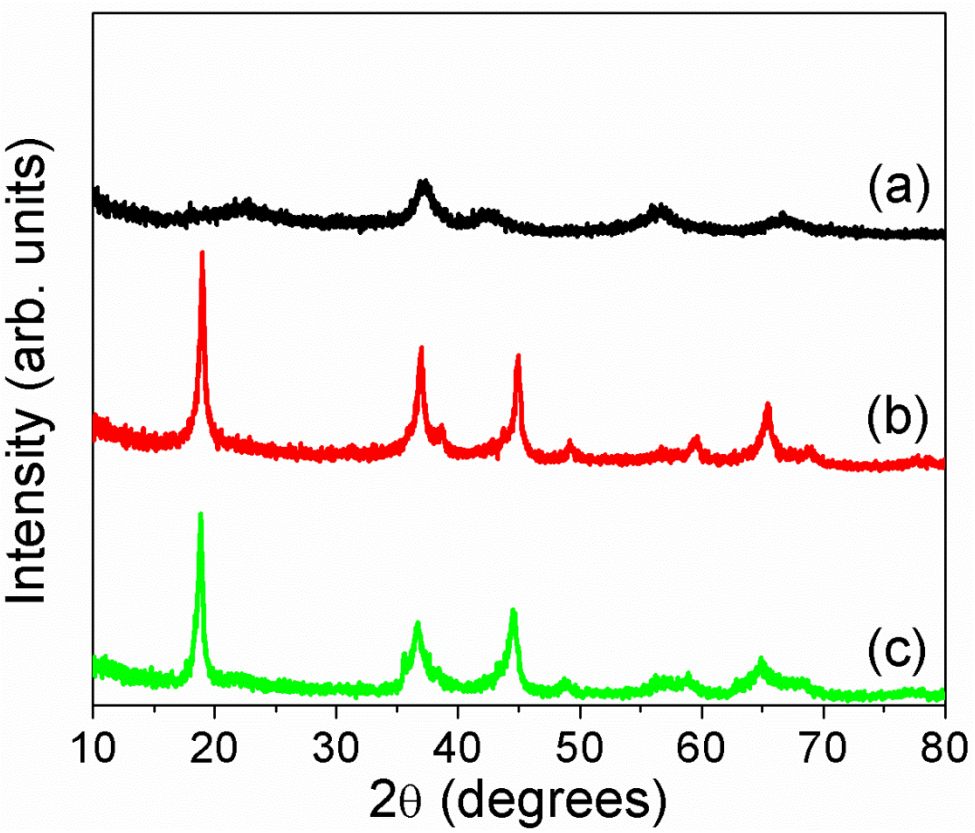

Figure 6.6. XRD patterns of the three samples in the $Mg_{1+x}Mn_{2-x}O_4$ series with full Mg removal: (a) Mg 1.1, (b) Mg 1.1A, and (c) Mg 1.5.

Because there was so much Mg removal beyond the anticipated amount, some other Mg extraction mechanism must be taking place in the $Mg_{1+x}Mn_{2-x}O_4$ samples. As Feng *et al.* previously found, Mg^{2+} ions in the octahedral sites of the spinel structure can undergo ion exchange with H^+ ions.[259] It is assumed that the same mechanism is occurring in the Mg-spinel structure as well. To confirm the ion exchange of Mg^{2+} by H^+, FTIR analysis of some representative samples were taken and can be seen in Figure 6.7. The peaks in the 400 – 800 cm^{-1} range are from the Mg-O and Mn-O stretching

vibrations. The peaks in the 1500 – 1700 cm^{-1} range correspond to the adsorbed water bending vibrations. The asymmetric stretching of carbon dioxide and water account for the peaks at ~ 2400 cm^{-1} and 3600 – 4000 cm^{-1}, respectively. This leaves the large band centered around ~ 3400 cm^{-1}, which corresponds to the lattice –OH group stretching vibration.[259] When the ion exchange reaction occurs, lattice –OH groups are formed. As the amount of Mg^{2+} ions in the octahedral sites increases from the Mg 1000 to Mg 1.1 to Mg 1.5 samples, the intensity of this band increases, signaling an increase in the degree of ion exchange reaction. For a reference, the scan of $LiMn_2O_4$ is also included. No Li^+/H^+ ion exchange occurs in this compound, so there is no band near 3400 cm^{-1}.

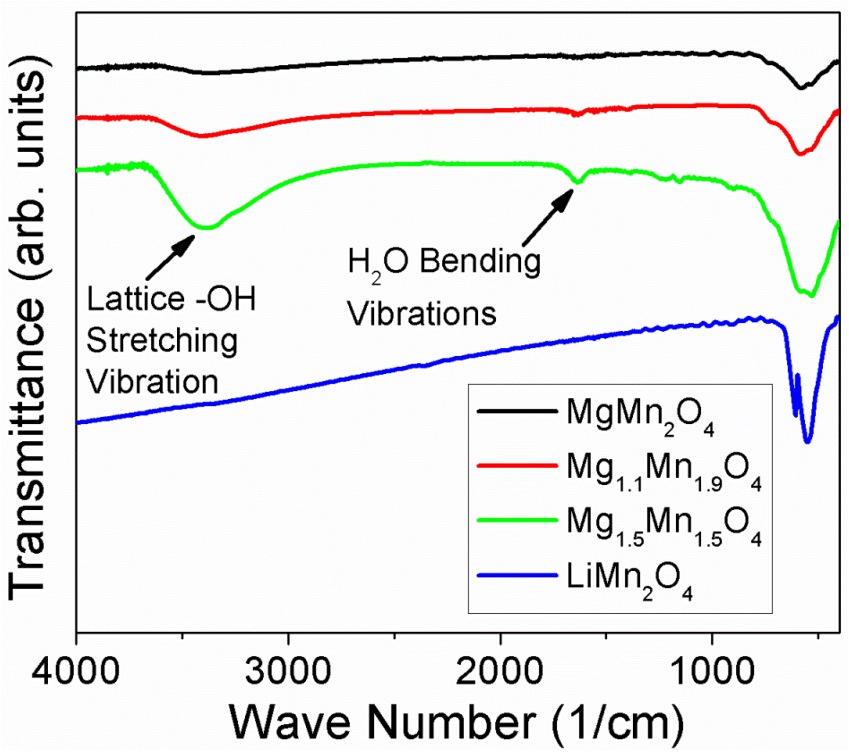

Figure 6.7. FTIR spectra of Mg and Li spinel samples: (a) Mg 1000, (b) Mg 1.1, (c) Mg 1.5, and (d) $LiMn_2O_4$.

This additional Mg extraction mechanism can further our understanding of several observations seen in this study. As previously described, cation disorder in these materials consists of Mg ions moving to octahedral sites in place of Mn ions, so samples with increased cation disorder have larger amounts of octahedral Mg^{2+} ions. Therefore, Mg extraction from the disordered $MgMn_2O_4$ samples probably proceeded via Hunter's mechanism and the ion exchange reaction, even though Mn^{3+} disproportionation alone would have been able to fully extract Mg. Looking back at the $MgMn_2O_4$ data also shows that increasing the cation disorder slows the rate of Mg extraction. Because these more disordered samples experienced more of the ion-exchange reaction, it can be assumed that the ion-exchange reaction proceeds at a slower rate than the Mn disproportionation mechanism. The ion-exchange mechanism also explains why some experimental results conflicted with the ion size discussion with $MgMn_2O_4$. The slower ion-exchange reaction has a much more detrimental effect on the rate of Mg extraction than the rate increase that might be caused by the presence of smaller Mn^{4+} ions in more disordered samples.

6.3.3. Acid Treatment of $MgMnAlO_4$

In order to further test if $MgMn_2O_4$-based spinels follow Hunter's mechanism during acid treatment, samples were synthesized by substituting an ion besides Mg for Mn in the octahedral site. The first dopant chosen was Al because it easily forms the spinel structure with Mg in the tetrahedral sites, and a couple of compositions in the $MgMn_{2-x}Al_xO_4$ series are known. The Al^{3+} ion is substituted directly for Mn^{3+}, so there is

no change to the Mn oxidation state. Unfortunately, we were only able to synthesize $MgMnAlO_4$ as a single-phase material. As discussed previously, $MgMn_2O_4$ forms in the tetragonal spinel structure, whereas $MgAl_2O_4$ adopts a cubic spinel structure. Our attempts to make other compositions in the series all produced mixtures of cubic Al-rich spinels and tetragonal Mn-rich spinels. A more thorough investigation of the phase diagram of this system could most likely produce other single-phase materials, but that was deemed outside the scope of this investigation.

The XRD patterns of $MgMnAlO_4$ before and after acid treatment are shown in Figure 6.8, and it is clear that the patterns are nearly identical, except for a slight peak intensity increase seen for the acid-treated sample. This is unexpected, as significant amounts of Mg should be removed, causing a lattice parameter decrease and corresponding peak shift to higher 2θ values. The XRD data depict a material unaltered by the acid treatment, which is also exactly what the ICP results confirm. The $MgMnAlO_4$ lost only 1% of its Mg during acid treatment. One possible explanation for this curious outcome is that there is so much Al^{3+} substitution in the 16d octahedral sites, that it impedes the Mn-Mn interaction/contact. As mentioned earlier in the text, the acid-treatment mechanism begins with 2 Mn^{3+} ions located next to each other disproportionating into a Mn^{2+} ion and a Mn^{4+} ion. The large population of Al^{3+} ions significantly reduces the likelihood of two Mn^{3+} ions being next to each other in the spinel structure, thus preventing the Mn^{3+} disproportionation mechanism. This explanation is contradicted, however, by our previous study on the acid delithiation of $LiMn_2O_4$-based samples.[245] In the $LiMn_{2-x}Cr_xO_4$ series, for example, Hunter's

mechanism was followed for x = 0, 0.25, 0.5, 0.75, and 1. For the x = 1 sample, no Li was extracted. This is the same behavior seen in $MgMnAlO_4$, but in $LiMnCrO_4$, this is expected because all Mn ions exist in the 4+ state. In the x = 0.75 sample in $LiMn_{2-x}Cr_xO_4$, however, the mechanism is followed perfectly, as ~ 20% of the Li is removed. If the Cr ions impede the Mn disproportionation process, one would expect it to have some effect on the x = 0.75 sample, but that is not the case.

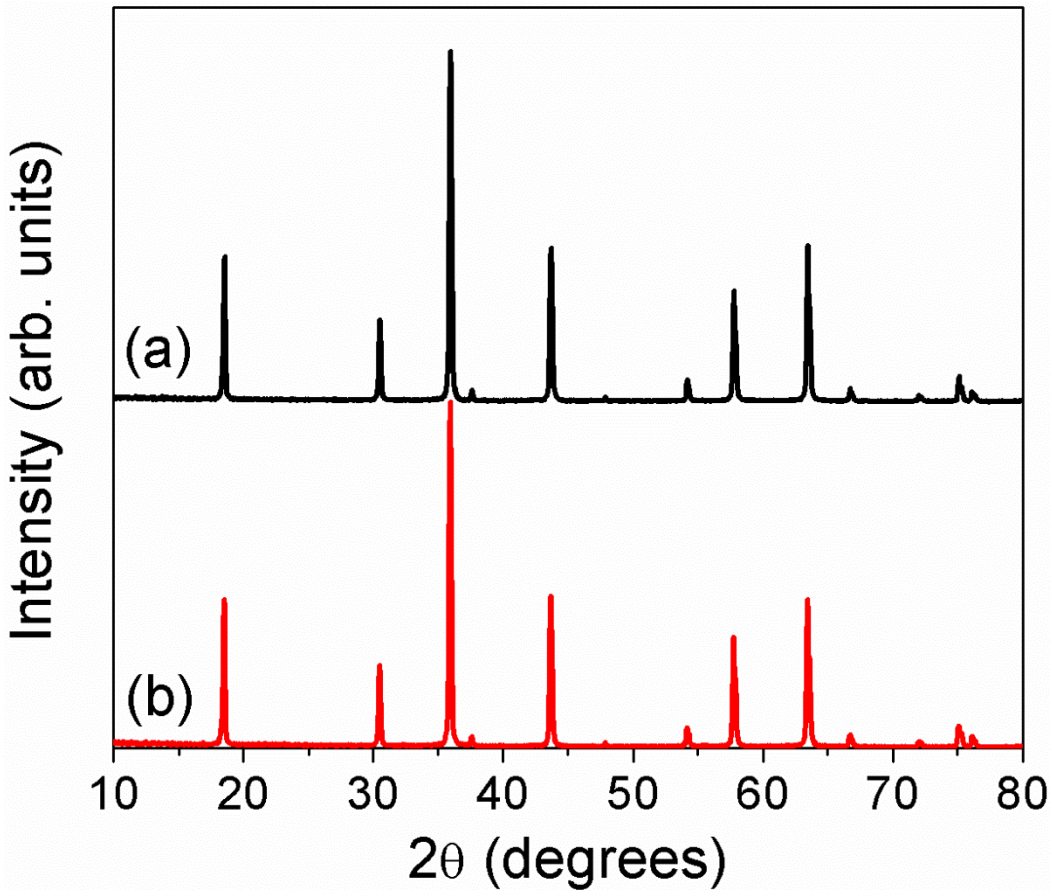

Figure 6.8. XRD patterns of $MgMnAlO_4$: (a) starting material and (b) after acid treatment.

This discrepancy between the Mg and Li spinels may be due to the nature of the dopant ion chosen. All of the dopant ions chosen in our previous study of $LiMn_{2-x}M_xO_4$ (M = Ni, Co, Cr, and Fe) are 3d transition-metal ions that can exist in multiple oxidation states. These transition-metal dopant ions, while impeding the formation of neighboring Mn^{3+} ions, still facilitate Mn^{3+} disproportionation by participating in the electron hopping/transfer across the shared octahedral edges in $LiMn_{2-x}M_xO_4$. Conversely, Al^{3+} is only capable of existing in the 3+ state in $MgMnAlO_4$, so it cannot facilitate such electron hopping/transfer. In order to test this theory, significant attempts were made at substituting Mn in $MgMn_2O_4$ with other transition metals, such as Co and Ni, that would still facilitate electron hopping/transfer across the shared octahedral edges. Different compositions and heating protocols were attempted, but unfortunately, none of these attempts were successful. Again, a more in depth synthesis and structural study of these compounds would surely produce a suitable material.

6.3.4. Chemical Treatment of Mg Spinels

Chemical treatment with NO_2BF_4 was also used to try to extract Mg from Mg spinels. NO_2BF_4 has been used extensively to study the delithiation of Li-ion battery cathodes, such as layered oxides and spinels.[198, 260, 261] Unlike acid treatment, this chemical treatment closely mirrors the oxidative processes that occur inside electrochemical cells. For instance, stirring $LiCoO_2$ with an acetonitrile solution of NO_2BF_4 causes an extraction of Li concomitant with oxidation of Co^{3+} ions to Co^{4+} ions. In $MgMn_2O_4$, the process should follow Reaction 6.5 as below:

$$MgMn_2^{3+}O_4 + xNO_2BF_4 \rightarrow Mg_{1-0.5x}Mn_2^{>3+}O_4 + xNO_2 + 0.5xMg[BF_4]_2 \quad (6.5)$$

Also unlike acid treatment, the degree of extraction is controlled by the amount of NO_2BF_4 added. If more NO_2BF_4 is added, then more Mg should be extracted. The mass ratio of NO_2BF_4 to active material used in this study was 4 : 1, which corresponds to ~ 200 % excess NO_2BF_4. For a comparison, a 2 : 1 ratio is able to fully delithiate $LiMn_2O_4$.[198]

The two samples chemically treated were $MgMn_2O_4$ and $Mg_{1.5}Mn_{1.5}O_4$, and their XRD patterns before and after the treatment with NO_2BF_4 are shown in Figure 6.9. It is clear that the chemical treatment with NO_2BF_4 essentially had no effect on the material structure as their XRD patterns are nearly identical before and after treatment. This was unexpected because removing significant amounts of Mg should decrease the lattice parameters and markedly shift the peaks to higher 2θ values. The ICP analysis, however, explains the unexpected XRD data, as both compounds showed negligible Mg removal; $MgMn_2O_4$ lost only 0.01 mol of Mg, whereas $Mg_{1.5}Mn_{1.5}O_4$ lost only 0.02 mol of Mg. This was unanticipated, especially because the same mechanism is so facile with $LiMn_2O_4$ and other Li spinels. The reason for the lack of Mg extraction may be due to the increased electrostatic repulsion that Mg^{2+} ions would feel compared to the Li^+ ions. In order to be removed from the structure, Mg ions need to diffuse from the bulk to the surface of the particle by migrating from their initial 8a tetrahedral sites to the unoccupied 16c octahedral sites and then to another 8a tetrahedral site. The electrostatic repulsion between an Mg^{2+} ion that migrated to a 16c octahedral site and an Mg^{2+} ion in a neighboring 8a tetrahedral site may be too strong to overcome, thus blocking the Mg^{2+}

ion diffusion. The addition of Mg^{2+} and Mn^{4+} ions to the 16d octahedral sites in $Mg_{1.5}Mn_{1.5}O_4$ did not produce any Mg extraction either.

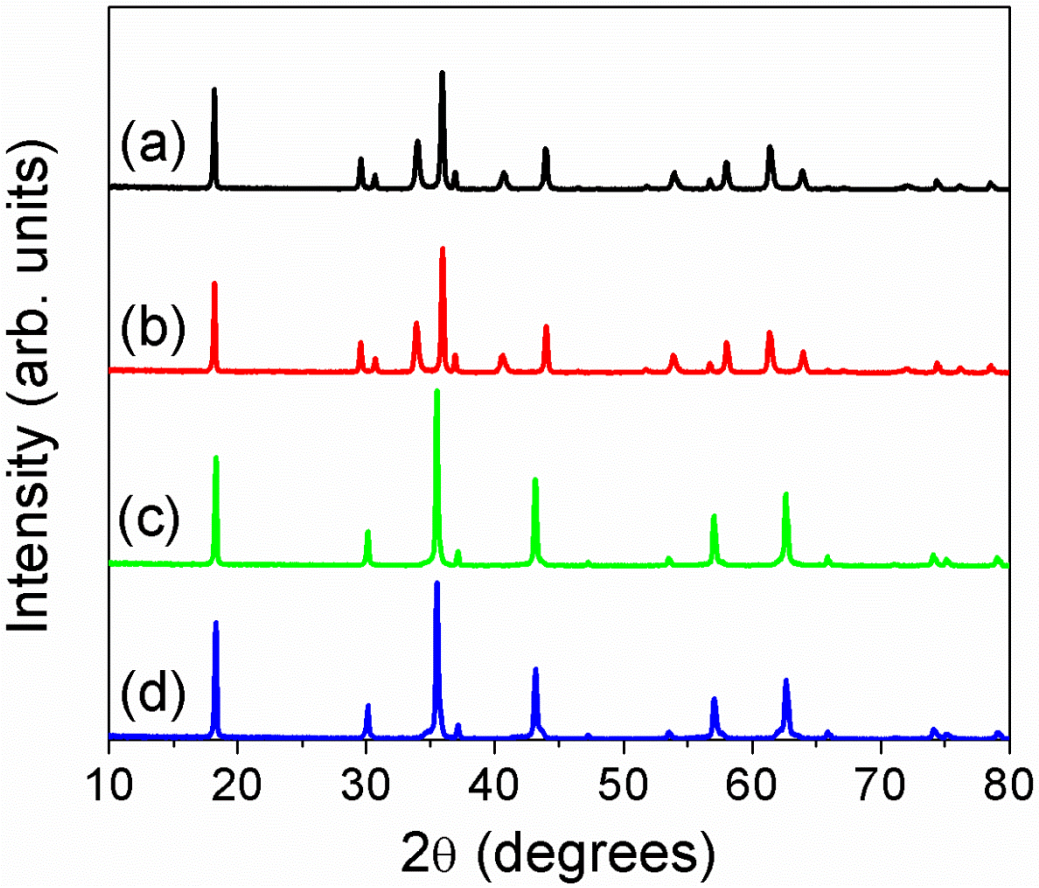

Figure 6.9. XRD patterns of the materials that underwent chemical treatment with NO_2BF_4 in acetonitrile medium: (a) Mg 1000 starting material, (b) Mg 1000 after chemical treatment, (c) Mg 1.5 starting material, and (d) Mg 1.5 after chemical treatment.

This is obviously very different behavior than was seen with the acid-treatment mechanism. Mg^{2+} ions would still have to diffuse between the 8a tetrahedral and 16c octahedral sites to be extracted during acid treatment, but the mechanism is very different in that Mn^{3+} ions are disproportionating into Mn^{2+} and Mn^{4+} ions causing significant Mn

ion migration as well as Mn ion dissolution from the lattice. The migration and dissolution of Mn ions may open up pathways with reduced electrostatic repulsion that allow the Mg^{2+} ions to diffuse through the spinel structure to be extracted. These results also seem to contradict the recent work of Kim *et al.* that verified the intercalation of Mg^{2+} into λ-MnO_2. If they were able to electrochemically insert Mg^{2+} ions into the λ-MnO_2 structure, then one would expect to be able to remove Mg^{2+} ions from the same structural framework. One possible reason for the discrepancy is the acid treatment used in their study to prepare the λ-MnO_2 altered the morphology of some particles. Almost all of the Mg insertion occurred in particles that morphed into nanoflakes with higher surface area and shorter diffusion pathways during the acid treatment, which would enhance ion migration. The particles that did not change morphology did not show significant Mg uptake. A more important factor may be the reduced electrostatic repulsion that the migrating Mg ions would experience in the initial stages of Mg insertion into the λ-MnO_2 structure that has all of the 8a tetrahedral sites empty initially. In $MgMn_2O_4$, all of the 8a tetrahedral sites are initially filled, so any Mg^{2+} ion migrating through the 16c octahedral sites would feel the repulsion from neighboring tetrahedral Mg^{2+} ions. On the other hand, when inserting Mg^{2+} ions into the λ-MnO_2 structure, there are no Mg^{2+} ions in the 8a tetrahedral sites initially, so there is no electrostatic repulsion to block Mg migration. This would allow for Mg insertion to some degree and would explain why full Mg insertion was not achieved, because once a critical mass of Mg^{2+} ions is reached in the 8a tetrahedral sites, the diffusion may be blocked by the increased electrostatic repulsion.

Combining the results from our study and other published work allows us to obtain a more complete picture of the spinel structure for use as an Mg-ion insertion host. Because NO_2BF_4 failed to extract any Mg from $MgMn_2O_4$ and $Mg_{1.5}Mn_{1.5}O_4$, it seems that the ideal spinel structure is not a viable as Mg insertion/extraction host. However, structural alterations could turn the spinel structure into a usable Mg insertion host. These alterations include synthesizing particles with high surface area and decreased ion diffusion pathways,[244] chemically removing ions to reduce electrostatic repulsion,[244] or synthesizing cation deficient spinel structures to promote Mg-ion migration.[237] The findings in this study may provide insights in designing and developing Mg-ion insertion hosts.

6.3.5. Acid Treatment of $ZnMn_{2-x}Ni_xO_4$

Reactions 6.6, 6.7, and 6.8 present the expected outcome of acid treatment on the three Zn-spinel samples used in this study:

$$ZnMn_2^{3+}O_4 \rightarrow 0.5Mn_2^{4+}O_4 + MnO + ZnO \quad (6.6)$$

$$ZnMn_{1.5}^{3.33+}Ni_{0.5}O_4 \rightarrow 0.75Zn_{0.67}Mn_{1.33}^{4+}Ni_{0.67}O_4 + 0.5MnO + 0.5ZnO \quad (6.7)$$

$$ZnMn^{4+}NiO_4 \rightarrow ZnMn^{4+}NiO_4 \quad (6.8)$$

In each case, the MnO and ZnO are soluble, leaving behind only the spinel material. It should be noted that the actual compositions of the solid materials left behind in Reactions 6.6 and 6.7 are MnO_2 and $Zn_{0.5}MnNi_{0.5}O_3$, respectively, but they have been rewritten to convey that the materials remain in the spinel structure.

The XRD patterns of the starting materials are shown in Figures 6.10a, 6.11a, and 6.12a. All three samples are single-phase spinels. The Zn 0 and Zn 0.5 samples could be indexed with the $I4_1/amd$ space group of the tetragonal spinel. They form tetragonal spinels because the average Mn oxidation state is below 3.5+ for each sample. The Zn 1 sample, however, has an average Mn oxidation state of 4+, and it, therefore, possesses the cubic spinel structure with the $Fd\bar{3}m$ space group. Zn spinels form as normal spinels, so there is no cation mixing between the Zn and Mn/Ni ions.[247] This is due to the strong preference of the Zn^{2+}:$3d^{10}$ configuration for tetrahedral coordination.[262]

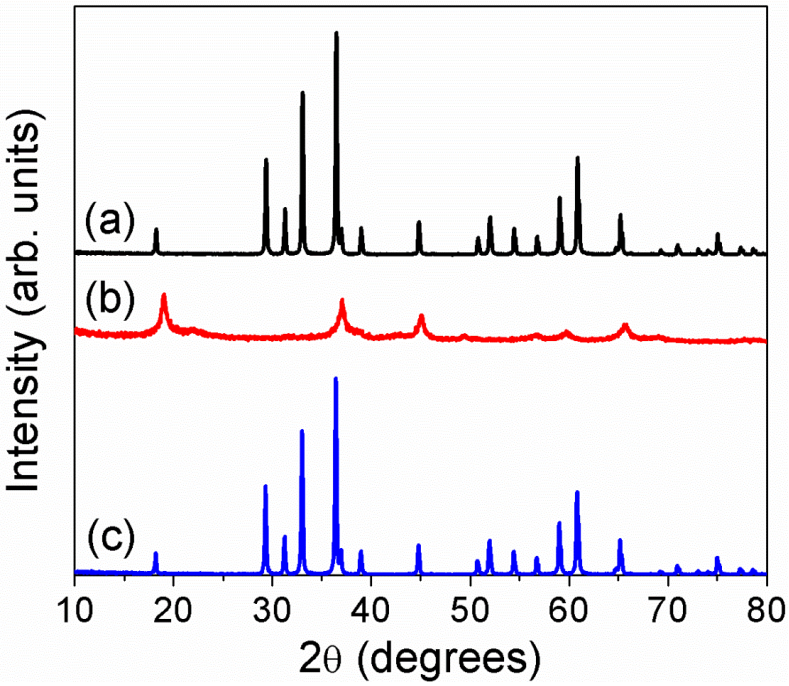

Figure 6.10. XRD patterns of $ZnMn_2O_4$ at various stages: (a) starting material, (b) after acid treatment, and (c) after chemical treatment.

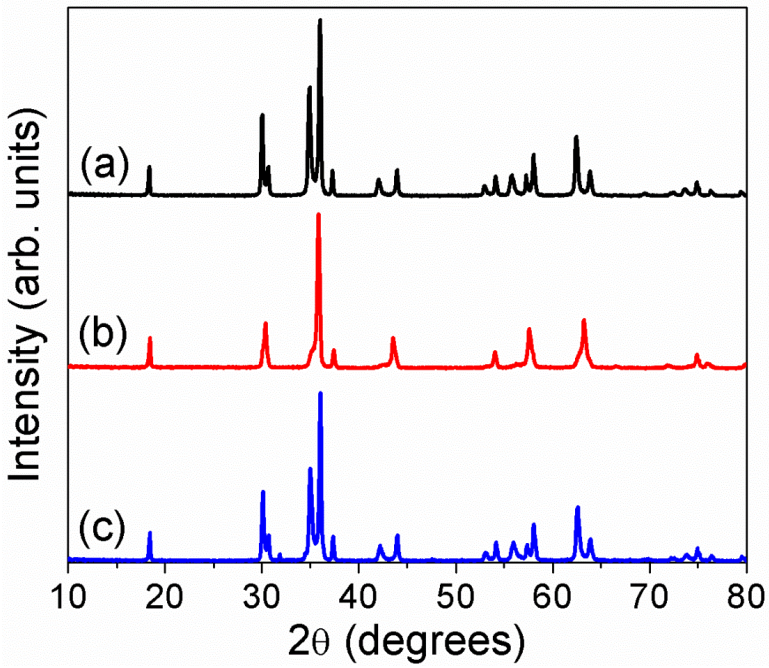

Figure 6.11. XRD patterns of $ZnMn_{1.5}Ni_{0.5}O_4$ at various stages: (a) starting material, (b) after acid treatment, and (c) after chemical treatment.

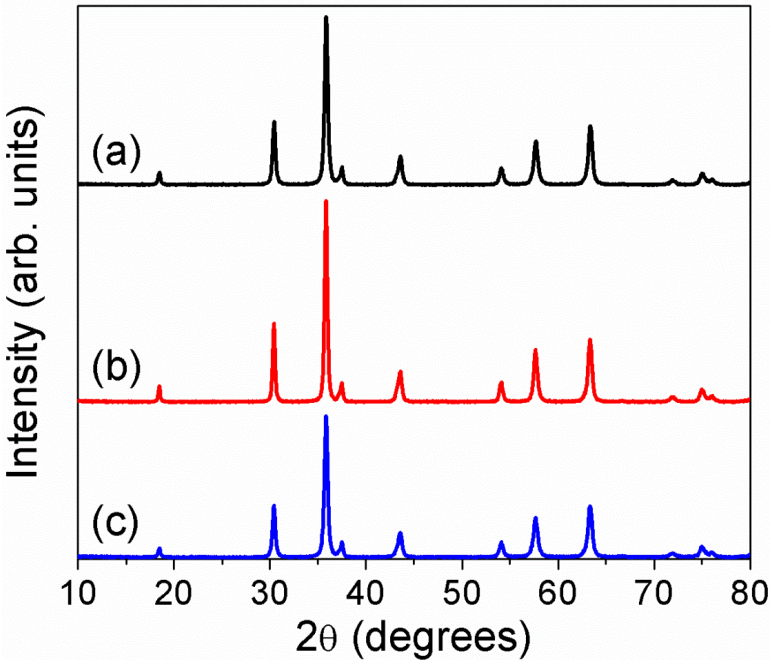

Figure 6.12. XRD patterns of $ZnMnNiO_4$ at various stages: (a) starting material, (b) after acid treatment, and (c) after chemical treatment.

The XRD patterns of the samples after acid treatment are shown in Figures 6.10b, 6.11b, and 6.12b. As expected, the acid treated Zn 0 sample shows a significant change in the XRD pattern, as all of the Zn is expected to be extracted, and its XRD pattern matches that of the cubic λ-MnO_2 sample.[2] Similarly, the acid-treated Zn 0.5 sample also exhibits a large change: the structure has converted from a tetragonal starting material to a final cubic spinel structure as the oxidation state of Mn has increased to 4+ in the acid-treated sample. In contrast, the Zn 1 sample remains essentially the same before and after the acid treatment, as the starting Zn 1 sample has all Mn as Mn^{4+} and does not lose any Zn from the lattice.

The ICP results of the acid-treated samples are given in Table 6.2. After a single acid treatment, the compositions were not as expected. The Zn 1 sample did not lose any Zn as expected, but there was still a significant amount of Zn ions left in the Zn 0 sample, and the Zn 0.5 sample had not lost as much Zn as it should by following Hunter's mechanism. This was unexpected because the acid treatment mechanism occurs very rapidly in Li-based spinel samples. For example, our previous study on $LiMn_2O_4$-based spinels required only a single acid treatment.[245] An additional acid treatment was carried out on the Zn 0 and Zn 0.5 samples after washing the samples obtained after the first acid treatment to see if more Zn could be extracted. Because the Zn 1 sample did not lose any Zn, further acid treatment was deemed unnecessary. After the second acid treatment, the compositions of the acid-treated Zn 0 and Zn 0.5 samples closely match the compositions

expected based on Hunter's mechanism. The Zn 0 sample lost nearly all of its Zn ions, while the Zn 0.5 sample displayed partial Zn extraction (0.70 Zn remaining), which very closely matched the calculated compositions. This verifies that the Mn^{3+} disproportionation reactions given in Reactions 6.6 and 6.7 are followed in Zn spinels. The fact that a second acid treatment was required to complete the extraction of the expected amount of Zn^{2+} ions suggests that the diffusion of Zn^{2+} ions is much slower through the spinel structure than Li^{+}-ion diffusion. This is most likely due to the increased electrostatic repulsion felt by the divalent Zn^{2+} ions with their neighboring Zn^{2+} ions while diffusing through the empty 16c octahedral sites. This topic will be discussed in greater detail in the next section.

Table 6.2. Theoretical and experimental Zn content after acid treatment and after chemical treatment of the various $ZnMn_{2-x}Ni_xO_4$ samples

Sample	Expected Composition After Acid Treatment	Zn Content After 1st Acid Treatment	Actual Composition After Two Acid Treatments	Composition After Chemical Treatment
Zn 0	Mn_2O_4	0.19	$Zn_{0.04}Mn_2O_4$	$Zn_{0.99}Mn_2O_4$
Zn 0.5	$Zn_{0.67}Mn_{1.33}Ni_{0.67}O_4$	0.82	$Zn_{0.70}Mn_{1.33}Ni_{0.66}O_4$	$Zn_{0.96}Mn_{1.50}Ni_{0.50}O_4$
Zn 1	$ZnMnNiO_4$	0.98	--	$Zn_{0.99}Mn_{1.00}Ni_{0.99}O_4$

Because the compositions so closely match their expected values, the results also confirm that the disproportionation of Mn^{3+} into Mn^{4+} and Mn^{2+} is the only mechanism involved in the extraction of Zn from these spinel samples. An exchange of Zn^{2+} ions by H^+ ions could be another possible mechanism for Zn extraction. However, we have previously shown in Chapter 5 that protons do not exchange with ions in the tetrahedral sites of the spinel structure, as they are not stable in the tetrahedral site.[245] This further confirms that there are no Zn ions in the octahedral sites of these materials because we earlier saw that an exchange of Mg^{2+} by H^+ occurs when Mg^{2+} ions are located in the octahedral sites. Also, if an exchange of Zn^{2+} ions by H^+ ions occurs, then the Zn 1 sample should have lost some Zn, but that is not the case. We attempted to gain further understanding of this topic by preparing a sample with Zn^{2+} ions located in the octahedral sites, *viz.*, $Zn_{1.1}Mn_{1.9}O_4$, but the synthesis of $Zn_xMn_{3-x}O_4$ ($x > 1$) unfortunately results in the formation of an impurity phase of either ZnO, another tetragonal spinel, or a cubic spinel.[263]

6.3.6. Chemical Treatment of $ZnMn_{2-x}Ni_xO_4$

The three samples were also chemically treated with NO_2BF_4 in hopes of extracting Zn from the structure. This process is very facile in $LiMn_2O_4$.[198] However, we saw earlier that it does not occur in Mg-based spinels. Reaction 6.9 displays the chemical process that could be anticipated to occur in $ZnMn_2O_4$ as a reference:

$$ZnMn_2^{3+}O_4 + xNO_2BF_4 \rightarrow Zn_{1-0.5x}Mn_2^{\geq 3+}O_4 + xNO_2 + 0.5xZn[BF_4]_2 \quad (6.9)$$

As mentioned previously, the XRD patterns of the starting materials are shown in Figures 6.10a, 6.11a, and 6.12a. The patterns of the chemically treated samples are shown in Figures 6.10c, 6.11c, and 6.12c. It is clear that the patterns of the chemically treated samples are essentially the same as the starting materials, except for a slight peak intensity decrease. This signifies that no Zn was extracted from the samples. The chemically treated Zn 0.5 sample did show two new small peaks, however, which are attributed to (Zn/Mn/Ni)O. It is unclear why this small impurity was formed. The ICP results of the chemically-treated samples are given in Table 6.2, which confirm that essentially no Zn was extracted from the samples. Zn 0 and Zn 1 only lost 0.01 Zn, while Zn 0.5 lost slightly more at 0.04 Zn, but this is nearly a negligible loss when experimental error is taken into account.

The results obtained from the Zn-based spinel system are clearly very different from those expected based on the acid-treatment mechanism and those found with the Li-based spinels, but they are similar to those found in Mg-spinels. Because NO_2BF_4 easily extracts Li from $LiMn_2O_4$, one would expect the same behavior in $ZnMn_2O_4$ and other similar compounds. In tetrahedral sites, both Li^+ (0.59 Å) and Zn^{2+} (0.60 Å) ions have

very similar ionic radii, so size effects cannot explain the differences in the extraction behavior. The major difference between the two ions is their charge. Zn^{2+} ions would experience greater electrostatic repulsion than Li^{+} ions, which is the most likely the reason for the difference between the Li-based and Zn-based systems. When Zn^{2+} ions diffuse out of the spinel structure, they migrate through an empty 16c octahedral site in order to hop from one 8a tetrahedral site to another 8a tetrahedral site. When the Zn^{2+} ions are in the 16c octahedral sites, they feel electrostatic repulsion from another Zn^{2+} ion in the neighboring 8a tetrahedral site. With a higher charge in Zn^{2+} compared to that in Li^{+}, the electrostatic repulsion between two Zn^{2+} ions in neighboring 8a tetrahedral and 16c octahedral sites is dramatically increased, which leads a large energetic barrier for Zn-ion diffusion and a blocking of the extraction of Zn from the structure.

An interesting point is that a similar diffusion of Zn^{2+} ions from one 8a tetrahedral site to another via the neighboring 16c site needs to occur during acid treatment as well. However, acid treatment results in the extraction of the right amount of Zn as one would expect based on Hunter's mechanism. We need to understand why. Acid extraction proceeds by a more complicated mechanism due to the disproportionation of Mn^{3+} ions and dissolution of resulting Mn^{2+} ions. Because Mn^{2+} ions are being lost from the lattice, some 16d octahedral-site vacancies are being formed as Mn ions migrate to the surface during acid treatment. These additional vacancies most likely allow for new Zn-ion migration pathways with reduced energy barriers, which facilitate the Zn^{2+} ions to be extracted from the structure.

We found exactly the same behavior in Mg-based spinels as well. Acid treatment was able to extract Mg ions from the spinel structure according to Hunter's mechanism, and an exchange of Mg^{2+} ions by H^{+} ions occurs if Mg^{2+} ions are present in octahedral sites. Because another divalent ion exhibits the same extraction properties, it further strengthens the argument that increased electrostatic repulsion is responsible for the failure of chemical extraction of Zn from the spinel lattice. The difficulty of extracting divalent ions from the spinel structure appears to only occur, however, in the ideal spinel structure. If the spinel structure has cation vacancies, either through explicit synthesis or post-synthesis processing, then divalent ions are able to move through the spinel structure to some extent.[237, 264] These findings lead us to conclude that the ideal spinel structure is not viable as a cathode for Zn-ion batteries due to the blockage of Zn-ion diffusion. However, if chemical treatment or appropriate synthesis methods are used to create cation vacancies in the structure, then spinels could become amenable to divalent cations like Mg^{2+} or Zn^{2+}, but only to a limited extent and with limited capacity.

6.4. CONCLUSIONS

Battery systems using multivalent cations, such as Mg^{2+} and Zn^{2+}, are being pursued as next-generation batteries, but there are several hurdles to overcome in developing multivalent ion batteries, including finding a suitable cathode host that can reversibly insert/extract Mg^{2+}/Zn^{2+} ions. We studied the possibility of Mg/Zn extraction in some spinel materials, employing both acid (H_2SO_4) and chemical (NO_2BF_4) treatments analogous to those employed with lithium-containing spinels such as

$LiMn_2O_4$. The samples investigated were $Mg_{1+x}Mn_{2-x}O_4$ (x = 0, 0.1, and 0.5), $MgMnAlO_4$, and $ZnMn_{2-x}Ni_xO_4$ (x = 0, 0.5, 1). It was found that acid treatment can fully extract Mg from $MgMn_2O_4$, following Hunter's mechanism[2] involving the disproportionation of Mn^{3+} and dissolution of Mn^{2+} from the lattice. The rate of Mg extraction varies linearly with the amount of cation disorder between the octahedral and tetrahedral sites, which can be altered by the heating protocol. Increasing the cation disorder decreases the rate of Mg extraction. Acid treatment can fully extract Mg from $Mg_{1.1}Mn_{1.9}O_4$ and nearly extracts all of the Mg from $Mg_{1.5}Mn_{1.5}O_4$. With only Hunter's mechanism, these compounds should have significant Mg content remaining after acid treatment, but they also experience an ion exchange of Mg^{2+} by H^+ that only happens to Mg^{2+} ions in the octahedral sites; such an ion exchange does not occur with tetrahedral sites as H^+ ions are not stable in the tetrahedral sites of the spinel lattice.[28] This mechanism is slower than the process involving Mn^{3+} disproportionation and Mn dissolution, which is why increasing cation disorder decreases the Mg extraction rate. $MgMnAlO_4$, however, does not experience Mg extraction with acid treatment because the Al^{3+} ions disrupt the Mn-Mn interaction and impede electron transfer/hopping. Chemical treatment with NO_2BF_4 was not able to extract any Mg from $MgMn_2O_4$ and $Mg_{1.5}Mn_{1.5}O_4$, unlike in the analogous $LiMn_2O_4$ spinel. This is most likely due to the increased repulsion felt by the higher valence Mg^{2+} ions by diffusing from one 8a tetrahedral site to another through the neighboring 16c octahedral sites. The difference between the acid treatment and the chemical treatment with NO_2BF_4 behaviors is due to the Mn dissolution that occurs during the acid treatment. The migration and removal of

Mn ions during acid treatment lead to the Mg^{2+} ions experiencing less of an energy barrier for migration.

Acid treatment was able to extract Zn from the spinel lattice quantitatively following Hunter's mechanism involving the disproportionation of Mn^{3+} into Mn^{4+} and Mn^{2+}.[2] No additional Zn extraction via ion-exchange reaction was found to occur. In contrast, chemical treatment with NO_2BF_4 was unable to extract any appreciable amount of Zn from the spinel lattice, unlike with the Li analog $LiMn_2O_4$. Similar to Mg-spinels, this is believed to be due to the large electrostatic repulsion felt by the Zn^{2+} ions while diffusing through the lattice. Because the Mg^{2+} and Zn^{2+} ions are not able to easily diffuse from the 8a tetrahedral sites to the neighboring 16c octahedral sites during chemical treatment with NO_2BF_4, the spinel structure may not be a suitable option for Mg-ion or Zn-ion battery cathodes, unless it is altered structurally to increase divalent cation migration, as shown in other reports.[237, 244]

Chapter 7: Summary

With an aim to develop advanced battery materials, the electrochemical properties and ion-extraction mechanisms of Li-rich layered oxides and spinel oxides were studied. Transition-metal doping of Li-rich layered oxides was used to explore the complex first charge-discharge mechanism and mitigate voltage decay. The Li, Mg, and Zn ion extraction mechanisms from spinel oxides were investigated to gain insight into designing new battery cathodes.

First, the effect of substituting Ru^{4+} ions for Mn^{4+} ions on the first charge-discharge cycle of Li-rich layered oxides was investigated. As the amount of Ru doping increases, the materials exhibit the monoclinic *P12/m* structure, which provides some evidence of Ru-Ru dimer formation. Although the substitution of Ru was expected to increase the performance due to the electroactive $Ru^{4+/5+}$ couple and its higher degree of covalent bonding with the oxide-ion framework, the electroactive Ru does increase the sloping region length, but the plateau region suffers from a dramatic decrease in length with increasing doping which may be due to the increase in particle size and the formation of Ru-Ru dimers. The Ru-Ru dimers raise the $Ru^{4+/5+}$:4d band relative to the top of the O:2p band and consequently decrease the metal-oxygen covalence and oxygen loss plateau length. The relative positions of these bands play a key role in controlling the complex electrochemical properties of lithium-rich layered oxides.

Next, the effect of Ni oxidation state on the properties of Li-rich layered oxides was examined. Increasing the Ni oxidation state had several effects. The smaller Ni^{3+} ions decreases the amount of Li/Ni site mixing, which enhances Li-ion diffusion and

impede the layered-to-spinel transformation that causes the voltage decay process. The oxygen loss plateau decreases with increasing Ni oxidation state due to the reduction in the Li_2MnO_3 character of the material from the decreased Mn content and the reduction of Li ions in the TM layer. The first cycle irreversible capacity loss increases due to Ni^{3+} ions forming an inactive domain. Overall, the discharge capacity decreases with increasing Ni oxidation state. The decrease in the Mn^{3+} ion formation reduces Mn dissolution into the electrolyte, which increases cyclability, and impedes the layered-to-spinel phase transformation by reducing the amount of Mn disproportionation that occurs. Increasing the Ni oxidation state dramatically reduces the voltage decay and improves the cyclability, but the downside is a decrease in discharge capacity also occurs.

Then, the acid delithiation mechanism in doped Li-spinels was investigated. XRD and compositional analysis data establish that the lithium extraction occurs by a disproportionation of Mn^{3+} ions into Mn^{4+} and Mn^{2+} ions, with the latter being leached out into the solution. The amount of lithium extracted is proportional to the amount of Mn^{3+} in the initial samples. Other M^{3+} (M = Cr, Fe, and Co) ions do not disproportionate into M^{4+} and M^{2+} ions, unlike the Mn^{3+} ions. Moreover, ion exchange of Li^+ ions by H^+ ions does not occur as the H^+ ions may not be stabilized in tetrahedral sites of the spinel framework.

Finally, the Mg and Zn extraction mechanisms from some spinel materials were studied employing both acid and chemical treatments. It was found that acid treatment can fully extract Mg from $MgMn_2O_4$, through a disproportionation of Mn^{3+} and dissolution of Mn^{2+} from the lattice. The rate of Mg extraction decreases linearly with an

increasing amount of cation disorder between the octahedral and tetrahedral sites. Acid treatment can fully extract Mg from $Mg_{1.1}Mn_{1.9}O_4$ and nearly extracts all of the Mg from $Mg_{1.5}Mn_{1.5}O_4$. These compounds, in addition to Mn dissolution, experience an ion exchange of Mg^{2+} by H^+ that only happens to Mg^{2+} ions in the octahedral sites. This mechanism is slower than Mn disproportionation, which is why increasing cation disorder decreases the Mg extraction rate. $MgMnAlO_4$, however, does not experience Mg extraction with acid treatment because the Al^{3+} ions disrupt the Mn-Mn interaction and impede electron transfer/hopping.

Unexpectedly, chemical treatment was not able to extract any Mg from the materials. This is likely due to the repulsion felt by the Mg^{2+} ions diffusing from one tetrahedral site to another through a neighboring octahedral site. The difference between the acid and chemical treatment behaviors is due to the Mn dissolution that occurs during the acid treatment. The migration and removal of Mn ions during acid treatment lead to the Mg^{2+} ions experiencing less of an energy barrier for migration. Acid treatment was able to extract Zn from the spinel lattice with the same Mn disproportionation reaction as in Mg-spinels. No additional Zn extraction via ion exchange reaction was found to occur. In contrast, chemical treatment was unable to extract any appreciable amount of Zn from the spinel lattice. Similar to Mg-spinels, this is believed to be due to the electrostatic repulsion felt by the Zn^{2+} ions while diffusing through the lattice. Because Mg^{2+} and Zn^{2+} ions are not able to easily diffuse through the spinel structure, it may not be a suitable option for Mg-ion or Zn-ion battery cathodes, unless it is altered structurally to increase divalent cation migration.

Overall, the findings in this dissertation bring new insights towards (i) understanding the complex structural and electrochemical behaviors of lithium-rich layered oxides and (ii) whether or not spinel hosts could be employed for reversible divalent cation insertion/extraction. The understanding gained with the variation of Ni oxidation state could be utilized to think of potential future approaches to overcome the persistent problem of voltage decay in lithium-rich layered oxides. The findings with the Li, Mg, and Zn extraction reactions in spinel oxide hosts could serve as a guide in designing future hosts for battery chemistries based on multivalent cations.

References

1. M. H. Rossouw, D. C. Liles and M. M. Thackeray, *Journal of Solid State Chemistry*, 1993, **104**, 464-466.
2. J. C. Hunter, *Journal of Solid State Chemistry*, 1981, **39**, 142-147.
3. P. Kalyani, S. Chitra, T. Mohan and S. Gopukumar, *Journal of Power Sources*, 1999, **80**, 103-106.
4. Z. Lu, D. D. MacNeil and J. R. Dahn, *Electrochemical and Solid-State Letters*, 2001, **4**, A191.
5. Z. Lu, L. Y. Beaulieu, R. A. Donaberger, C. L. Thomas and J. R. Dahn, *Journal of The Electrochemical Society*, 2002, **149**, A778.
6. Z. Lu and J. R. Dahn, *Journal of The Electrochemical Society*, 2002, **149**, A815.
7. H. Yu, H. Kim, Y. Wang, P. He, D. Asakura, Y. Nakamura and H. Zhou, *Physical chemistry chemical physics : PCCP*, 2012, **14**, 6584-6595.
8. B. Song, M. O. Lai and L. Lu, *Electrochimica Acta*, 2012, **80**, 187-195.
9. H. Yu, Y. Ishikawa, Y. G. So, N. Shibata, T. Kudo, H. Zhou and Y. Ikuhara, *Angewandte Chemie*, 2013, **52**, 5969-5973.
10. K. A. Jarvis, C.-C. Wang, A. Manthiram and P. J. Ferreira, *Journal of Materials Chemistry A*, 2014, **2**, 1353-1362.
11. C.-C. Wang and A. Manthiram, *Journal of Materials Chemistry A*, 2013, **1**, 10209-10217.
12. Z. Lu, Z. Chen and J. R. Dahn, *Chemistry of Materials*, 2003, **15**, 3214-3220.
13. K. A. Jarvis, Z. Deng, L. F. Allard, A. Manthiram and P. J. Ferreira, *Chemistry of Materials*, 2011, **23**, 3614-3621.
14. B. Ammundsen, J. Paulsen, I. Davidson, R.-S. Liu, C.-H. Shen, J.-M. Chen, L.-Y. Jang and J.-F. Lee, *Journal of The Electrochemical Society*, 2002, **149**, A431.
15. C. Genevois, H. Koga, L. Croguennec, M. Ménétrier, C. Delmas and F. Weill, *The Journal of Physical Chemistry C*, 2015, **119**, 75-83.
16. H. Koga, L. Croguennec, P. Mannessiez, M. Ménétrier, F. Weill, L. Bourgeois, M. Duttine, E. Suard and C. Delmas, *The Journal of Physical Chemistry C*, 2012, **116**, 13497-13506.
17. J. Kikkawa, T. Akita, M. Tabuchi, M. Shikano, K. Tatsumi and M. Kohyama, *Journal of Applied Physics*, 2008, **103**, 104911.
18. J. Bareno, C. H. Lei, J. G. Wen, S. H. Kang, I. Petrov and D. P. Abraham, *Advanced Materials*, 2010, **22**, 1122-1127.
19. J. Bareño, M. Balasubramanian, S. H. Kang, J. G. Wen, C. H. Lei, S. V. Pol, I. Petrov and D. P. Abraham, *Chemistry of Materials*, 2011, **23**, 2039-2050.
20. M. Gu, I. Belharouak, A. Genc, Z. Wang, D. Wang, K. Amine, F. Gao, G. Zhou, S. Thevuthasan, D. R. Baer, J. G. Zhang, N. D. Browning, J. Liu and C. Wang, *Nano letters*, 2012, **12**, 5186-5191.
21. J. Shojan, V. R. Chitturi, J. Soler, O. Resto, W. C. West and R. S. Katiyar, *Journal of Power Sources*, 2015, **274**, 440-450.

22. J. Kikkawa, T. Akita, M. Tabuchi, M. Shikano, K. Tatsumi and M. Kohyama, *Applied Physics Letters*, 2007, **91**, 054103-054103-054103.
23. M. M. Thackeray, C. S. Johnson, J. T. Vaughey, N. Li and S. A. Hackney, *Journal of Materials Chemistry*, 2005, **15**, 2257-2267.
24. S.-H. Yu, T. Yoon, J. Mun, S. Park, Y.-S. Kang, J.-H. Park, S. M. Oh and Y.-E. Sung, *Journal of Materials Chemistry A*, 2013, **1**, 2833.
25. J. Kikkawa, T. Akita, M. Tabuchi, M. Shikano, K. Tatsumi and M. Kohyama, *Electrochemical and Solid-State Letters*, 2008, **11**, A183.
26. C.-C. Wang, K. A. Jarvis, P. J. Ferreira and A. Manthiram, *Chemistry of Materials*, 2013, **25**, 3267-3275.
27. E. McCalla, A. W. Rowe, R. Shunmugasundaram and J. R. Dahn, *Chemistry of Materials*, 2013, **25**, 989-999.
28. E. McCalla, C. M. Lowartz, C. R. Brown and J. R. Dahn, *Chemistry of Materials*, 2013, **25**, 912-918.
29. E. McCalla, A. W. Rowe, C. R. Brown, L. R. P. Hacquebard and J. R. Dahn, *Journal of the Electrochemical Society*, 2013, **160**, A1134-A1138.
30. E. McCalla, J. Li, A. W. Rowe and J. R. Dahn, *Journal of the Electrochemical Society*, 2014, **161**, A606-A613.
31. H. Koga, L. Croguennec, M. Menetrier, K. Douhil, S. Belin, L. Bourgeois, E. Suard, F. Weill and C. Delmas, *Journal of the Electrochemical Society*, 2013, **160**, A786-A792.
32. H. Koga, L. Croguennec, M. Ménétrier, P. Mannessiez, F. Weill and C. Delmas, *Journal of Power Sources*, 2013, **236**, 250-258.
33. M. Sathiya, K. Ramesha, G. Rousse, D. Foix, D. Gonbeau, A. S. Prakash, M. L. Doublet, K. Hemalatha and J. M. Tarascon, *Chemistry of Materials*, 2013, **25**, 1121-1131.
34. M. Sathiya, G. Rousse, K. Ramesha, C. P. Laisa, H. Vezin, M. T. Sougrati, M. L. Doublet, D. Foix, D. Gonbeau, W. Walker, A. S. Prakash, M. Ben Hassine, L. Dupont and J. M. Tarascon, *Nature Materials*, 2013, **12**, 827-835.
35. C. S. Johnson, N. Li, C. Lefief and M. M. Thackeray, *Electrochemistry Communications*, 2007, **9**, 787-795.
36. A. D. Robertson and P. G. Bruce, *Chemical communications*, 2002, DOI: 10.1039/b207945c, 2790-2791.
37. J. C. Knight, P. Nandakumar, W. H. Kan and A. Manthiram, *Journal of Materials Chemistry A*, 2015, **3**, 2006-2011.
38. X. Xiang, J. C. Knight, W. Li and A. Manthiram, *Journal of Physical Chemistry C*, 2014, **118**, 21826-21833.
39. Z. Q. Deng and A. Manthiram, *The Journal of Physical Chemistry C*, 2011, **115**, 7097-7103.
40. J. R. Croy, J. S. Park, F. Dogan, C. S. Johnson, B. Key and M. Balasubramanian, *Chemistry of Materials*, 2014, **26**, 7091-7098.

41. F. Dogan, J. R. Croy, M. Balasubramanian, M. D. Slater, H. Iddir, C. S. Johnson, J. T. Vaughey and B. Key, *Journal of the Electrochemical Society*, 2015, **162**, A235-A243.
42. A. R. Armstrong, M. Holzapfel, P. Novák, C. S. Johnson, S. H. Kang, M. M. Thackeray and P. G. Bruce, *Journal of American Chemical Society*, 2006, **128**, 8694-8698.
43. N. Yabuuchi, K. Yoshii, S. T. Myung, I. Nakai and S. Komaba, *Journal of the American Chemical Society*, 2011, **133**, 4404-4419.
44. H. Koga, L. Croguennec, M. Ménétrier, P. Mannessiez, F. Weill, C. Delmas and S. Belin, *The Journal of Physical Chemistry C*, 2014, **118**, 5700-5709.
45. E. Salager, V. Sarou-Kanian, M. Sathiya, M. Tang, J.-B. Leriche, P. Melin, Z. Wang, H. Vezin, C. Bessada, M. Deschamps and J.-M. Tarascon, *Chemistry of Materials*, 2014, **26**, 7009-7019.
46. M. Sathiya, A. M. Abakumov, D. Foix, G. Rousse, K. Ramesha, M. Saubanere, M. L. Doublet, H. Vezin, C. P. Laisa, A. S. Prakash, D. Gonbeau, G. VanTendeloo and J. M. Tarascon, *Nature Materials*, 2015, **14**, 230-238.
47. P. Yan, A. Nie, J. Zheng, Y. Zhou, D. Lu, X. Zhang, R. Xu, I. Belharouak, X. Zu, J. Xiao, K. Amine, J. Liu, F. Gao, R. Shahbazian-Yassar, J. G. Zhang and C. M. Wang, *Nano letters*, 2015, **15**, 514-522.
48. F. Yang, Y. Liu, S. K. Martha, Z. Wu, J. C. Andrews, G. E. Ice, P. Pianetta and J. Nanda, *Nano letters*, 2014, **14**, 4334-4341.
49. M. Gu, I. Belharouak, J. Zheng, H. Wu, J. Xiao, A. Genc, K. Amine, S. Thevuthasan, D. R. Baer, J.-G. Zhang, N. D. Browning, J. Liu and C. Wang, *ACS Nano*, 2013, **7**, 760-767.
50. Y. Li, M. Bettge, B. Polzin, Y. Zhu, M. Balasubramanian and D. P. Abraham, *Journal of the Electrochemical Society*, 2013, **160**, A3006-A3019.
51. C. R. Fell, K. J. Carroll, M. Chi and Y. S. Meng, *Journal of The Electrochemical Society*, 2010, **157**, A1202.
52. B. Song, Z. Liu, M. O. Lai and L. Lu, *Physical chemistry chemical physics : PCCP*, 2012, **14**, 12875-12883.
53. A. Boulineau, L. Simonin, J.-F. Colin, E. Canévet, L. Daniel and S. Patoux, *Chemistry of Materials*, 2012, **24**, 3558-3566.
54. S. Hy, W.-N. Su, J.-M. Chen and B.-J. Hwang, *The Journal of Physical Chemistry C*, 2012, **116**, 25242-25247.
55. S. H. Kang, P. Kempgens, S. Greenbaum, A. J. Kropf, K. Amine and M. M. Thackeray, *Journal of Materials Chemistry*, 2007, **17**, 2069.
56. J. R. Croy, K. G. Gallagher, M. Balasubramanian, Z. Chen, Y. Ren, D. Kim, S.-H. Kang, D. W. Dees and M. M. Thackeray, *The Journal of Physical Chemistry C*, 2013, **117**, 6525-6536.
57. B. Xu, C. R. Fell, M. Chi and Y. S. Meng, *Energy & Environmental Science*, 2011, **4**, 2223-2233.
58. D. Mohanty, J. Li, D. P. Abraham, A. Huq, E. A. Payzant, D. L. Wood and C. Daniel, *Chemistry of Materials*, 2014, **26**, 6272-6280.

59. J. Zheng, M. Gu, A. Genc, J. Xiao, P. Xu, X. Chen, Z. Zhu, W. Zhao, L. Pullan, C. Wang and J. G. Zhang, *Nano letters*, 2014, **14**, 2628-2635.
60. E.-S. Lee and A. Manthiram, *Journal of Materials Chemistry A*, 2014, **2**, 3932-3939.
61. K. G. Gallagher, J. R. Croy, M. Balasubramanian, M. Bettge, D. P. Abraham, A. K. Burrell and M. M. Thackeray, *Electrochemistry Communications*, 2013, **33**, 96-98.
62. J. R. Croy, K. G. Gallagher, M. Balasubramanian, B. R. Long and M. M. Thackeray, *Journal of the Electrochemical Society*, 2014, **161**, A318-A325.
63. F. Dogan, B. R. Long, J. R. Croy, K. G. Gallagher, H. Iddir, J. T. Russell, M. Balasubramanian and B. Key, *Journal of the American Chemical Society*, 2015, **137**, 2328-2335.
64. D. Kim, G. Sandi, J. R. Croy, K. G. Gallagher, S. H. Kang, E. Lee, M. D. Slater, C. S. Johnson and M. M. Thackeray, *Journal of the Electrochemical Society*, 2013, **160**, A31-A38.
65. D. Kim, J. R. Croy and M. M. Thackeray, *Electrochemistry Communications*, 2013, **36**, 103-106.
66. A. Vu, L. K. Walker, J. Bareño, A. K. Burrell and I. Bloom, *Journal of Power Sources*, 2015, **280**, 155-158.
67. Y. Li, J. Bareno, M. Bettge and D. P. Abraham, *Journal of the Electrochemical Society*, 2015, **162**, A155-A161.
68. M. Bettge, Y. Li, K. Gallagher, Y. Zhu, Q. Wu, W. Lu, I. Bloom and D. P. Abraham, *Journal of the Electrochemical Society*, 2013, **160**, A2046-A2055.
69. B. Song, C. Zhou, H. Wang, H. Liu, Z. Liu, M. O. Lai and L. Lu, *Journal of the Electrochemical Society*, 2014, **161**, A1723-A1730.
70. M. N. Ates, Q. Jia, A. Shah, A. Busnaina, S. Mukerjee and K. M. Abraham, *Journal of the Electrochemical Society*, 2014, **161**, A290-A301.
71. Q. Li, G. Li, C. Fu, D. Luo, J. Fan and L. Li, *ACS applied materials & interfaces*, 2014, **6**, 10330-10341.
72. M. N. Ates, S. Mukerjee and K. M. Abraham, *Journal of the Electrochemical Society*, 2014, **161**, A355-A363.
73. J. Zheng, M. Gu, J. Xiao, B. J. Polzin, P. Yan, X. Chen, C. Wang and J.-G. Zhang, *Chemistry of Materials*, 2014, **26**, 6320-6327.
74. I. Bloom, L. Trahey, A. Abouimrane, I. Belharouak, X. Zhang, Q. Wu, W. Lu, D. P. Abraham, M. Bettge, J. W. Elam, X. Meng, A. K. Burrell, C. Ban, R. Tenent, J. Nanda and N. Dudney, *Journal of Power Sources*, 2014, **249**, 509-514.
75. B. R. Long, J. R. Croy, J. S. Park, J. Wen, D. J. Miller and M. M. Thackeray, *Journal of the Electrochemical Society*, 2014, **161**, A2160-A2167.
76. X. Feng, Z. Yang, D. Tang, Q. Kong, L. Gu, Z. Wang and L. Chen, *Physical Chemistry Chemical Physics*, 2015, **17**, 1257-1264.
77. E.-S. Lee, A. Huq and A. Manthiram, *Journal of Power Sources*, 2013, **240**, 193-203.
78. J. Yan, X. Liu and B. Li, *RSC Advances*, 2014, **4**, 63268-63284.

79. X. Yu, Y. Lyu, L. Gu, H. Wu, S.-M. Bak, Y. Zhou, K. Amine, S. N. Ehrlich, H. Li, K.-W. Nam and X.-Q. Yang, *Advanced Energy Materials*, 2014, **4**.
80. H. Liu, C. Chen, C. Du, X. He, G. Yin, B. Song, P. Zuo, X. Cheng, Y. Ma and Y. Gao, *Journal of Materials Chemistry A*, 2015, **3**, 2634-2641.
81. J. Lee and W. Choi, *Journal of the Electrochemical Society*, 2015, **162**, A743-A748.
82. H. Zhuo, Y. Zhang, D. Wang, C. He, C. Zhu, Q. Zhang, C. Li, L. Sun, J. Liu and S. Chen, *Electrochimica Acta*, 2014, **149**, 42-48.
83. Q. Xue, J. Li, G. Xu, H. Zhou, X. Wang and F. Kang, *Journal of Materials Chemistry A*, 2014, **2**, 18613-18623.
84. B. Song, C. Zhou, Y. Chen, Z. Liu, M. O. Lai, J. Xue and L. Lu, *RSC Advances*, 2014, **4**, 44244-44252.
85. J. Mun, J.-H. Park, W. Choi, A. Benayad, J.-H. Park, J.-M. Lee, S.-G. Doo and S. M. Oh, *Journal of Materials Chemistry A*, 2014, **2**, 19670-19677.
86. I. T. Kim, J. C. Knight, H. Celio and A. Manthiram, *Journal of Materials Chemistry A*, 2014, **2**, 8696.
87. Y. Liu, Y. Gao, J. Lv and L. Chen, *Materials Research Bulletin*, 2013, DOI: 10.1016/j.materresbull.2013.07.024.
88. B. Li, Y. Yu and J. Zhao, *Journal of Power Sources*, 2015, **275**, 64-72.
89. F. He, X. Wang, C. Du, A. P. Baker, J. Wu and X. Zhang, *Electrochimica Acta*, 2015, **153**, 484-491.
90. H. Meng, H. Jin, J. Gao, L. Zhang and Q. Xu, *Journal of the Electrochemical Society*, 2014, **161**, A1564-A1571.
91. S. X. Liao, C. H. Shen, Y. J. Zhong, W. H. Yan, X. X. Shi, S. S. Pei, X. Guo, Z. B. He, X. L. Wang and H. Liu, *RSC Advances*, 2014, **4**, 56273-56278.
92. Y. Zhao, C. Zhao, H. Feng, Z. Sun and D. Xia, *Electrochemical and Solid-State Letters*, 2011, **14**, A1.
93. Q. Y. Wang, J. Liu, A. V. Murugan and A. Manthiram, *Journal of Materials Chemistry*, 2009, **19**, 4965.
94. Y. Wu and A. Manthiram, *Electrochemical and Solid-State Letters*, 2006, **9**, A221.
95. J. Ma, B. Li, L. An, H. Wei, X. Wang, P. Yu and D. Xia, *Journal of Power Sources*, 2015, **277**, 393-402.
96. J. J. Chen, Z. D. Li, H. F. Xiang, W. W. Wu, S. Cheng, L. J. Zhang, Q. S. Wang and Y. C. Wu, *RSC Advances*, 2015, **5**, 3031-3038.
97. Y. Liu, X. Huang, Q. Qiao, Y. Wang, S. Ye and X. Gao, *Electrochimica Acta*, 2014, **147**, 696-703.
98. S.-H. Kang and M. M. Thackeray, *Electrochemistry Communications*, 2009, **11**, 748-751.
99. S. H. Lee, B. K. Koo, J.-C. Kim and K. M. Kim, *Journal of Power Sources*, 2008, **184**, 276-283.
100. F. Amalraj, M. Talianker, B. Markovsky, L. Burlaka, N. Leifer, G. Goobes, E. M. Erickson, O. Haik, J. Grinblat, E. Zinigrad, D. Aurbach, J. K. Lampert, J. Y. Shin,

M. Schulz-Dobrick and A. Garsuch, *Journal of the Electrochemical Society*, 2013, **160**, A2220-A2233.
101. J. M. Zheng, Z. R. Zhang, X. B. Wu, Z. X. Dong, Z. Zhu and Y. Yang, *Journal of The Electrochemical Society*, 2008, **155**, A775.
102. S. Han, B. Qiu, Z. Wei, Y. Xia and Z. Liu, *Journal of Power Sources*, 2014, **268**, 683-691.
103. B. Song, H. Liu, Z. Liu, P. Xiao, M. O. Lai and L. Lu, *Scientific reports*, 2013, **3**, 3094.
104. J. Zheng, S. Deng, Z. Shi, H. Xu, H. Xu, Y. Deng, Z. Zhang and G. Chen, *Journal of Power Sources*, 2013, **221**, 108-113.
105. D. Y. W. Yu, K. Yanagida and H. Nakamura, *Journal of The Electrochemical Society*, 2010, **157**, A1177.
106. E. S. Lee and A. Manthiram, *Journal of The Electrochemical Society*, 2011, **158**, A47.
107. Y.-S. Hong, Y. J. Park, K. S. Ryu, S. H. Chang and M. G. Kim, *Journal of Materials Chemistry*, 2004, **14**, 1424.
108. Y. Kim, Y. Hong, M. G. Kim and J. Cho, *Electrochemistry Communications*, 2007, **9**, 1041-1046.
109. M. G. Kim, M. Jo, Y. S. Hong and J. Cho, *Chemical communications*, 2009, DOI: 10.1039/b815378g, 218-220.
110. G. Z. Wei, X. Lu, F. S. Ke, L. Huang, J. T. Li, Z. X. Wang, Z. Y. Zhou and S. G. Sun, *Adv Mater*, 2010, **22**, 4364-4367.
111. X. Jin, Q. Xu, H. Liu, X. Yuan and Y. Xia, *Electrochimica Acta*, 2014, **136**, 19-26.
112. H. Xu, S. Deng and G. Chen, *Journal of Materials Chemistry A*, 2014, **2**, 15015-15021.
113. M. Iftekhar, N. E. Drewett, A. R. Armstrong, D. Hesp, F. Braga, S. Ahmed and L. J. Hardwick, *Journal of the Electrochemical Society*, 2014, **161**, A2109-A2116.
114. S. H. Kang and K. Amine, *Journal of Power Sources*, 2005, **146**, 654-657.
115. L. Croguennec, J. Bains, M. Ménétrier, A. Flambard, E. Bekaert, C. Jordy, P. Biensan and C. Delmas, *Journal of The Electrochemical Society*, 2009, **156**, A349.
116. M. Tabuchi, Y. Nabeshima, T. Takeuchi, H. Kageyama, K. Tatsumi, J. Akimoto, H. Shibuya and J. Imaizumi, *Journal of Power Sources*, 2011, **196**, 3611-3622.
117. L. F. Jiao, M. Zhang, H. T. Yuan, M. Zhao, J. Guo, W. Wang, X. D. Zhou and Y. M. Wang, *Journal of Power Sources*, 2007, **167**, 178-184.
118. J. H. Kim, C. W. Park and Y. K. Sun, *Solid State Ionics*, 2003, **164**, 43-49.
119. K. G. Gallagher, S.-H. Kang, S. U. Park and S. Y. Han, *Journal of Power Sources*, 2011, **196**, 9702-9707.
120. N. Tran, L. Croguennec, M. Menetrier, F. Weill, P. Biensan, C. Jordy and C. Delmas, *Chemistry of Materials*, 2008, **20**, 4815-4825.
121. Y. Wu, A. Vadivel Murugan and A. Manthiram, *Journal of The Electrochemical Society*, 2008, **155**, A635.

122. J. Gao, J. Kim and A. Manthiram, *Electrochemistry Communications*, 2009, **11**, 84-86.
123. J. Gao and A. Manthiram, *Journal of Power Sources*, 2009, **191**, 644-647.
124. Y. Wu and A. Manthiram, *Solid State Ionics*, 2009, **180**, 50-56.
125. S. H. Kang, C. S. Johnson, J. T. Vaughey, K. Amine and M. M. Thackeray, *Journal of The Electrochemical Society*, 2006, **153**, A1186.
126. H. Yu and H. Zhou, *Journal of Materials Chemistry*, 2012, **22**, 15507-15510.
127. A. van Bommel, L. J. Krause and J. R. Dahn, *Journal of The Electrochemical Society*, 2011, **158**, A731.
128. T. Ohzuku, M. Nagayama, K. Tsuji and K. Ariyoshi, *Journal of Materials Chemistry*, 2011, **21**, 10179.
129. B. Qiu, J. Wang, Y. Xia, Z. Wei, S. Han and Z. Liu, *Journal of Power Sources*, 2014, **268**, 517-521.
130. R. Shunmugasundaram, R. Senthil Arumugam and J. R. Dahn, *Chemistry of Materials*, 2015, **27**, 757-767.
131. J. Hong, H.-D. Lim, M. Lee, S.-W. Kim, H. Kim, S.-T. Oh, G.-C. Chung and K. Kang, *Chemistry of Materials*, 2012, **24**, 2692-2697.
132. R. Liu, J. Duay and S. B. Lee, *Chemical communications*, 2011, **47**, 1384-1404.
133. P. Oh, S. Myeong, W. Cho, M.-J. Lee, M. Ko, H. Y. Jeong and J. Cho, *Nano letters*, 2014, **14**, 5965-5972.
134. K. Nakahara, M. Tabuchi, S. Kuroshima, A. Toda, K. Tanimoto and K. Nakano, *Journal of the Electrochemical Society*, 2012, **159**, A1398-A1404.
135. A. Ito, D. Li, Y. Ohsawa and Y. Sato, *Journal of Power Sources*, 2008, **183**, 344-346.
136. A. Ito, D. Li, Y. Sato, M. Arao, M. Watanabe, M. Hatano, H. Horie and Y. Ohsawa, *Journal of Power Sources*, 2010, **195**, 567-573.
137. Y. Zhu, Y. Li and D. P. Abraham, *Journal of the Electrochemical Society*, 2014, **161**, A1580-A1585.
138. S. J. Lee, J. G. Han, I. Park, J. Song, J. Cho, J. S. Kim and N. S. Choi, *Journal of the Electrochemical Society*, 2014, **161**, A2012-A2019.
139. J. Zhang, J. Wang, J. Yang and Y. NuLi, *Electrochimica Acta*, 2014, **117**, 99-104.
140. D. V. Chernyshov, S. A. Krachkovskiy, A. V. Kapylou, I. A. Bolshakov, W. C. Shin and M. Ue, *Journal of the Electrochemical Society*, 2014, **161**, A633-A642.
141. Y. Zhu, Y. Li, M. Bettge and D. P. Abraham, *Electrochimica Acta*, 2013, **110**, 191-199.
142. Z. D. Li, Y. C. Zhang, H. F. Xiang, X. H. Ma, Q. F. Yuan, Q. S. Wang and C. H. Chen, *Journal of Power Sources*, 2013, **240**, 471-475.
143. Y.-S. Kang, T. Yoon, S. S. Lee, J. Mun, M. S. Park, J.-H. Park, S.-G. Doo, I.-Y. Song and S. M. Oh, *Electrochemistry Communications*, 2013, **27**, 26-28.
144. Y. Zhu, Y. Li, M. Bettge and D. P. Abraham, *Journal of the Electrochemical Society*, 2012, **159**, A2109-A2117.
145. Q. Wu, W. Lu, M. Miranda, T. K. Honaker-Schroeder, K. Y. Lakhsassi and D. Dees, *Electrochemistry Communications*, 2012, **24**, 78-81.

146. S. Tan, Z. Zhang, Y. Li, Y. Li, J. Zheng, Z. Zhou and Y. Yang, *Journal of the Electrochemical Society*, 2012, **160**, A285-A292.
147. L. Yang, T. Markmaitree and B. L. Lucht, *Journal of Power Sources*, 2011, **196**, 2251-2254.
148. X. Xiang, J. C. Knight, W. Li and A. Manthiram, *Journal of Physical Chemistry C*, 2014, **118**, 23553-23558.
149. W. Yan, H. Wen, Y. Chen, Y. Wang and Y. Liu, *Journal of Power Sources*, 2015, **277**, 76-83.
150. X. Yuan, Q.-j. Xu, C. Wang, X. Liu, H. Liu and Y. Xia, *Journal of Power Sources*, 2015, **279**, 157-164.
151. L. Zhang, N. Li, B. Wu, H. Xu, L. Wang, X. Q. Yang and F. Wu, *Nano letters*, 2015, **15**, 656-661.
152. M. Chen, X. Xiang, D. Chen, Y. Liao, Q. Huang and W. Li, *Journal of Power Sources*, 2015, **279**, 197-204.
153. X. Hou, X. Zou, Y. Huang, S. Hu, Q. Ru and Y. Gao, *RSC Advances*, 2014, **4**, 29534.
154. L. Zhang, W. Borong, L. Ning and W. Feng, *Electrochimica Acta*, 2014, **118**, 67-74.
155. J. Xiao, L. Wan, S. Yang, F. Xiao and S. Wang, *Nano letters*, 2014, **14**, 831-838.
156. L. Zhang, B. Wu, N. Li, D. Mu, C. Zhang and F. Wu, *Journal of Power Sources*, 2013, **240**, 644-652.
157. D. Wang, I. Belharouak, G. Zhou and K. Amine, *Advanced Functional Materials*, 2013, **23**, 1070-1075.
158. K. M. Hercule, Q. Wei, A. M. Khan, Y. Zhao, X. Tian and L. Mai, *Nano letters*, 2013, **13**, 5685-5691.
159. J. Jiang and J. R. Dahn, *Electrochimica Acta*, 2005, **50**, 4778-4783.
160. H. Deng, I. Belharouak, C. S. Yoon, Y. K. Sun and K. Amine, *Journal of The Electrochemical Society*, 2010, **157**, A1035.
161. H. Yu and H. Zhou, *The Journal of Physical Chemistry Letters*, 2013, **4**, 1268-1280.
162. *United States Pat.,* 4.959,281, 1990.
163. A. Manthiram, K. Chemelewski and E.-S. Lee, *Energy & Environmental Science*, 2014, **7**, 1339-1350.
164. C. H. Lei, J. Bareño, J. G. Wen, I. Petrov, S. H. Kang and D. P. Abraham, *Journal of Power Sources*, 2008, **178**, 422-433.
165. J.-S. Kim, C. S. Johnson, J. T. Vaughey and M. M. Thackeray, *Chemistry of Materials*, 2004, **16**, 1996-2006.
166. C. Pan, Y. J. Lee, B. Ammundsen and C. P. Grey, *Chemistry of Materials*, 2002, **14**, 2289-2299.
167. Y. Miura, Y. Yasui, M. Sato, N. Igawa and K. Kakurai, *Journal of the Physical Society of Japan*, 2007, **76**, 033705.
168. D. Mori, H. Sakaebe, M. Shikano, H. Kojitani, K. Tatsumi and Y. Inaguma, *Journal of Power Sources*, 2011, **196**, 6934-6938.

169. S. Laha, E. Morán, R. Sáez-Puche, M. Á. Alario-Franco, A. J. Dos santos-Garcia, E. Gonzalo, A. Kuhn, S. Natarajan, J. Gopalakrishnan and F. García-Alvarado, *Journal of Materials Chemistry A*, 2013, **1**, 10686-10692.
170. A. C. W. P. G. James, J. B., *Journal of Solid State Chemistry*, 1988, **74**, 287-294.
171. H. Kobayashi, R. Kanno, Y. Kawamoto, M. Tabuchi, O. Nakamura and M. Takano, *Solid State Ionics*, 1995, **82**, 25-31.
172. V. Massarotti, D. Capsoni, M. Bini, G. Chiodelli, C. B. Azzoni, M. C. Mozzati and A. Paleari, *Journal of Solid State Chemistry*, 1997, **131**, 94-100.
173. M. Johannes, A. Stux and K. Swider-Lyons, *Physical Review B*, 2008, **77**, 075124-075124-075128.
174. G. Jackeli and D. Khomskii, *Physical Review Letters*, 2008, **100**, 147203-147201-147203-147204.
175. M. J. O'Malley, H. Verweij and P. M. Woodward, *Journal of Solid State Chemistry*, 2008, **181**, 1803-1809.
176. A. Manthiram, *The Journal of Physical Chemistry Letters*, 2011, **2**, 176-184.
177. A. Manthiram, Y. Fu, S. H. Chung, C. Zu and Y. S. Su, *Chem Rev*, 2014, **114**, 11751-11787.
178. A. Manthiram and L. Li, *Advanced Energy Materials*, 2015, **5**, n/a-n/a.
179. N. Yabuuchi, K. Kubota, M. Dahbi and S. Komaba, *Chem Rev*, 2014, **114**, 11636-11682.
180. I. Shterenberg, M. Salama, Y. Gofer, E. Levi and D. Aurbach, *MRS Bulletin*, 2014, **39**, 453-460.
181. A. Manthiram, J. C. Knight, S.-T. Myung, S.-M. Oh and Y.-K. Sun, *Advanced Energy Materials* (in press).
182. H. Arai, S. Okada, Y. Sakurai and J.-i. Yamaki, *Journal of the Electrochemical Society*, 1997, **144**, 3117-3125.
183. H. Arai, S. Okada, H. Ohtsuka, M. Ichimura and J. Yamaki, *Solid State Ionics*, 1995, **80**, 261-269.
184. H. Arai, S. Okada, Y. Sakurai and J.-i. Yamaki, *Solid State Ionics*, 1997, **95**, 275-282.
185. M. Armand and J. M. Tarascon, *Nature*, 2008, **451**, 652-657.
186. D. H. Jang, Y. J. Shin and S. M. Oh, *Journal of the Electrochemical Society*, 1996, **143**, 2204-2211.
187. R. J. Gummow, A. de Kock and M. M. Thackeray, *Solid State Ionics*, 1994, **69**, 59-67.
188. W. Choi and A. Manthiram, *Journal of The Electrochemical Society*, 2006, **153**, A1760.
189. X. Wang, H. Nakamura and M. Yoshio, *Journal of Power Sources*, 2002, **110**, 19-26.
190. A. Blyr, C. Sigala, G. Amatucci, D. Guyomard, Y. Chabre and J. M. Tarascon, *Journal of the Electrochemical Society*, 1998, **145**, 194-209.
191. J. Morales, R. Stoyanova, J. L. Tirado and E. Zhecheva, *Journal of Solid State Chemistry*, 1994, **113**, 182-192.

192. E. Zhecheva and R. Stoyanova, *Journal of Solid State Chemistry*, 1994, **109**, 47-52.
193. R. Stoyanova, E. Zhecheva and L. Zarkova, *Solid State Ionics*, 1994, **73**, 233-240.
194. R. Gupta and A. Manthiram, *Journal of Solid State Chemistry*, 1996, **121**, 483-491.
195. S. Venkatraman and A. Manthiram, *Journal of Solid State Chemistry*, 2004, **177**, 4244-4250.
196. J. Choi, E. Alvarez, T. A. Arunkumar and A. Manthiram, *Electrochemical and Solid-State Letters*, 2006, **9**, A241-A244.
197. A. Manthiram and W. Choi, *Electrochemical and Solid-State Letters*, 2007, **10**, A228.
198. R. V. Chebiam, A. M. Kannan, F. Prado and A. Manthiram, *Electrochemistry Communications*, 2001, **3**, 624-627.
199. B. Ammundsen, P. B. Aitchison, G. R. Burns, D. J. Jones and J. Roziere, *Solid State Ionics*, 1997, **97**, 269-276.
200. B. Ammundsen, D. J. Jones and J. Roziere, *Chemistry of Materials*, 1995, **7**, 2151-2160.
201. Q. Feng, Y. Miyai, H. Kanoh and K. Ooi, *Langmuir : the ACS journal of surfaces and colloids*, 1992, **8**, 1861-1867.
202. K. R. Chemelewski, W. Li, A. Gutierrez and A. Manthiram, *Journal of Materials Chemistry A*, 2013, **1**, 15334.
203. Y. Kadoma, S. Sato, K. Ui and N. Kumagai, *Electrochemistry*, 2010, **78**, 658-661.
204. R. K. Katiyar, R. Singhal, K. Asmar, R. Valentin and R. S. Katiyar, *Journal of Power Sources*, 2009, **194**, 526-530.
205. M. Aklalouch, R. M. Rojas, J. M. Rojo, I. Saadoune and J. M. Amarilla, *Electrochimica Acta*, 2009, **54**, 7542-7550.
206. H. Bang, V. S. Donepudi and J. Prakash, *Electrochimica Acta*, 2002, **48**, 443-451.
207. A. Manthiram, J. S. Swinnea, Z. T. Sui, H. Steinfink and J. B. Goodenough, *Journal of the American Chemical Society*, 1987, **109**, 6667-6669.
208. T. Ohzuku, K. Ariyoshi, S. Takeda and Y. Sakai, *Electrochimica Acta*, 2001, **46**, 2327-2336.
209. M. Gracia, J. F. Marco, J. R. Gancedo, J. Ortiz, R. Pastene and J. L. Gautier, *Journal of Physical Chemistry C*, 2010, **114**, 12792-12799.
210. J. M. Amarilla, J. L. Martin de Vidales and R. M. Rojas, *Solid State Ionics*, 2000, **127**, 73-81.
211. A. Bhaskar, D. Mikhailova, N. Kiziltas-Yavuz, K. Nikolowski, S. Oswald, N. N. Bramnik and H. Ehrenberg, *Progress in Solid State Chemistry*, 2014, DOI: 10.1016/j.progsolidstchem.2014.04.007.
212. L. Hernan, J. Morales, L. Sanchez and J. Santos, *Solid State Ionics*, 1999, **118**, 179-185.
213. A. A. Andriiko, A. Y. Shpak, N. Y. Vlasenko and N. M. Stepanenko, *Chemistry of Metals and Alloys*, 2008, **1**, 283-287.

214. B. J. Hwang, Y. W. Tsai, D. Carlier and G. Ceder, *Chemistry of Materials*, 2003, **15**, 3676-3682.
215. H. Kobayashi, H. Sakaebe, H. Kageyama, K. Tatsumi, Y. Arachi and T. Kamiyama, *Journal of Materials Chemistry*, 2003, **13**, 590-595.
216. H. D. Yoo, I. Shterenberg, Y. Gofer, G. Gershinsky, N. Pour and D. Aurbach, *Energy & Environmental Science*, 2013, **6**, 2265.
217. M. C. Lin, M. Gong, B. Lu, Y. Wu, D. Y. Wang, M. Guan, M. Angell, C. Chen, J. Yang, B. J. Hwang and H. Dai, *Nature*, 2015, **520**, 325-328.
218. C. Xu, S. W. Chiang, J. Ma and F. Kang, *Journal of the Electrochemical Society*, 2012, **160**, A93-A97.
219. C. Xu, B. Li, H. Du and F. Kang, *Angewandte Chemie*, 2012, **51**, 933-935.
220. B. Lee, H. R. Lee, H. Kim, K. Y. Chung, B. W. Cho and S. H. Oh, *Chemical communications*, 2015, **51**, 9265-9268.
221. B. Lee, C. S. Yoon, H. R. Lee, K. Y. Chung, B. W. Cho and S. H. Oh, *Scientific reports*, 2014, **4**, 6066.
222. J. Lee, J. B. Ju, W. I. Cho, B. W. Cho and S. H. Oh, *Electrochimica Acta*, 2013, **112**, 138-143.
223. G. G. Amatucci, F. Badway, A. Singhal, B. Beaudoin, G. Skandan, T. Bowmer, I. Plitz, N. Pereira, T. Chapman and R. Jaworski, *Journal of The Electrochemical Society*, 2001, **148**, A940.
224. R. Chevrel, M. Sergent and J. Prigent, *Journal of Solid State Chemistry*, 1971, **3**, 515-519.
225. D. Aurbach, I. Weissman, Y. Gofer and E. Levi, *Chemical record*, 2003, **3**, 61-73.
226. R. Mohtadi, M. Matsui, T. S. Arthur and S. J. Hwang, *Angewandte Chemie*, 2012, **51**, 9780-9783.
227. Y. Shao, T. Liu, G. Li, M. Gu, Z. Nie, M. Engelhard, J. Xiao, D. Lv, C. Wang, J. G. Zhang and J. Liu, *Scientific reports*, 2013, **3**, 3130.
228. J. Zhu, Y. Guo, J. Yang, Y. Nuli, F. Zhang, J. Wang and S.-i. Hirano, *Journal of Power Sources*, 2014, **248**, 690-694.
229. P. Novak and J. Desilverstro, *Journal of The Electrochemical Society*, 1993, **140**, 140-144.
230. M. E. Spahr, P. Novak, O. Haas and R. Nesper, *Journal of Power Sources*, 1995, **54**, 346-351.
231. Z. Feng, J. Yang, Y. NuLi and J. Wang, *Journal of Power Sources*, 2008, **184**, 604-609.
232. Y. Zheng, Y. NuLi, Q. Chen, Y. Wang, J. Yang and J. Wang, *Electrochimica Acta*, 2012, **66**, 75-81.
233. J. Giraudet, D. Claves, K. Guérin, M. Dubois, A. Houdayer, F. Masin and A. Hamwi, *Journal of Power Sources*, 2007, **173**, 592-598.
234. J. Vatsala Rani, S. Bhavana Rushi, V. Kanakaiah and S. Palaniappan, *Journal of The Electrochemical Society*, 2011, **158**, A1031.
235. P. Novak, W. Sheifele, F. Joho and O. Haas, *Journal of The Electrochemical Society*, 1995, **142**, 2544-2550.

236. P. Novak, W. Sheifele and O. Haas, *Journal of Power Sources*, 1995, **54**, 479-482.
237. L. Sanchez and J.-P. Pereira-Ramos, *Journal of Materials Chemistry*, 1997, **7**, 471-473.
238. K. Makino, Y. Katayama, T. Miura and T. Kishi, *Journal of Power Sources*, 2001, **99**, 66-69.
239. K. Makino, Y. Katayama, T. Miura and T. Kishi, *Journal of Power Sources*, 2002, **112**, 85-89.
240. T. D. Gregory, R. J. Hoffman and R. C. Winterton, *Journal of The Electrochemical Society*, 1990, **137**, 775-780.
241. C. Ling and F. Mizuno, *Chemistry of Materials*, 2013, **25**, 3062-3071.
242. C. Yuan, Y. Zhang, Y. Pan, X. Liu, G. Wang and D. Cao, *Electrochimica Acta*, 2014, **116**, 404-412.
243. N. N. Sinha and N. Munichandraiah, *Electrochemical and Solid-State Letters*, 2008, **11**, F23.
244. C. Kim, P. J. Phillips, B. Key, T. Yi, D. Nordlund, Y. S. Yu, R. D. Bayliss, S. D. Han, M. He, Z. Zhang, A. K. Burrell, R. F. Klie and J. Cabana, *Advanced materials*, 2015, DOI: 10.1002/adma.201500083.
245. J. C. Knight, S. Therese and A. Manthiram, *Journal of The Electrochemical Society*, 2015, **162**, A426-A431.
246. R. Manaila, *Journal of Physics and Chemistry of Solids*, 1967, **28**, 2335-2341.
247. F. C. Romeijn, *Philips Research Reports*, 1953, **8**, 304-320.
248. A. P. B. Sinha, N. R. Sanjana and A. B. Biswas, *Acta Crystallographica*, 1957, **10**, 439-440.
249. K. S. Irani, A. P. B. Sinha and A. B. Biswas, *Journal of Physics and Chemistry of Solids*, 1962, **23**, 711-727.
250. S. T. Kshirsagar and A. B. Biswas, *Journal of Physics and Chemistry of Solids*, 1967, **28**, 1493-1499.
251. M. Rosenberg and P. Nicolau, *Physica Status Solidi*, 1964, **6**, 101-110.
252. R. Manaila and P. Pausescu, *Physica Status Solidi*, 1965, **9**, 385-394.
253. N. K. Radhakrishnan and A. B. Biswas, *Physica Status Solidi A*, 1976, **37**, 719-722.
254. V. P. Barkhatov, V. F. Balakibev, Y. V. Golikov and E. G. Kostitsin, *Physica Status Solidi A*, 1983, **76**, 57-63.
255. C. B. Azzoni, M. C. Mozzati, L. Malavasi, P. Ghigna and G. Flor, *Solid State Communications*, 2001, **119**, 591-595.
256. L. Malavasi, P. Ghigna, G. Chiodelli, G. Maggi and G. Flor, *Journal of Solid State Chemistry*, 2002, **166**, 171-176.
257. L. Malavasi, C. Tealdi, G. Flor and M. Amboage, *Physical Review B*, 2005, **71**.
258. S. K. Panda, I.-H. Jung and T. Bessmann, *Journal of the American Ceramic Society*, 2014, **97**, 3328-3340.
259. Qi Feng, Yoshitaka Miyai, Hirofumi Kanoh and K. Ooi, *Chemistry of Materials*, 1993, **5**, 311-316.

260. R. V. Chebiam, F. Prado and A. Manthiram, *Journal of Solid State Chemistry*, 2002, **163**, 5-9.
261. J. Choi, E. Alvarez, T. A. Arunkumar and A. Manthiram, *Electrochemical and Solid-State Letters*, 2006, **9**, A241.
262. E.-S. Lee and A. Manthiram, *Journal of Materials Chemistry A*, 2014, **2**, 3932.
263. M. Peiteado, A. Kodre, I. Arcon, A. C. Caballero and D. Makovec, *Journal of the American Ceramic Society*, 2010, **93**, 590-595.
264. C. Kim, P. J. Phillips, B. Key, T. Yi, D. Nordlund, Y. S. Yu, R. D. Bayliss, S. D. Han, M. He, Z. Zhang, A. K. Burrell, R. F. Klie and J. Cabana, *Advanced materials*, 2015, **27**, 3377-3384.

Vita

James Knight was born in Hilliard, Ohio. He attended the Ohio State University and graduated in 2009 with a B.S. in chemical engineering. He then attended the University of Texas at Austin and received a Ph.D. in chemical engineering in 2015, where he worked on cathode materials for Li-ion and other rechargeable batteries.

Email Address: jknight.205@gmail.com

This dissertation was typed by the author.